POLITECNICO
MILANO 1863

SCUOLA DI INGEGNERIA INDUSTRIALE
E DELL'INFORMAZIONE

EXECUTIVE SUMMARY OF THE THESIS

Spatio-temporal Analysis and Monitoring of Temperature in Extrusion-based AM processes

TESI MAGISTRALE IN MANAGEMENT ENGINEERING – INGEGNERIA GESTIONALE

AUTHOR: EMANUELE CARRARO

ADVISOR: BIANCA MARIA COLOSIMO

CO-ADVISOR: FABIO CALTANISSETTA

ACADEMIC YEAR: 2020-2021

1. Introduction

In the past years, Additive Manufacturing (AM) technologies have drastically changed the manufacturing panorama, introducing a vast range of new possibilities in terms of product design, materials, and applications. Extrusion-based AM processes recently found themselves under the spotlight due to the extension of printable material range (techno-polymers, ceramics, metals etc.) and to the capability of producing large parts (>1 m^3). However, low repeatability and stability have limited the diffusion of extrusion-based AM in industrial world, being unable to achieve quality desired for finished products.

To tackle this issue, the scientific and the industrial community have recently proposed methods based on in-situ monitoring to prevent the arising of defects, in a first-time-right production perspective. Among many available information sources, the process thermal behaviour has recently found significant interest, since it allows the identification of anomalies linked to quality issues, such as lack of bond (i.e., delamination, inter-road voids), failures due to heat retention, warpage, and over/under-extrusion states. So far, most of studies on thermal profiles analysis are based on data acquired via IR thermography. However, many papers are dedicated to in-situ sensing solutions for temperature measurement, without taking steps towards automatic defect identification. Moreover, none of the existing studies tackled together the temperature temporal evolution and the spatial dimension (i.e., the location within the layer where temperature profiles are extracted). In this thesis, a methodology for spatiotemporal thermal data analysis and monitoring of AM processes is proposed. The methodology is inspired by the paper from Gao et al. (2019) [1], in which the authors presented a new version of Local Moran's I [2], that embeds a temporal descriptor (Z index). This index and a methodology for monitoring and diagnosis were tested both on simulation experiments and on a real case study.

2. Methodology

In this section, we will describe the methodology inspired by Gao et al. (2019) for the analysis of spatiotemporal data. More in details, we will describe the proposed indicator computation. This index will be applied to simulation and a real case study for data analysis and monitoring.
First of all, given the set of time series from a time interval [1, T], each associated to a specific location (thus to spatial information), the average profile is computed as the empirical average of all points. With this profile, for each location *i*, the indicator ${Z_i}^T$ from Gao et al. (2019) is computed (hereafter referred to as *Z index*). This indicator expresses the deviation of profile X_i with respect to the average one (X_{avg}). Its formula is the following:

$$ {Z_i}^T = \varphi\big(CORT(X_i, X_{avg})\big) \cdot (V_i - V_{avg}) \quad (1) $$

The indicator is the result of multiplication of two components.
The former, called *CORT component*, expresses deviation from average profile in terms of shape. It is computed as the φ transformation of the CORT function, where:

$$ CORT(X_T, Y_T) = \frac{\sum_t^{T-1}(X_{t+1} - X_t)(Y_{t+1} - Y_t)}{\sqrt{\sum_t^{T-1}(X_{t+1} - X_t)^2}\ \sqrt{\sum_t^{T-1}(Y_{t+1} - Y_t)^2}} \quad (2) $$

This function, given two time series X_T and Y_T, computes the correlation coefficient between the vectors containing their successive differences. As a consequence, the indicator assumes values in the interval [-1,1]. φ is an exponential adaptive tuning function. Its formula is the following:

$$ \varphi(x) = \frac{2}{1 + e^{2x}} \quad (3) $$

This transformation remaps the CORT in a range between 0 and 2, in a way that the strongest the correlation with average profile, the lower is CORT component.
The second component, called *Area Difference component*, consists of the difference between the accumulative volumes under the two curves. This corresponds to the difference between the areas under the curve of both, thus:

$$ V_i = \int_1^T X_i \, dt \quad (4) $$

Temporal profiles above the average one will assume positive values for the component, while profiles below the average one will assume negative values.

Following the steps from Gao et al. (2019), the indicator ${Z_i}^T$ is used as substitute for the term z_i of *Local Moran's I*, which for element *i*, has equation:

$$ I_i = z_i \cdot \sum_j w_{ij} z_j \quad (5) $$

Where w_{ij} is a weight expressing spatial proximity between element *i* and element *j*; generally, the inverse of Euclidian distance is used. Local Moran's I expresses spatial correlation between element *i* and its neighbours. If *i* it is surrounded by elements with similar value, then $I_i > 0$. On the other hand, if surrounded by dissimilar values, $I_i < 0$. If it is surrounded by both similar and dissimilar in a random arrangement, then $I_i \approx 0$.
Analytically, Local Moran's I will assume higher values when ${Z_i}^T$ and the weighted sum of other elements are higher (in absolute values). Therefore, the indicator gives more relevance to association of profiles that deviate more from the average.
The result of the first step is then availability of two metrics associated to each location of the dataset, Z index and Local Moran's I.

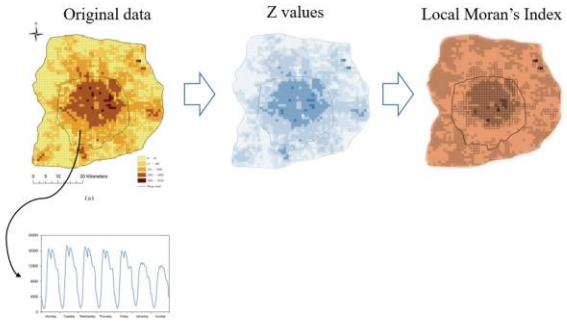

Figure 1: Workflow of indicators extraction: starting from the time series, Z indexes are extracted; then these become the input for computation of Local Moran's I

In the context of Extrusion-based AM, the methodology is transposed to a set of temperature profiles, extracted from predefined locations of each layer. Therefore, we are able to describe thermal evolution of each layer through the Z indexes and Local Moran's I of each location. The way in which the two metrics can be used to detect anomalous layers and identify the locations that correspond to anomalous thermal behaviour are explained through the simulation example provided in the following section.

3. Simulation

The methodology is tested in a simulation environment to assess its performance in automatic defect identification. The availability of thermographic data of layers from extrusion-based AM processes is simulated by generating 9x9 matrices, where each cell contains a temperature profile generated with the following equation:

$$\ln T(t) = \beta_0 + \beta_1 t + \beta_2 t^2 + \varepsilon_t \qquad (6)$$

Where:
$\ln T(t)$: natural logarithm of temperature T as function of time
$\beta_0, \beta_1, \beta_2$: coefficients of the second order polynomial function
ε_t: residual between polynomial function and observed temperature logarithm at time instant t
The values of $\beta_0, \beta_1, \beta_2$ and ε_t are generated following the normal distributions indicated in a precedent study [3].
Three defective scenarios are simulated by altering the β_1 coefficient of certain locations (alterations consist of addition of K standard deviations). For each scenario, multiple experiments are performed, each with different number of defective cells and different intensity of alteration. The first scenario is *single cluster*, and defective cells are located in a unique spatial cluster. The second is *sparse defects*, and defective cells are scattered randomly throughout the matrix. The third scenario is *two clusters*, and two groups of clustered defects are generated, each with same intensity of alteration, but opposite sign. Examples of the three scenarios are shown in the following figure.

Figure 2: Examples of the three defective scenarios: single cluster (left), sparse defects (centre), two clusters (right)

To provide a practical example of how the simulation works, the *single cluster* experiment with defective region of 3x3 cells and $K = 3$ is analysed. Hereafter, a visualization of the temperature profiles simulated is provided.

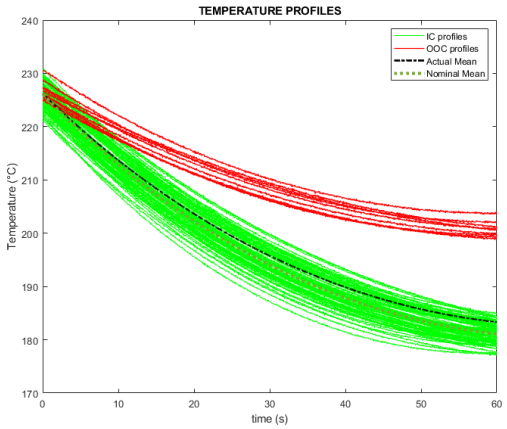

Figure 3: Temperature profiles from simulation example

After the computation of the empirical average profile (in the graph represented with the black dotted line), *Z index* is computed for each cell. As can be seen in Figure 4.
The indicator assumes higher value for the defective cells, as result of combination of higher Area Difference (since the altered profiles are above the average one) and high CORT component, due to lower correlation with average profile.
Z index is then used to compute Local Moran's I, following equation (5). From the visualization of Figure 4, we can see that the indicator detects positive correlation in the cells belonging to the cluster, which is the desirable result knowing that cells with high and same-sign Z indexes are located close together.

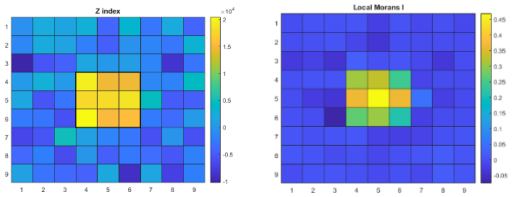

Figure 4: Z index (left) and Local Moran's I (right) visualization through heatmap; the defective region is highlighted through thick border

In order to test the possibility of using these statistics in a process control framework the *mean Z index* and *Global Moran's I* are computed respectively as mean of all Z indexes and of all Local Moran's I of a layer.
More in details, we generate 100 matrices without OOC cells. These matrices (and the associated mean Z index and Global Moran's I) were used to build a Shewhart control chart. Then, 5 additional matrices are generated, this time with defect

introduction. Figure 5 shows resulting control charts when, for each defective matrix, the same layout of the experiment above is used (thus 9 clustered cells with same intensity $K = 3$).

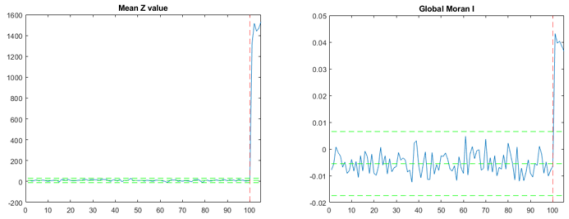

Figure 5: Control Charts for mean Z index and Global Moran's I

In concurrence with the beginning of defective layers, both metrics show very relevant jumps, with values far from the control limits. The presence of an alarm in both CC hints at both presence of outliers in terms of thermal behaviour, and presence of positive spatial association, which means that the outliers are most likely clustered together. Both observations are in line with the experiment simulated.

The monitoring approach described above is then tested for all experiments of all three scenarios, changing defect size and intensity. The control charts built on Global Moran's I and mean Z index are very effective in detection of anomalies, being able to trigger an alarm in at least one of the two charts in all experiments. In particular, for *single cluster* we have alarms on both charts, for *sparse defects* only on mean Z index chart, for *two clusters* only on Global Moran's I chart.

As for diagnostics, which consists of the automatic identification of the cells with abnormal thermal behaviour, a classification of elements according to Z index is proposed, knowing that independently from the degree of spatial association, the indicator is capable of capturing well abnormal thermal behaviour. In specific, agglomerative hierarchical clustering is applied on the Z index, in order to subdivide all elements into groups of similar thermal behaviour, according to this metric [4].

The diagnostic approach based on hierarchical clustering is compared with an approach based on significance level of Local Moran's I, described in Gao et al. (2019). The former method sees improved performances in the identification of defective cells in all three scenarios, when compared to the other. In particular, great improvements are obtained in the two weak cases of the latter method: *single cluster* scenario, when number of OOC cells is high, and all *sparse defects* experiments. In particular, in both cases the approach from Gao et al. (2019) presents many false negatives.

Recall	K=2	K=3	K=4
Single Cluster	**[0.814, 0.98]** *[0.241, 0.964]*	**[0.983, 1]** *[0.287, 0.999]*	**[0.998, 1]** *[0.305, 1]*
Sparse Defects	**[0.836, 0.99]** *[0.02, 0.08]*	**[0.971, 1]** *[0.022, 0.04]*	**[0.998, 1]** *[0.018, 0.12]*
Two Clusters	**[0.778, 0.945]** *[0.13, 0.954]*	**[0.962 0.995]** *[0.23 0.982]*	**[0.992 1]** *[0.27 0.983]*

Table 1: Ranges of Recall for diagnostics based on Hierarchical clustering (**bold** text) and based on Local Moran's I significance (*italic* text) in the three scenarios for different alteration magnitude K

4. Real-data application

The dataset exploited for the real case study consists of the thermographic monitoring of a Big Area Additive Manufacturing (BAAM) build, manufactured by the large-scale printer developed at the Oak Ridge National laboratories in collaboration with Cincinnati Incorporated. Acrylonitrile Butadiene Styrene (ABS) with 20% of chopped carbon fibres weight is used to print a connected serpentine pattern; this toolpath is repeated for 15 layers.

Extruder temperature was set at 230°C, while the building platform was pre-heated at 90°C. Extruder speed was 63.5 mm/s, so that a single layer printing lasts around 70 seconds. IR images of the process are acquired at a framerate of 30 fps using a FLIR A35 thermal camera (FLIR® Systems Inc, Wilsonville, U.S.), positioned near the build area (approximately 1.3 m from the target object) with an inclination with respect to the building platform of around 45°.

For each layer, temperature profiles are extracted from 506 Regions of Interest (ROI), which can be visualized as the grid placed over the serpentine shown in Figure 6.

Each profile is made of a set of temperature acquisition, where each value corresponds to a frame of the IR video. All profiles are subjected to pre-processing, in order to synchronize them and to filter out noisy regions linked to the passing of the extruder between the ROI and the camera.

Once the set of temperature profiles of each layer is available, Z index and Local Moran's I are computed.

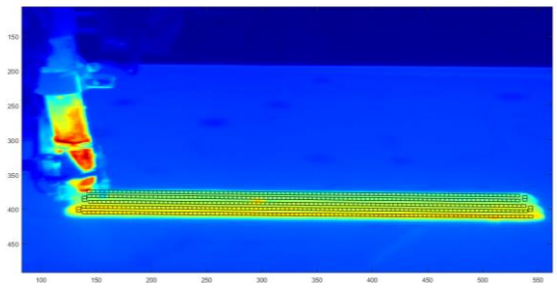

Figure 6: Visualization of grid over serpentine

A first assessment on the thermal dynamics throughout the process can be made by looking at visual representations of the two indicators. In specific, for both of them we provide a visualization of the spatial arrangement of the 506 ROIs, each coloured according to the average value of the indicator across the 15 layers and a visualization of the evolution of the indicator along the succession of the 506 ROIs for each of the 15 layers.

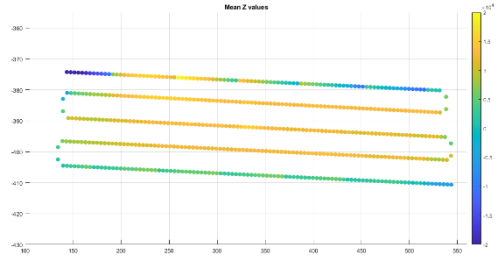

Figure 7: Scatterplot of all ROIs with colormap used to visualize average Z index across 15 layers

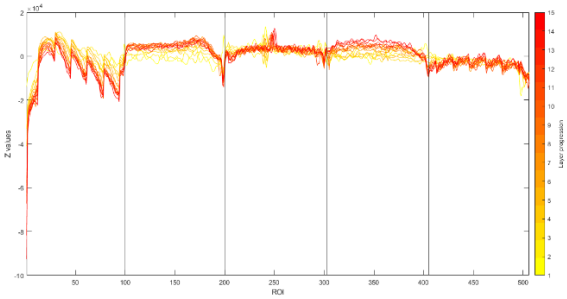

Figure 8: Z index by ROI for each of the 15 layers; vertical lines are used to mark turning points between beads, while colormap is used to visualize layer progression; since ROI sequence follows extruder path, these profiles show temporal evolution for Z index for a layer along its printing

Z indexes show that despite the simplicity of the toolpath, the thermal behaviour of the print is very complex, highlighting presence of relevant patterns. In specific, we see for all layers after the first one presence of a very cold region at the beginning of bead 1, most likely linked to under-extrusion at beginning of the layer. Then, beads 1 and 5 show jumping patterns, which are much more intense in the former, probably linked to discontinuities in the material feed rate. The inner beads show higher Z indexes, symptom of either slower cooling rate of higher initial temperature. As layers progress, the indexes become even higher due to stronger heat retention than other locations of the layer. Finally, most layers present a hot spot in the middle of bead 3, which is always induced by the reheating concurrent to passing of the extruder above that location while moving from last to first ROI, to begin the new layer.
As for the analysis of Local Moran's I, the indicator confirms some of the patterns of Z index and shows some more insights.

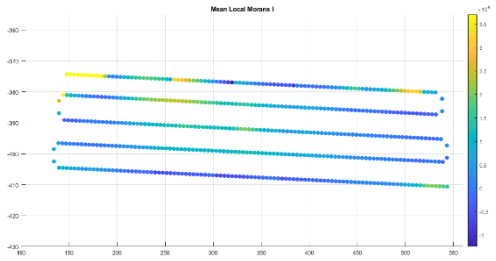

Figure 9: Average Local Moran's I of each ROI

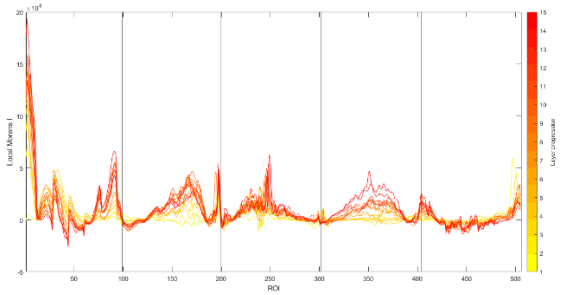

Figure 10: Local Moran's I by ROI for each of the 15 layers

The strongest positive association region is linked to the cold beginning of bead 1, which is much more intense than any other spatial correlation pattern. We do see, as layers progress, increasing association in the central beads, due to their increasing Z index values. The indicator also highlights the hot spot with a spike, and is very irregular during the jumps of beads 1 and 5.

As done in simulation, the two global metrics – mean Z index and Global Moran's I – can be

computed for each layer. The two cannot be used for monitoring purposes, since there is no information about what is in-control to build control limits. Nevertheless, they can be used to give an assessment of the overall trend of the print.

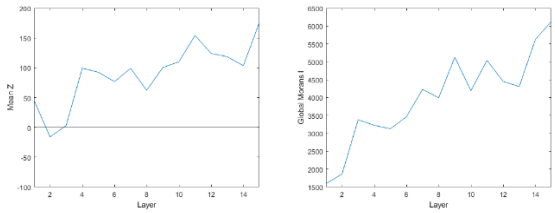

Figure 11: Mean Z index by layer (left), Global Moran's I by layer (right)

Both metrics show a growing trend along layer progression, hinting at the non-stationarity of the process. In specific, mean Z index highlights that there is increasing unbalance of Z index distribution towards positive high values. This tendency can be linked to the heat retention pattern of the inner beads. Global Moran's I shows increasing positive association, which means that there is an increasing number of regions with similar thermal behaviour, associated to high values of Z index (in absolute value).

Finally, another approach for automatic flaws detection is proposed on real data. Looking at Z index, we see presence of localized inhomogeneities, i.e., consecutive ROIs with very different thermal behaviour. Therefore, an approach to identify inhomogeneities in thermal behaviour by means of this indicator is proposed. Z index by ROI is a signal characterized by positive autocorrelation even after differentiation. Therefore, the EWMA statistic is used as one-step-ahead predictor of differentiated Z index, to then build a Control Chart on residuals. This approach is an effective way to deal with positively autocorrelated data. The method is built to work excluding all ROIs on the border (thus beads 1-5 and turning points), seeing how they are far less stable than inner ones and knowing that defects on border may be dealt with via post-processing. A Control Chart on residuals of an EWMA model is trained on layer 1 and used to detect abnormal shifts in Z index between adjacent cells for all other layers. The methodology is able to identify the central hot spot present in many layers, together with inhomogeneities at the beginning or end of central beads, probably linked to instabilities in material feed rate.

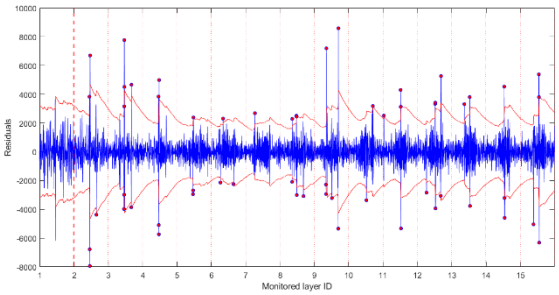

Figure 12: CC on EWMA residuals

5. Conclusions

The methodology developed in this thesis provides a powerful tool to gain a deep understanding of the thermal behaviour in extrusion-based AM processes. Through simulation studies, we assessed its ability to automatically detect flaws in different scenarios. As for the real case study, while the dataset was not suitable to apply the methodology for monitoring purposes as it was developed, many insights about thermal evolution were identified through qualitative assessment, and a different monitoring approach, based on the same indicators was successfully employed.
Future developments encompass the expansion of simulation to different scenarios, the combination between the current methodology and the a priori knowledge on the average (or target) thermal profile and the application to new case studies with different AM technologies.

Bibliography

[1] Y. Gao, J. Cheng, H. Meng and Y. Liu, "Measuring spatio-temporal autocorrelation in time series data of collective human mobility," *Geo-Spatial Information Science,* vol. 22, no. 3, pp. 166-173, 2019.

[2] L. Anselin, "Local Indicators of Spatial Association-LISA," 1995.

[3] F. Caltanissetta, G. Dreyfus, A. J. Hart and B. M. Colosimo, "In-situ monitoring of Extrusion-based processes via thermal videoimaging with application to Big Area Additive Manufacturing (BAAM)," *Additive Manufacturing,* 2021.

[4] C. Vercellis, Business Intelligence, 2009.

POLITECNICO
MILANO 1863

SCUOLA DI INGEGNERIA INDUSTRIALE
E DELL'INFORMAZIONE

Spatio-temporal Analysis and Monitoring of Temperature in Extrusion-based AM processes

TESI DI LAUREA MAGISTRALE IN
MANAGEMENT ENGINEERING

Author: **Emanuele Carraro**

Student ID:	939737
Advisor:	Bianca Maria Colosimo
Co-advisor:	Fabio Caltanissetta
Academic Year:	2020-21

Alla Nonna Dina,

Perchè senza radici un albero

È solo un pezzo di legno

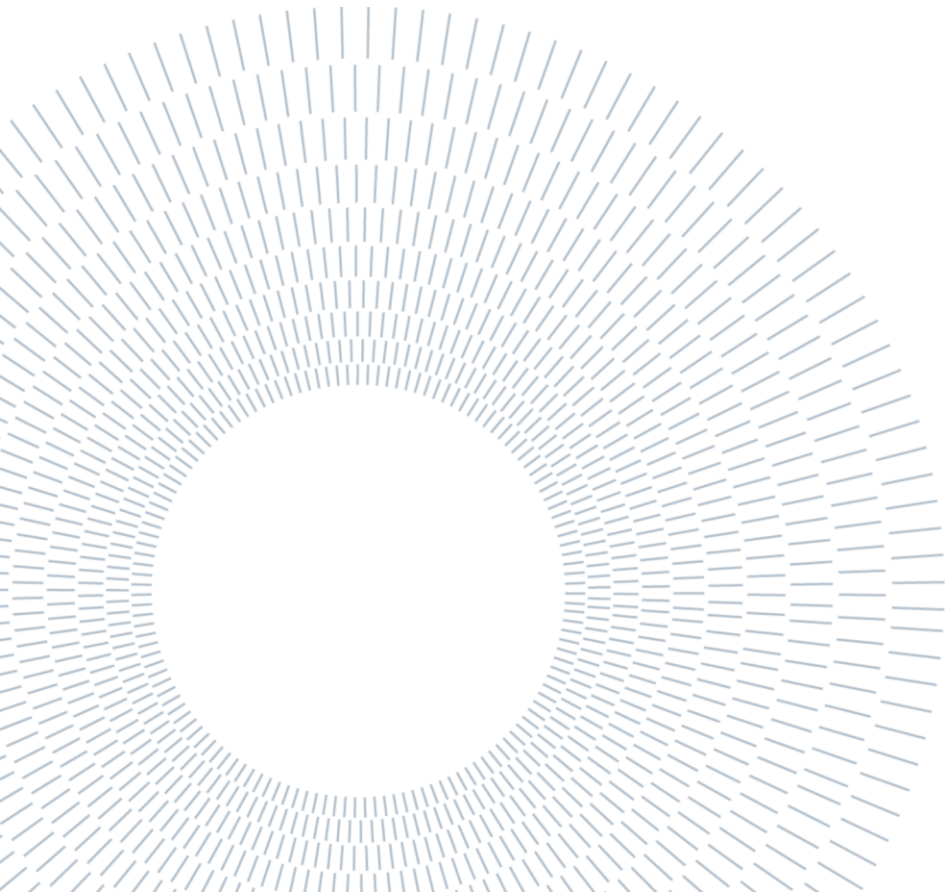

Abstract

Extrusion-based Additive Manufacturing technologies are widely adopted in the industrial world for rapid prototyping purposes and among hobbyists for domestic applications. In the last years, they have been facing disruptive technological innovation, due to trends like Bioprinting, Large Area Additive Manufacturing (LAAM) and new materials (composites and metals). However, the diffusion of these technologies in industrial world has been limited by their low stability and repeatability. For this reason, the latest research trends aim at developing suitable in-situ monitoring solutions, oriented towards zero-defect manufacturing. In particular, in-situ thermography is commonly used as mean to study the process and understand its dynamics from a thermal point of view. Despite the growing number of articles on the theme, there is lack of quantitative methods that put together spatial and temporal dimensions to analyse thermal phenomena. Besides, a very limited number of methodologies for automatic flaws detection based on thermography has been proposed. This thesis seeks to fill this gap in scientific literature by proposing a methodology for in-situ monitoring of extrusion-based AM based on spatiotemporal analysis of the thermal behaviour. The methodology is based on the computation of a spatiotemporal indicator to gain knowledge about thermal behaviour of a print. The approach is applied on both a simulation case study and a real case study, consisting of a BAAM print.

Key-words: Extrusion-based AM, thermography, in-situ monitoring, Moran's I, BAAM, composite printing

Abstract in lingua italiana

Le tecnologie Extrusion-based Additive Manufacturing sono comunemente adottate in ambito industriale per la prototipazione rapida e tra gli hobbisti per applicazioni domestiche. Negli ultimi anni, questi processi hanno affrontato una fase di forte innovazione tecnologica, grazie a trend come Bioprinting, Large Area Additive Manufacturing (LAAM) e l'introduzione di nuovi materiali (compositi e metalli). Nonostante ciò, la loro diffusione in ambito industriale è stata limitata dalla scarsa stabilità e ripetibilità. Per questi motivi, recentemente la ricerca scientifica si è direzionata verso lo sviluppo di soluzioni per il monitoraggio in-situ, orientate alla produzione senza difetti. In particolare, la termografia in-situ è comunemente usata come mezzo per studiare il processo e capire le sue dinamiche dal punto di vista termico. Nonostante il crescente numero di articoli sul tema, vi è una mancanza di metodi che mettano insieme le dimensioni spaziali e temporali per analizzare i fenomeni termici. Inoltre, il numero di metodologie proposte finora per l'identificazione automatica dei difetti basata su termografia è limitato. Lo scopo di questa tesi è quello di colmare questi vuoti nella letteratura scientifica, proponendo una metodologia per il monitoraggio in-situ dei processi extrusion-based AM, basata sull'analisi spaziotemporale del comportamento termico. Tale metodologia si basa sul calcolo di un indicatore spaziotemporale, che consenta di comprendere meglio il comportamento termico di una stampa. L'approccio viene applicato sia su un caso di studio basata su simulazione, che su un caso di studio reale, cioè una stampa via BAAM.

Parole chiave: Extrusion-based AM, termografia, monitoraggio in-situ, Moran's I, BAAM, stampa con compositi

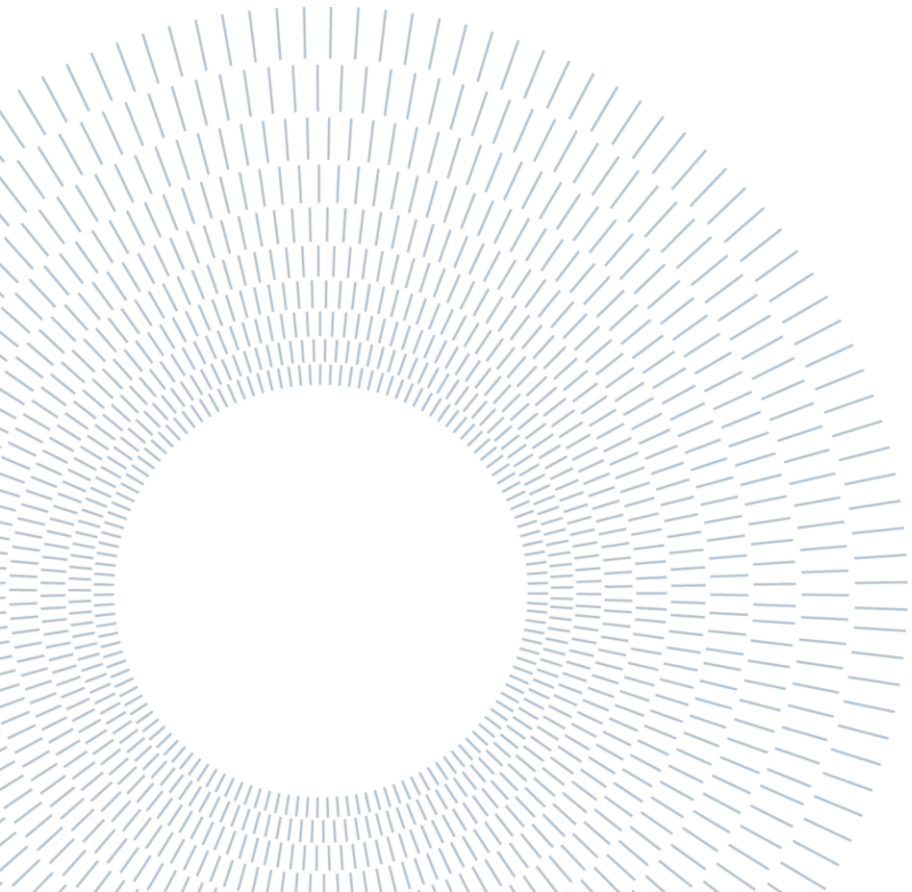

Contents

1. Introduction

Additive Manufacturing (AM) is defined as "the process of joining materials to make objects from three-dimensional (3D) model data, usually layer upon layer, as opposed to subtractive manufacturing methodologies" [1]. The definition encompasses a set of very different technologies that share the layerwise manufacturing rationale. In their manual *Additive Manufacturing Technologies*, Gibson et al. identify seven main categories to subdivide AM processes: Vat Photopolymerization, Powder Bed Fusion, Material Extrusion, Material Jetting, Binder Jetting, Sheet Lamination and Direct Energy Deposition [2]. These all have very different characteristics in terms of materials, quality, throughput, build dimension and production costs. What they share is the suitability for manufacturing of customized, monolithic, freeform and lightweight products.

Among the AM technologies, one that recently found itself under the spotlight is extrusion-based AM. For many years, extrusion-based techniques such as Fuse Deposition Modeling (FDM) - process trademarked by company Stratasys, commonly referred also as Fused Filament Fabrication (FFF) - have been exploited exclusively for production of cheap polymer prototypes. While the accessibility of the technology allowed to have a huge success among hobbyists for domestic applications, in industrial contexts it found few applications beyond rapid prototyping, due to low quality of the technology and poor mechanical performances of the thermoplastic polymers used as feedstock material. However, recent evolutions of extrusion-based processes are fostering the interest of academic and industrial worlds. Recent trends include the widening of range of materials, with successful use of *composite materials* and *metals*. One example of successful use of innovative materials for extrusion-based AM processes is *Desktop Metal*, an American technology company which has raised $438 million in venture funding (Google Ventures, BMW, Ford Motor Company) and that designs and sells 3D printing systems based on Bound Metal Deposition, a

proprietary technology similar in principle to FFF, but with cartridges of Highly Filled polymer with metal particles as feedstock. Other developments for extrusion-based AM include *bioprinting*, which is the application of AM in medicine and bioengineering fields. A noteworthy example is the *BIO X* bioprinter developed by *Cellink*, which can work with a wide range of bioinks [3]. The last development worthy of mention is Large Area Additive Manufacturing (LAAM), the set of AM technologies capable of processing big volume products. Successful applications of LAAM to extrusion-based processes have been developed in the USA, for example the BAAM system developed at the Oak Ridge National Laboratory in collaboration with *Cincinnati Inc*. [4], and in Europe, for example the *Masterprint* from *Camozzi group* [5].

Despite these interesting developments, the industrial expansion of extrusion-based AM is limited by the low repeatability and stability of the process. These are crucial factors for this technology breakthrough, considering the long processing time, the high cost and procurement time of material feedstock, the time consuming and expensive inspection and post-processing operations, and the high-quality standards coming from many of the industrial stakeholders. Recently, such issues have been tackled for other AM technologies, primarily on Powder Bed Fusion ones, with in-situ monitoring. It consists of the data collection and analysis during the printing process with the purpose of assessing whether the process is stable or whether parts defects or process flaws are arising [6]. In the past few years, the in-situ sensing and monitoring literature has grown exponentially also for material extrusion processes [7]. Authors tried to detect specific types of failures or defects through the exploitation of a big variety of signals, from images to acoustic emissions. Since extrusion-based AM processes rely on the material bonding through thermal process, the information coming from in-situ temperature monitoring has been identified as a suitable way to obtain knowledge on bond formation (identifying states of lack of bond or excessive heat retention), as well as to identify the arising of a wide variety of defects, such as porosity, material deposition errors (over/under-extrusion) and warpage. Nowadays, while many papers are dedicated to the development of thermal in-situ sensing setups or focus on a qualitative analysis of material's thermal evolution, very few works tackle automatic defect identification. Moreover, none of the aforementioned studies try to jointly consider the temporal evolution of temperature and the associated spatial information. Indeed, academic works that treat temperature sensing are limited to

either spatial or temporal analysis (for example by extracting temporal profiles in specific locations or spatial temperature distribution at specific instants).

This thesis aims at fulfilling these research gaps through the development of a methodology for the identification of inhomogeneities or undesired patterns in the temperature evolution of AM parts. In order to keep control over both spatial and temporal dimensions of analysis, the applicability and potentiality of a spatiotemporal model inspired by Gao et al. (2019) [8] are studied. This approach consists of the computation of an updated version of a local indicator for spatial association (Moran's I), with embedded indicators of deviation of temporal profiles from a benchmark [9]. The methodology is firstly applied in a simulation environment, developed with strong ties to real data. Then, it is applied to a real case study, exploiting an IR thermography dataset, developed in partnership with MIT, extracted from an experimental print from the BAAM system of Oak Ridge National Laboratory.

This thesis is organized as follows. In section 2 a state of the art on extrusion-based techniques, in-situ monitoring and indicators for spatiotemporal data analysis is provided. Section 3 is dedicated to the in-depth explanation of the methodology. In Section 4, simulation is used to assess the performance of the methodology in different scenarios. In the same chapter, some methodological improvements are discussed. Finally, in section 5, the methodology is applied on a real case study, providing explanation of how some challenges relative to data acquisition are faced and summing up the knowledge of the process obtained. In section 6 conclusions and possible future developments are discussed.

2. State-of-the art

2.1 Extrusion-based Additive Manufacturing

Extrusion-based AM refers to the set of AM processes in which material is selectively dispensed through a nozzle or orifice. The most diffused extrusion-based AM technique is Fuse Deposition Modeling (FDM), a trademarked technology owned by *Stratasys,* that is also commonly referred to as Fused Filament Fabrication (FFF). In a nutshell, FDM machines consist of a Computer Numerically Controlled gantry, equipped with a liquefying system and a nozzle. Upon application of pressure, liquified material is extruded out of this nozzle and deposited on previous material or a build plate, following a path generated by a slicer software. As the material is deposited, it rapidly cools down, bonding with the previous layer. Once a layer is deposited, the build plate moves down (or the extruder moves up) of a pre-defined quantity, equal to the layer height, and the process is repeated until the last layer. Although this technology is mainly exploited for thermoplastic materials – the most common being PLA[1], ABS[2] and Nylon – it has recently been adopted for composite materials and metals.

[1] Polylactic Acid

[2] Acrylonitrile Butadiene Styrene

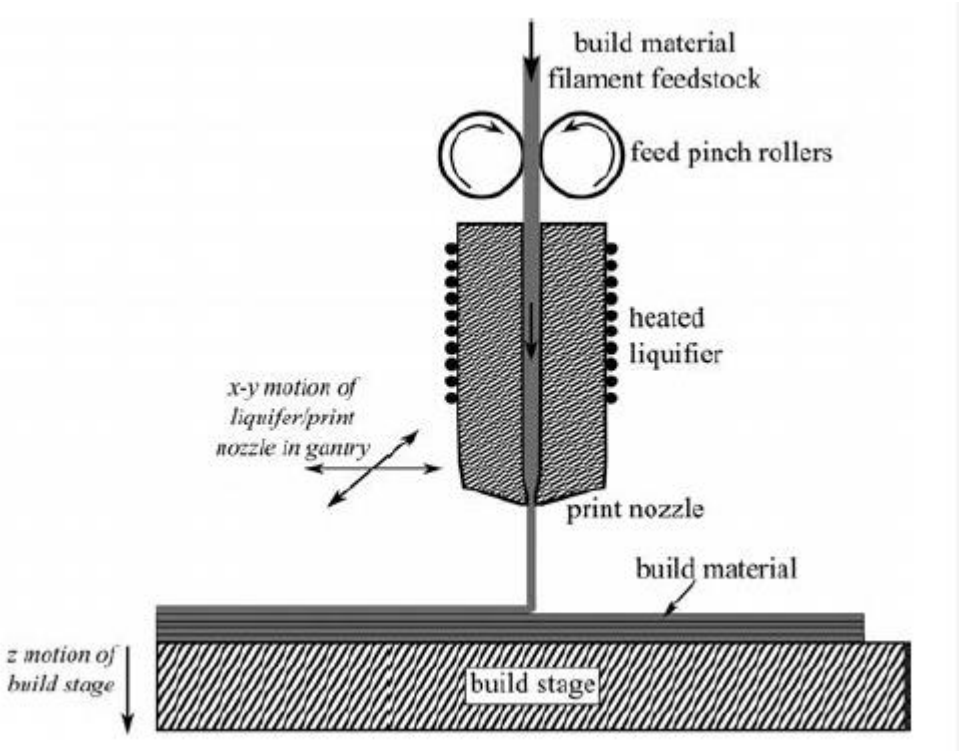

Figure 1: Illustration of typical extrusion-based AM process [10]

The most common industrial application of FDM is rapid prototyping, since it allows manufacturing of complex geometries and very fast lead time between computer design and production. Exploitation for functional parts is more limited, due to the poor mechanical performances of FDM products, although it is not uncommon. A noteworthy application of extrusion-based AM is home production, since the technology is very affordable and easy to use; in fact, the recent years have seen a widespread diffusion of FDM in homes, schools and laboratories, fostering the democratization of AM.

FDM is a relevant segment of a rapidly growing market, that of Additive Manufacturing. In their 2020 paper, Wickramasinghe et al. (2020) [11] provide a compound analysis of the expected growth of AM market from 2018 to 2026 throughout different industries, i.e., medical, automotive, food and aerospace. The predicted compound annual growth rate (CAGR) span from 18.2% in medical applications to 32.05% in food industry.

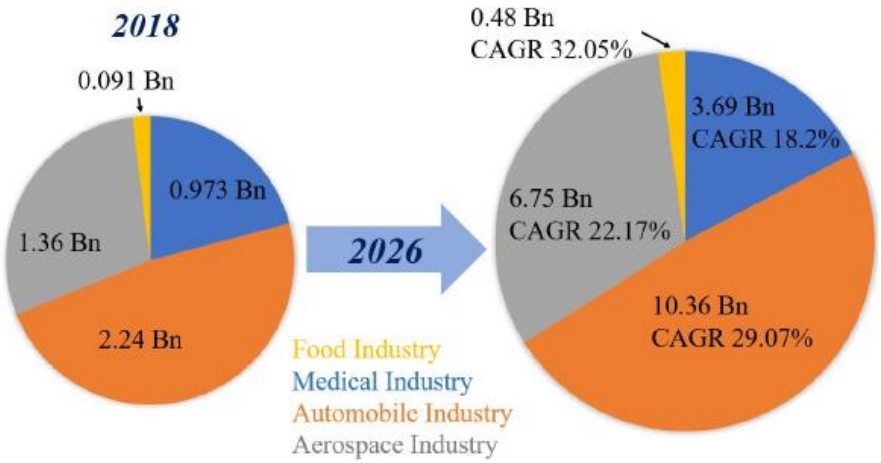

Figure 2: CAGR of AM market from 2018 to 2026, divided in the main industries [11]

They also observe that FDM is facing increasing interest mainly due to good cost effectiveness when compared to other AM technologies. To prove this, the number of scientific articles by year concerning FDM is depicted in Figure 3, showing an exponential growth in research. Furthermore, new applications are putting FDM under the spotlight (i.e., composite materials, LAAM, Bioprinting).

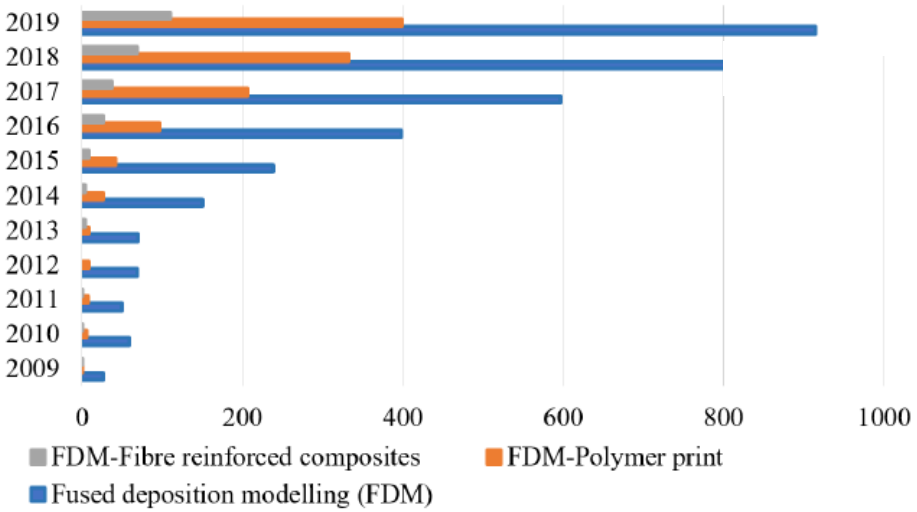

Figure 3: Number of publications on: FDM, FDM polymer prints and FDM fibre reinforced composites from 2009 to 2019 [11]

The process chain of FDM begins with the CAD file of the object that should be manufactured. From this input, a .STL[3] file - a format consisting of a representation of a volume through the discretization of its surface with triangles - should be generated. This file is then fed into a CAM software for 3D printing, which slices the .STL and generates the G-code, i.e., the list of sequential operations for the machine. This file is generated setting manufacturing parameters such as extruder speed and feed rate, extrusion temperature, need for supports, etc. The following step is printing, in which the electronic controller of the machine converts the commands contained in the G-code into actions for the motors, the filament roller and the thermistors of the print head. Once production is over, the process is completed with post-processing operations, usually consisting of supports removal and surface finishing. These have to be performed by human operators.

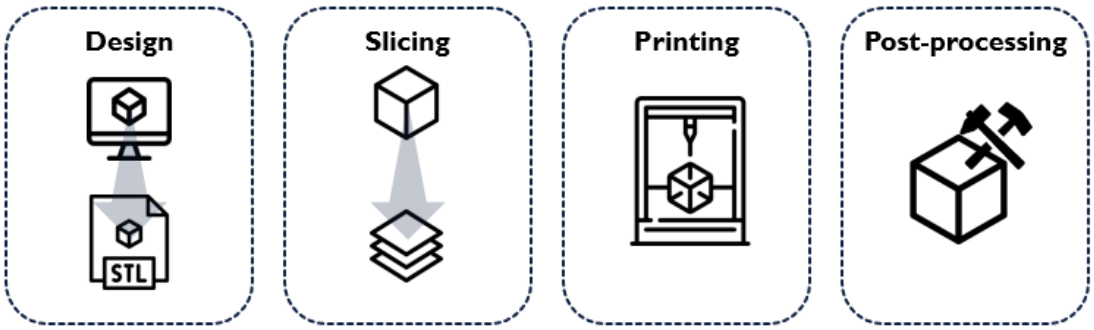

Figure 4: FDM process chain

To explain more in depth how printing phase works, FDM machines rely on rollers that push the filament through the print head. Here the material is melted, thus it is extruded through the nozzle in molten state. While the material is being extruded, two motors move the print head and/or the build plate to reproduce the 2-D path encoded in the G-code. This procedure can be easily visualised by thinking of cake icing. Once deposited, the material rapidly cools down (for example, ABS reaches the same temperature of the previously deposited layer within 2 s from extrusion [12]). Two consecutive layers bond thanks to the thermal energy of the newly deposited material,

[3] Standard Triangulation Language

which reheats the previous layer above glass transition temperature, thus leading it to a semi-molten state in which sintering between the two beads is possible. The success of bonding phase between adjacent beads and successive layers is fundamental to ensure good mechanical performances of the finished parts.

When compared with other AM technologies, FDM's advantages include its simplicity and the low cost. Its main disadvantages are linked to build speed, accuracy and material density. In fact, FDM has a very low throughput when compared with other AM techniques, it is affected by many defects that reduce its ability to reproduce nominal geometries and it is affected by high intrinsic porosity (see section 2.2.2). As briefly mentioned before, the interest in extrusion-based AM is rising not only due to its advantages, but also due to new applications that make the technology interesting, like composite printing, LAAM and Bioprinting.

(The insight of this section are mostly based on the textbook *Additive Manufacturing Technologies* [2])

2.1.1 Composite Printing

A "composite" is the combination of two or more materials with different properties in a way to act in concert, yet remain distinct because they don't fully merge or dissolve [13] . In extrusion-based AM, it is common to reinforce plastic materials with fibres or metal particles, in order to improve mechanical performances and achieve properties not attainable by pure polymer. An extensive analysis of the application of composites in FDM is provided by Wickramasinghe et al. (2020) [11]. They state that fibre composites in particular are the most common solution, encompassing materials like Kevlar, Carbon and glass, as well as some natural fibres. These composites further divide into short and continuous fibre.

The former group is manufactured by adding short fibres to the molten thermoplastic polymer. The most important parameters to keep under control while manufacturing short-fibre composites are: fibre orientation, mixture percentage and fibre size. In general, these materials face improved tensile strength and Young's modulus with respect to normal polymers, however at the cost of ductility, yield strength and toughness.

On the other hand, continuous-fibre composites require dedicated machines to be used. In fact, they rely on impregnation of a continuous fibre with molten polymer directly inside of the nozzle. Thus, FDM machines require two feeding mechanisms, one for fibre and one for thermoplastic filament. This process allows to have control over the fibre orientation. As for the comparison with respect to polymer, the same upsides and downsides of short-fibre composites stand true for continuous-fibre. However, the improvements in terms of mechanical performances are considerably higher with continuous-fibre than with short-fibre.

2.1.2 Large Area Additive Manufacturing

The term Large Area Additive Manufacturing (LAAM) refers to the application of AM technologies in a scaled-up context. Successful developments in this direction have been made at the Oak Ridge National Laboratory, with the realization of their Big Area Additive Manufacturing machine (BAAM). The prototype, initially developed in the Manufacturing Demonstration Facility of the laboratory, consists of an extrusion-based 3-D printer able to work with large volumes. In fact, the current system operates in a 6 m x 2.5 m x 1.8 m environment, and has a throughput of up to 50 kg/h. These figures translate in a great potential to impact sectors such as automotive, aerospace and energy [14]. In practical terms, it can be imagined as an upscaling of a common desktop FDM device, since it consists of a cartesian system. The main difference lies in its feedstock mechanism, which relies on fibre reinforced thermoplastic pellets, which are melted and extruded by a single screw extruder [15]. Since the application of BAAM technology has the chance to go beyond rapid prototyping and see exploitation for finished parts, many techniques are being proposed in the scientific literature to ensure high quality of prints.

Figure 5: BAAM printer realized by Cincinnati Incorporated at Oak Ridge National Laboratories [4]

2.1.3 Bioprinting

Bioprinting consists of the exploitation of AM techniques to manufacture biological models, biological systems and therapeutic products, exploiting as building blocks cells, proteins and biomaterials [16]. Bioprinting is born from the union of different research areas: Additive Manufacturing, Regenerative Medicine (RM) and Tissue Engineering (TE). RM refers to the ensemble of techniques which have as purpose the replacement or regeneration of human parts (e.g., cells, tissues, organs, etc); to work, these techniques either stimulate the body's repair mechanisms, or rely on growing parts in laboratory to then be implanted. TE, which is complementary to RM, relies on the combination of scaffolds, cells and biologically active molecules into functional tissues.

Bioprinting applications have evolved from the initial surgical planning models, inert implants, and cell-seeded scaffolds, to *in vitro*[4] bioprinted models. Developments of the technology foreseen in the near future encompass adoption of bioprinting to tackle

[4] Scientific expression used with reference to biological processes which happen in a laboratory

organ shortage or realization of patient-specific tissue replacement for his injuries. Among the main challenges of Bioprinting, listed by Sun et al. (2020) in their *Bioprinting Roadmap* [16], stands the printing process, which needs to be able to deliver cells with high survivability and high precision. In fact, low process repeatability and stability have slowed diffusion of these technologies.

2.2 Part defects

Given that AM scientific literature lacks a structured classification of extrusion-based AM defects (to the best of our knowledge), in the following pages an attempt at providing such classification is given.

Extrusion-based AM defects can loosely be divided in 3 families: *Geometrical defects*, *Internal defects* and *Superficial defects*.

2.2.1 Geometrical defects

This family refers to all the defects that concern an alteration in terms of shape or dimension with respect to the nominal profile. A very common cause for this type of alterations are defective motors, which due to blockage or slow-down can cause deviations from the path coded in the G-code. Since these events are very trivial, they are not a subject of scientific studies. Instead, two classes of Geometrical studies have a strong presence in AM literature: *Shrinkage* and *Warpage*.

Shrinkage is defined as homogeneous contraction of the part due to decrease of temperature of the finished part. Due to the thermal nature of FDM, some degree of shrinkage is inevitable. For this reason, it has been highly studied since the introduction of extrusion AM. This phenomenon begins after the glass temperature is reached and continues until the piece is in thermal equilibrium with the environment; therefore, the extrusion temperature has no impact on the amount of shrinkage, while environment temperature plays a key role, since the lower it is, the higher the contraction [17]. Contractions are relevant along the deposition direction of the bead, since shrinkage of cross sections does not affect the dimensional accuracy significantly. Shrinkage is generally countered via upscaling of the part directly through the slicer [10]. However, alternative approaches have been proposed in literature, for example Yaman (2018) [17] proposed a method for the compensation of inner holes shrinkage

through the shrinkage of an interior structure made of line segments, which by contracting stretch the holes, thus countering their tendency to reduce the diameter because of shrinkage.

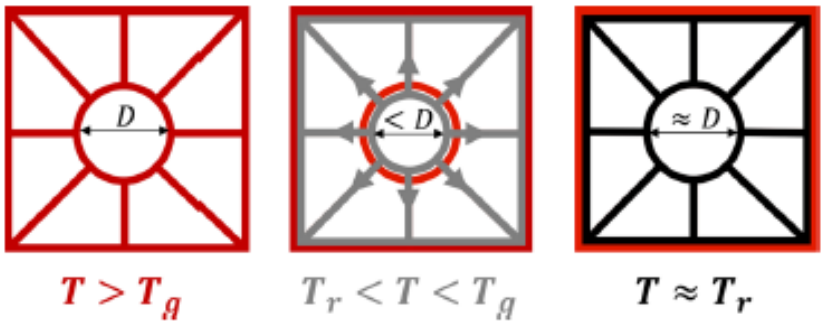

Figure 6: Visualization of approach from Yaman (2018); when shrinkage is over, the inner circle keeps its diameter thanks to the interior structure [17]

Warpage appears whenever shrinkage occurs inhomogeneously across the part during the build process. The main reasons for an inhomogeneous shrinkage of the parts in 3D printing processes are the time delayed solidification of layers and the influences due to the part geometry and boundary effects on the surface [18]. Schmutzler et al. (2016) [18] proposed a classification of warpage phenomena in 4 types: Curling, Trapezoid, Blocked shrinkage and Pincushion. *Curling* is a consequence of delayed shrinkage that manifests itself as an upward bend, most commonly at the edges of the part. Curling is the most common type of warpage defect, so much that in literature it is often referred just as warpage; It is generally countered via increased build plate temperature or application of adhesives on build plate [19]. *Trapezoid* is also caused by delayed shrinkage, but it manifests itself as an inclined distortion of side surfaces and a rounding of the lower part edges. *Blocked shrinkage* takes place when the part has cavities or undercuts; in these situations, we have a deformation of the contour of the cavity, pressed by shrinking material. Finally, *Pincushion* takes place on side surface and consists of subsidence of side planes. A visualization of the 4 classes is provided in the following images:

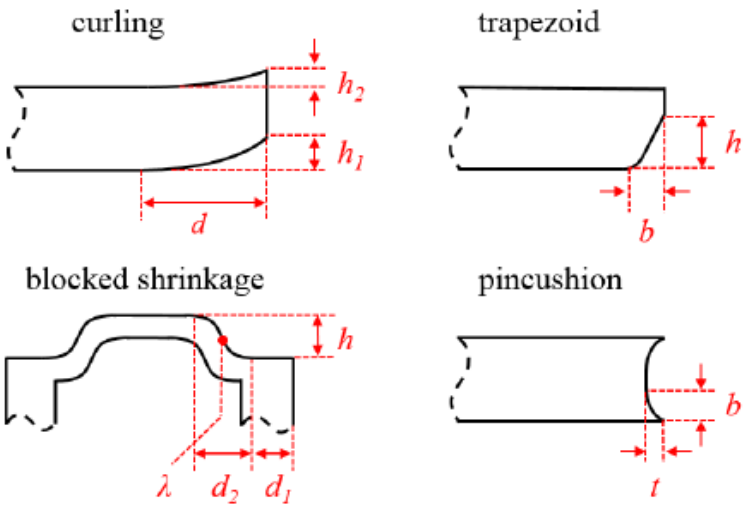

Figure 7: Four classes of warpage [18]

Wang et al. (2007) [20] attempted at identifying a mathematical relationship between a set of variables - number of layers, side length of part, environment temperature and shrinkage coefficient - and the entity of curling distortion (by them referred to with the generic term warpage instead of curling). What they discover is that distortion has an inversely proportional relationship with number of layers, a non-linear increasing relationship with length, a linear decreasing relationship with environment temperature and a linear increasing relationship with shrinkage coefficient. Thus, to avoid curling, they advise against long and thin parts and for high chamber temperature.

2.2.2 Internal defects

This family collects all defects internal to printed part, and thus all defects that cause a worsening of the mechanical performances of the finished product.

The first category of internal defects is *Cracking*, which refers to the formation of damages in the material structure that eventually lead to failure [21]. Cracks are generally the result of external causes, e.g., impact, light, chemicals or radiation. They can also generate as result of the inner stresses of shrinkage.

When a crack propagates through two adjacent layers, exceeding bonding forces, thus causing a separation of the layers, we talk about *Delamination*. A key factor

contributing to the formation of this defect is *incorrect bond formation*. In fact, the weaker the bonds between layers, the easier it is for such event to occur, up until the point in which no bond is formed and layers remain separated during production itself. Bonding happens when two adjacent beads are above glass temperature; in this semi-molten state, polymer chains are exchanged between the two beads in a phenomenon called sintering. Quality of bonding is generally measured via size of neck formed between beads.

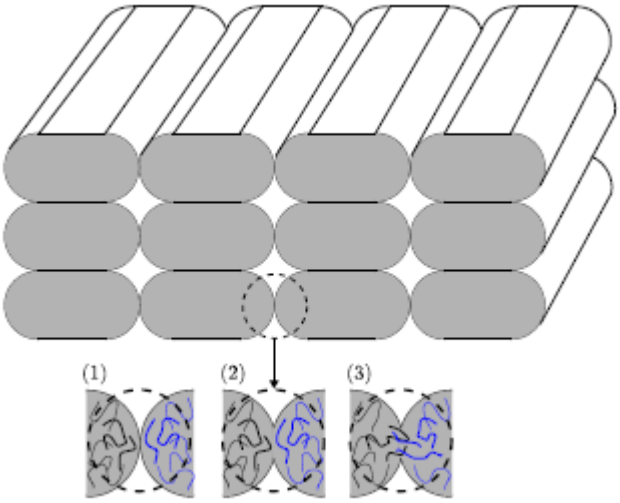

Figure 8: Bond formation articulated in 3 steps: (1) surface contacting; (2) neck growth; (3) diffusion at interface [22]

Bellehumeur et al. (2004) [23] found that extrusion temperature has a positive relationship with neck formation, and that it is a highly important parameter, since it determines the ability of previously deposited material to surpass glass temperature. However, excessive temperatures can worsen bond formation due to thermal degradation [10]. Beside thermal causes, lack of bond between layers can also be caused by incorrect nozzle height [24]. Delamination is also facilitated by *inter-layer voids*. While this type of porosity is inevitable in FDM processes due to nature of the process itself, it can be limited by reducing layer thickness [11].

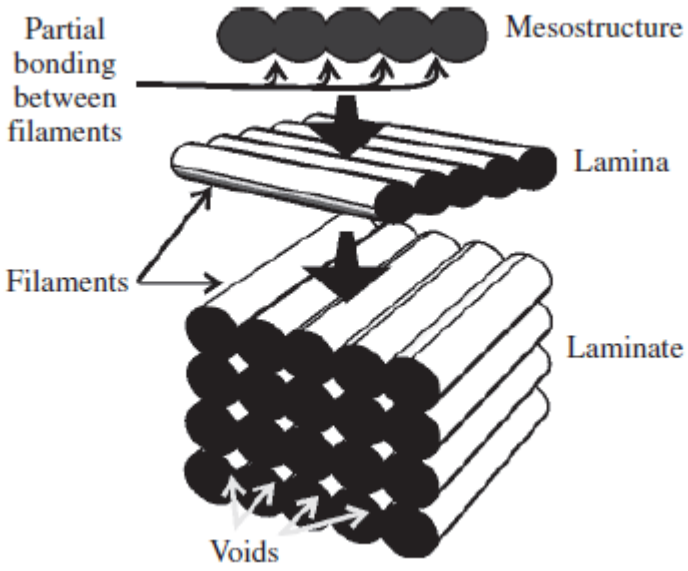

Figure 9: levels of analysis for FDM prototypes from Bellehumeur et al. (2004); the last level shows inter layer voids [23]

Incorrect bonding is also a possible cause for the formation of *inter-road voids*, which are small voids that form between adjacent tracks. Lack of bond between successive beads is less common than between successive layers, since material has less time to cool down before deposition of the adjacent bead than for the above bead, thus it is easier to reach glass temperature. The other cause for inter-road voids is incorrect material flow, which is generally linked to filament slippage or variations in filament volume. Under incorrect material flow phenomena falls *Under-extrusion*, the condition in which the flow rate of molten material is lower than nominal rate. This can be the result of a clogged nozzle, filament slippage or lack of sync between flow rate and nozzle speed, especially during acceleration [10] [19] [25].

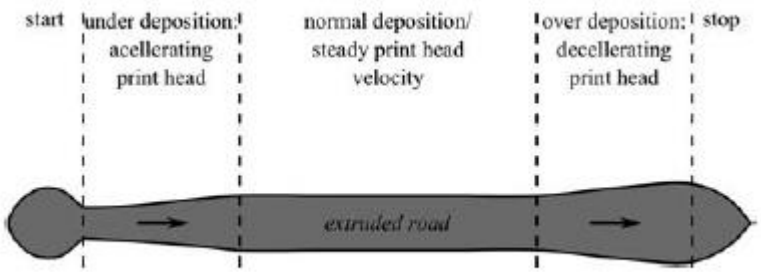

Figure 10: Illustration of under/over – extrusion linked to changes in nozzle speed [19]

A different class of internal defects is *filament porosity*, which refers to defects linked to presence of voids inside of the extruded material. A common defect of this kind are *Air bubbles*, the formation of bubbles in the liquified material that causes alteration of material structure [26]. Such phenomenon occurs at high temperatures, since the material is more viscous, thus more turbulence is generated while exiting nozzle, which creates air bubbles. Humidity also plays a key role, since the high temperature in the nozzle causes water boiling and this generates part bubbles.

In composite materials, *filament porosity* is a particularly relevant phenomenon due to the presence of fibres in the filament. High porosity can be caused by excessive percentage of fibrous material [11]. Furthermore, composite materials are subjected to a phenomenon called *fibre pull-out*, an issue concerning low adhesion between fibres and plastic matrix that is particularly relevant in continuous-fibre materials [27].

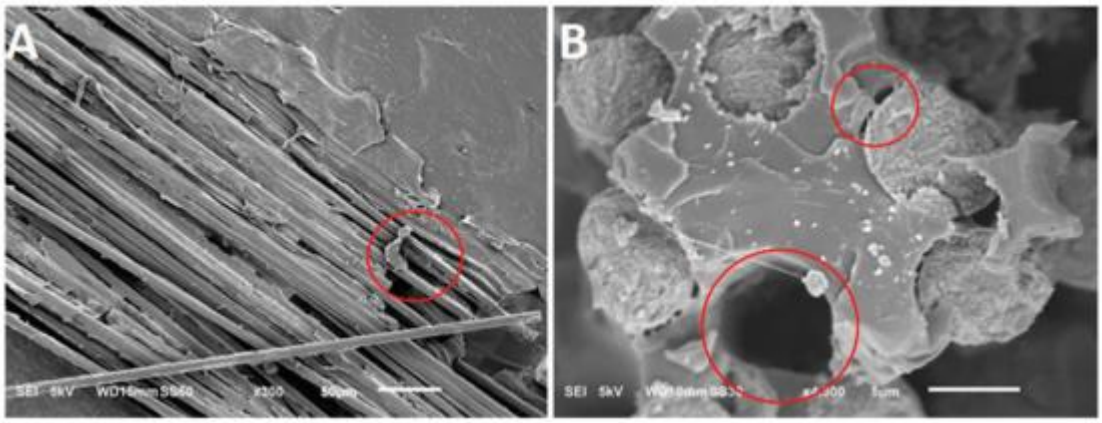

Figure 11: SEM observation of fibre-matrix interface in printed carbon reinforced composites: (a) poor resin infusion observed on the tow scale and (b) fibre pull-out with little matrix damage evidencing weak interface strength [28]

The last type of porosity classified in literature are *sub-perimeter voids*, gaps that form between infill and walls, resulting in weak connection between them that worsens mechanical performances. These voids can be countered by simply applying an offset to the perimeter or by adjusting flow rate of infill when close to walls [25].

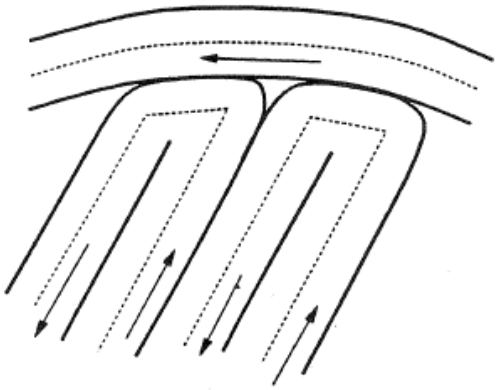

Figure 12: Sub-perimeter voids [25]

Finally, among internal defects we have *Over-extrusion residuals*, which consist of the deposition of excessive material, creating agglomerates that worsen roughness and can alter the geometry of the final product. Over-extrusion can be caused by incorrect flow rate or excessive temperature. In the first case issues arise mainly due to lack of sync between flow rate and nozzle speed, which causes output of excessive material during

deceleration and curves [19] [29]. Excessive nozzle temperature can instead cause leakage of molten material due to decreased viscosity, phenomenon called *stringing* [30].

Figure 13: printed object subject to stringing phenomenon [30]

2.2.3 Superficial defects

The last family includes all defects that cause alterations on the external faces of a part, increasing roughness. This family can be divided in two sub-groups: *top/bottom surface defects* and *lateral surface defects*.

The first sub-group is linked with defects that may arise during the printing of the first and last layer. For this reason, it includes many of those that are categorized as internal – i.e., *inter-road voids*, *sub-perimeter voids*, *filament porosity* and *over-extrusion residuals* – which cause an increase in roughness for these flat surfaces. To this list, *support removal burrs* should be included, defects consisting of roughness resulting from physical removal of supports during post-processing operations [25].

As for the second sub-group, it is linked to all defects causing increased roughness on lateral surface of the part. Beside *support removal burrs*, which may also concern this area, a common defect type is *staircase effect*, which consists of the translation of curved surfaces in a design to discrete steps in the z-direction results in a staircase or registering effect. This defect is caused by the slice method of manufacturing, which results in the impossibility to achieve perfectly round side surfaces. Methods for treating this effect range from varying the thickness of the slice to intermediate

processing [19] [25]. A similar defect is *chordal error*, which is the result of the approximation of all curvilinear surfaces as a series of linear segments, leading to a non-smooth surface of the part. This chordal approximation error is reduced as resolution in the .STL file is increased, also resulting in a correspondingly larger design file size [19] [25].

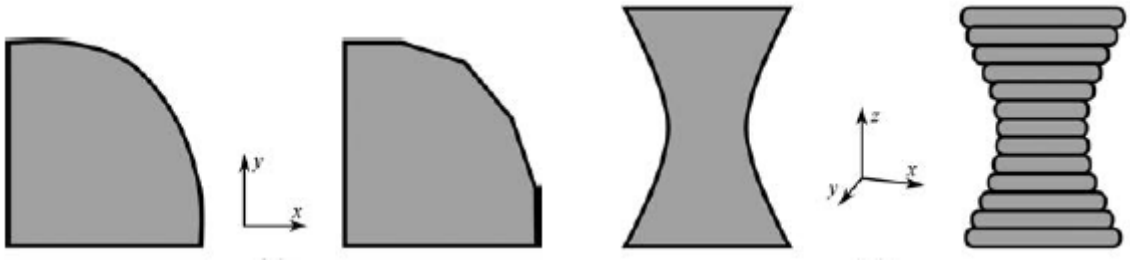

Figure 14: Chordal error (left); Staircase effect (right) [19]

2.3 Monitoring & Extrusion-based AM

The term *Monitoring* means to "observe and check the progress or quality of (something) over a period of time". For the sake of this work, with monitoring we refer to the identification of defects through signals extracted from the AM process, in contrast with *sensing*, which consists of the sole acquisition of data from the process.

Until the second half of the past decade, extrusion-based AM was not a target for monitoring for the AM scientific community, since differently from Powder Bed Fusion technologies, it was seldom exploited to manufacture finished products. Therefore, there was little interest in the industry to detect and avoid/correct defects for a process exploited mainly for rapid prototyping. This changed with recent trends of extrusion-based AM, like bioprinting, composite materials and LAAM. These applications fostered an interest in the development of techniques to detect defects during production and in search for knowledge of how to prevent them, moving towards zero-defect production.

Scientific papers dedicated to monitoring usually treat the application of a unique technology to detect a limited amount of defect types, typically just one. While a treaty of monitoring could be organized by technology adopted, in the following pages a division by defect type is provided, in order to keep strong ties with the previous chapter. In specific, we subdivide monitoring techniques in 4 clusters: *Geometrical*

defects, *internal defects*, *internal and superficial defects* and *Temperature variations monitoring*.

2.3.1 Geometrical defects monitoring

For what concerns geometrical defects, a lot of attention has been given to detection of warpage – in particular of curling (see section 2.2.1) – a very common issue with FDM. To detect it, different technologies have been adopted. Jin et al. (2020) [24] proposed a method based on the application of strain gauges on the build plate. In practical terms, by setting a threshold to the amplitude of strain, they're able to detect warpage. An approach combining computer vision and Machine learning has been successfully tested by Saluja et al. (2020) [31]; they applied a camera that acquires images of corners of a parallelepiped from the side view and trained a CNN[5] able to predict whether the corner is warped or not. Hu et al. (2020) [32] identified warpage via combination of thermal imaging and SVM[6], as well as under-extrusion and print failure states. Their approach is further explained in section 2.3.4.

A promising field of research concerning geometrical defects identification is the comparison between a reconstruction of the part geometry from data acquired during process and the nominal geometry. Moretti et al. (2021) [33] tested this approach by exploiting a cloud of points built with computer vision data acquired by a camera attached to the print head. Through the comparison between the cloud of points and the CAD file they managed to identify alterations of geometry in the form of large over-extrusion blobs on side surface.

[5] Convolutional Neural Network

[6] Support Vector Machine

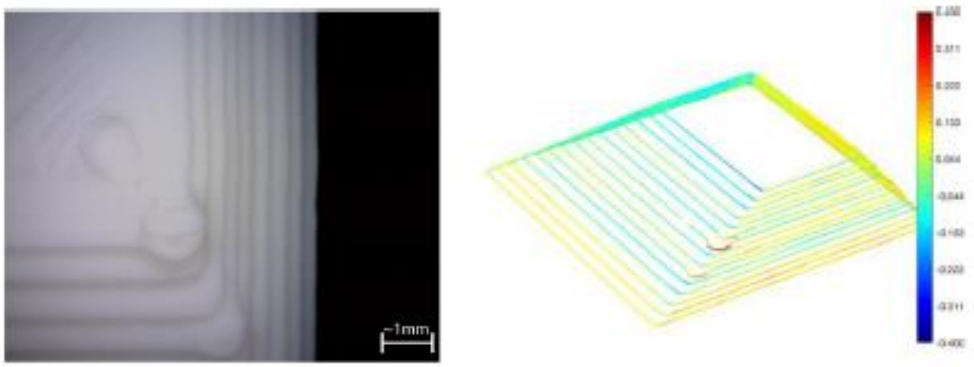

Figure 15: Forced over-extrusion blob (left); cloud of points reconstructed via computer vision with colomap built according to deviation from nominal profile (right) [33]

A similar approach is tested by Lin et al. (2019) [34], though the cloud of points is extracted through a laser scanner by acquiring a scan of each layer upon completion. These scans are then compared with the nominal profile of the very same layer from the CAD file to detect not only geometric alterations, but also under and over-extrusion phenomena. This is done by subtracting greyscale values from reference, which gives a reference of depth. Finally, He et al. (2019) [35] managed to identify staircase effect, gradual change and dislocations through the comparison between layer images, acquired with a camera from top, and nominal layer profile from CAD.

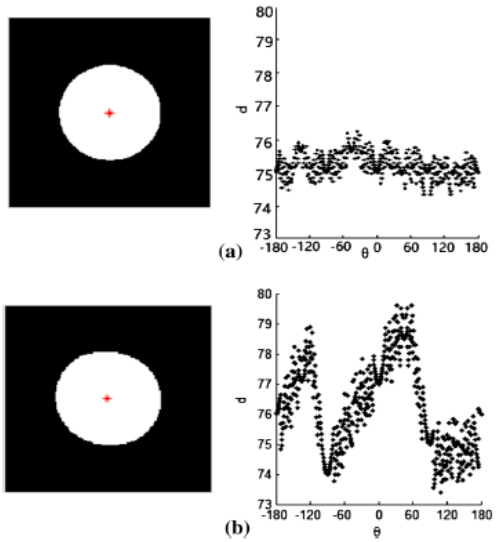

Figure 16: Geometric shape and its representation based on border signature, for: (a) the ideal profile, (b) the actual as-built profile [35]

2.3.2 Internal defects monitoring

Some attempts at detecting delamination with different methods have been made. For example, Jin et al. (2020) [24] built a CNN trained with images acquired by a camera placed sideview to detect whether the distance between nozzle and material is low, good, high or very high. This is done knowing from experiments that excessive height leads to lack of bonding, thus to delamination (see section 2.2.2). Therefore, the system predicts delamination by observing an erroneous setup of the equipment. They also observed that when distance is low, material distribution is irregular, and this leads to rough surfaces. A different approach for delamination detection has been proposed by Cummings et al. (2016) [36], who placed four piezoelectric transducers on the build platform to perform periodical inspections of the process via ultrasound chirp signals. Through a comparison between the detected response and an ideal one obtained through different experiments, they're able to assess whether delamination is present between the last two layers. Finally defects in the infill, in particular lack of bond with wall (sub-perimeter voids, see section 2.2.2) have been identified by Moretti et al. (2020) [37] thanks to layer images acquired by a camera placed in top view, showing how this setup can be useful to detect this kind of defect, though no algorithm for monitoring of this phenomenon was provided by them.

2.3.3 Internal and superficial defects monitoring

This category entails the identification of all defects shared between the internal and superficial families, such as inter-road voids, filament porosity and over-extrusion residuals. The identification of such events is performed by observing the layer being currently printed. The vast majority of approaches to monitor these defects rely on computer vision, generally combined with machine learning algorithms trained on layer images. A good example of this approach is the work of Jin et al. (2019) [38], who induced over-extrusion and under-extrusion states by altering the flow rate, and used the images acquired by a camera from top view to train a CNN able to determine whether the process is in good state, under-extrusion state or over-extrusion state.

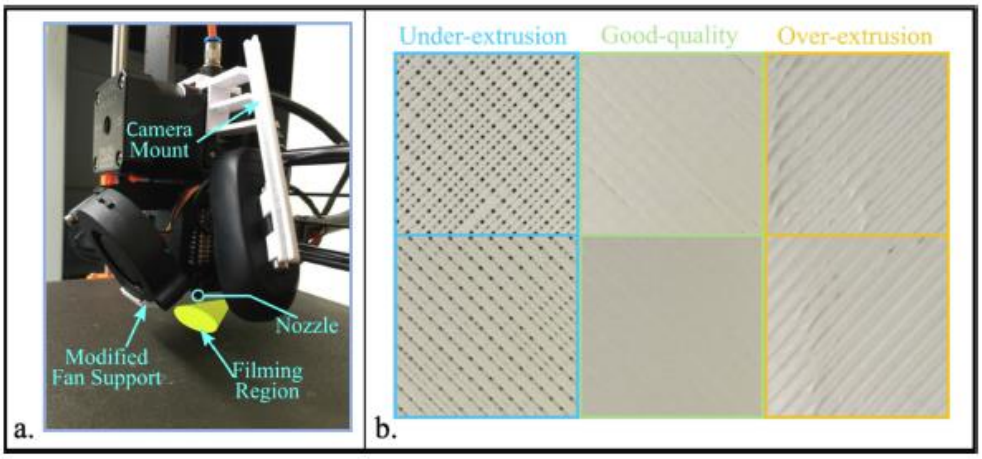

Figure 17: Jin et al. (2019) experiment setup (a); examples of Under-extrusion, Good-quality, Over-extrusion states (b) [38]

A different methodology, still relying on layer images acquired from top view, is the one proposed by Okarma et al. (2019) [39]; in their paper, they identify presence of voids or blobs in a given layer by dividing the image in fragments and testing the similarity of these sub-images through IQA[7] metrics. The method relies on the assumption that in nominal state, all fragments should be very similar, while fragments that differ from others may indicate presence of a defect.

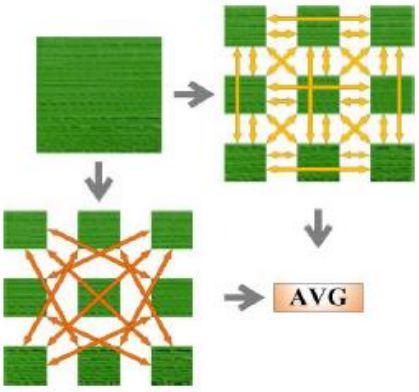

Figure 18: Illustration of the idea of the mutual similarity calculation between 9 image fragments [39]

[7] Image Quality Assessment

An example of identification of this class of defects that does not rely on computer vision is the aforementioned experiment from Lin et al. (2019) [34], in which the ability of laser scanning to measure the height of the currently deposited part allows to identify both voids and blobs.

2.3.4 Temperature variation monitoring

This last category of monitoring entails all techniques that exploit the temperature evolution along the process as mean for defect identification. Even though this approach is quite sensible, since extrusion-based AM are thermal processes, very few applications of thermal analysis for monitoring purposes have been proposed in literature. Instead, some papers are available on in-situ sensing, thus on the extraction of thermal data from the process, without the exploitation of these data to identify defects. However, these studies are very valuable, since they pave the way towards monitoring by developing effective approaches for data extraction.

The vast majority of approaches dedicated to temperature sensing rely on IR thermography, which means to exploit Infrared cameras to acquire images of the process that entail temperature information. The very first application of thermography to extrusion-based AM dates to a 2013 paper of Dinwiddie et al. (2013) [40], who adopted a sideview IR camera to extract temperature values in many locations inside the build chamber to identify inhomogeneities in temperature distribution. This paper also showed the potential of temperature analysis to gain a better understanding of the process by extracting temperature-space graphs of different layer for the production of cones. These graphs show skewness, thus highlighting uneven thermal behaviour, which in turn leads to uneven mechanical properties of the finished part. The reason behind such pattern is the print strategy, which began and finished new layer always on the right side.

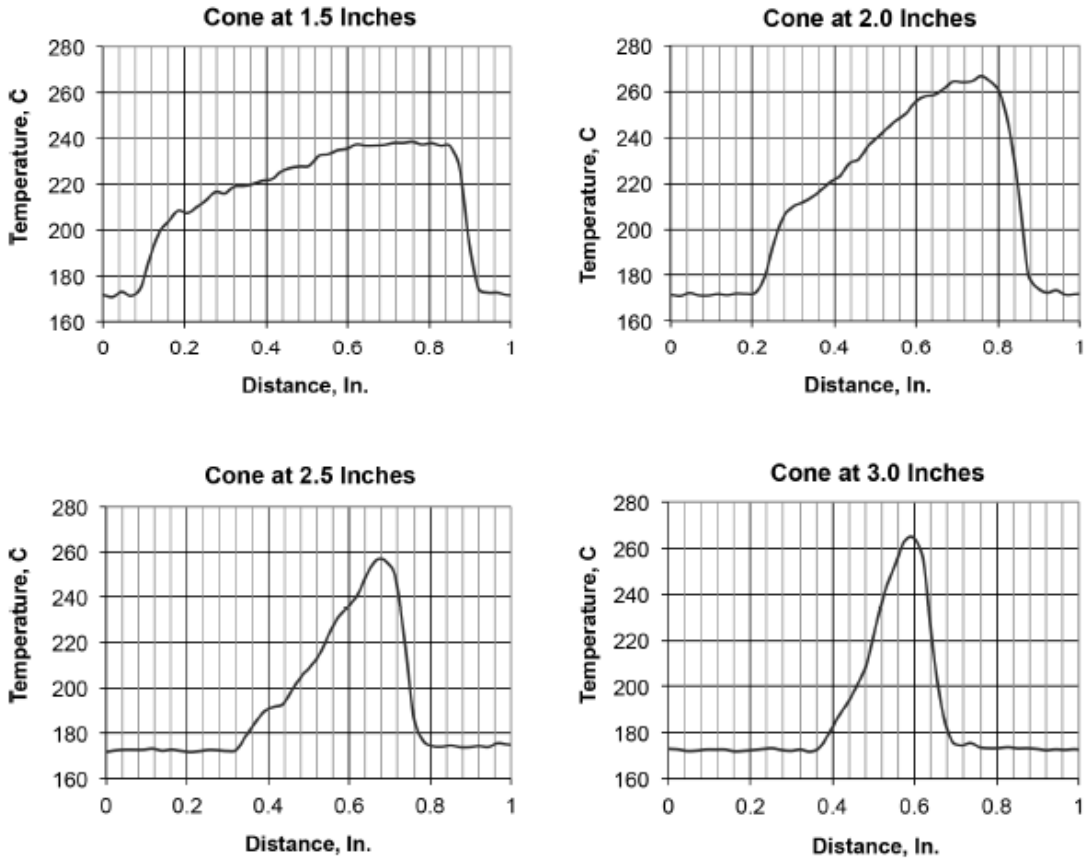

Figure 19: Spatial temperature distribution taken at different heights of a cone [40]

From this experiment on, nearly all thermography experiments are dedicated to the extraction of temporal or spatial temperature profiles. Seppala et al. (2016) [12] extracted temporal profiles from a region of interest (ROI) of both the newly deposited layer and the previous one, thanks to an IR camera applied from side view. They show how the past material reheats above glass temperature upon contact with hot filament, satisfying the necessary condition for bonding. The implicit idea behind this experiment is that such approach could be used to monitor correct bonding of layers, thus ideally to identify defects linked to incorrect bonding.

Both spatial and temporal profiles are extracted by Malekipour et al. (2018) [41], which developed an experiment to test impact of temperature distribution on mechanical performances by printing dogbone specimens with three different orientations, thus in turn with three different temperature distributions. What they observed is that better mechanical performances are achieved when distribution is the most even, a

very relevant insight for extrusion-based AM processes, since homogeneity in thermal behaviour becomes a main target to maximize quality of finished products.

Ferraris et al. (2019) [42] also exploit both types of profile, with a setup very similar to that of Seppala et al. (2016), though this time with the purpose of validating a model made to predict temperature evolution of a printed specimen. However, they also provide relevant insights on the influence of temperature evolution on quality of a part, observing that specimens with shortest infra-layer time (time passed before the nozzle gets to the same position in two consecutive layer), thus specimens in which little time is given to layers to cool-down before the following one, are those with the longest bonds, hence those with better mechanical performances.

However, minimization of infra-layer time is not necessarily a desirable strategy for quality improvement. In their experiment on application of thermography to BAAM to validate a temperature evolution model, Choo et al. (2019) [43] observed how excessive heat retention can cause failure of a print. What they did was printing a hollow pyramid with an increasing number of wall beads, from 1 to 3. In all three setups the print fails as it gets closer to the top, since the perimeter to cover becomes shorter, and with it infra-layer time, ultimately causing excessive heat retention that provokes a "melt-down" of the part. What changes is that the more beads are adopted, the higher the thermal mass of the part, therefore the print fails much earlier.

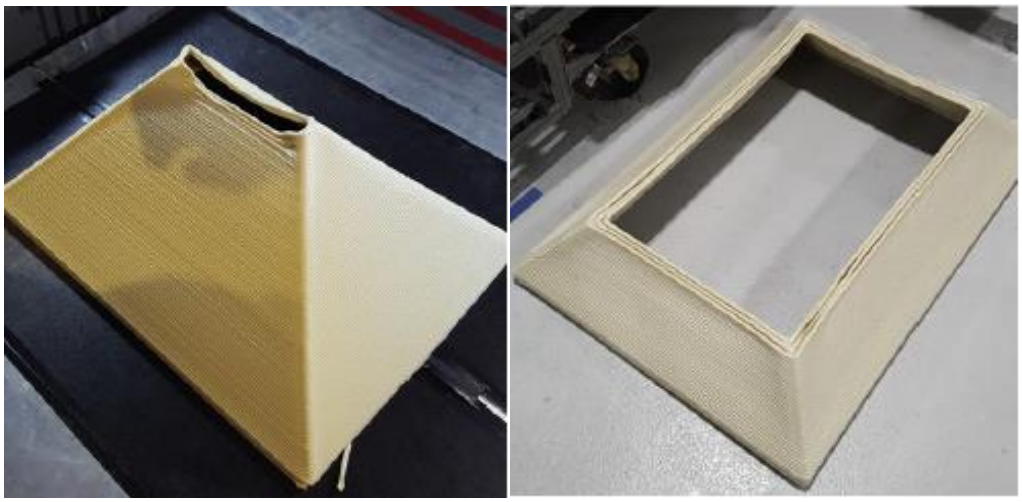

Figure 20: Print failure due to heat retention in two experiments: single bead wall(left); three beads wall (right) [43]

While the aforementioned papers don't treat directly defect detection, they are highly valuable for thermography monitoring in two ways: first of all, they explain in practical terms how to develop an IR camera setup and how to deal with some of the challenges of thermography; to give an example, Seppala et al. (2016) show how to deal with reflected IR photons coming from the hot nozzle. Secondly, they show two targets of monitoring: homogeneity of temperature distribution, which affects mechanical performances of the finished part, and steepness of temporal temperature profiles, which should be neither too high or too low, to avoid respectively lack of bond (due to rapid cool-down) and excessive heat retention (due to slow cool-down).

Nevertheless, FDM monitoring via temperature data is not a green field in scientific literature. Two methodologies to detect incomplete filling (under-extrusion), warpage and failure have been developed by He et al. (2018) [44] and Hu et al. (2020) [32]. Both approaches are developed on the same setup: an IR camera is installed on a FDM machine from top view, and for each layer of specimens with different geometries, a set of variables is collected once it has been finished – Mean temperature, Max temperature, Min temperature, temperature difference (Tmax -Tmin) and temperature variance.

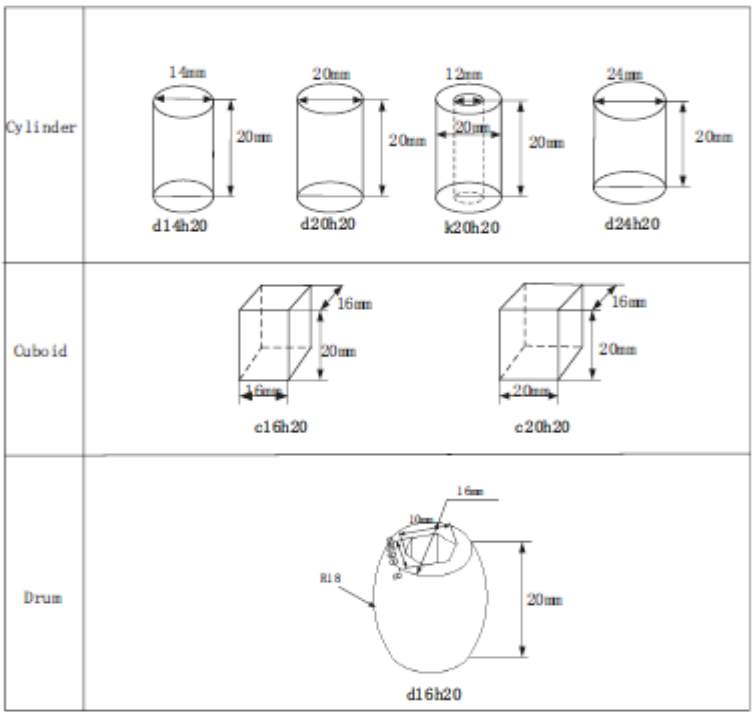

Figure 21: Shapes tested by He et al. (2018) and Hu et al. (2020) [32]

Along the print, defective states are induced by decreasing the nozzle temperature, thus causing clogging. Therefore, prints are characterized by four possible states: normal, under-extrusion, warpage and failure. In the work of He et al. (2018), Qualitative Trend Analysis is applied to the 5 metrics to identify layers in which a change of trend takes place. These setpoints are then compared with the real instants in which an alteration of nozzle temperature is performed, in order to assess how good the method is at detecting a change of state in the process. The experiment of Hu et al. (2020) is instead based on 4 metrics – variance is excluded – and correlation is searched between each of them and the four states. Having found such relationship to be stronger for the first three metrics – Mean, Max and Min temperature – they use them as independent variables of a SVM classifier, able to associate a given set of values to one of the four states. With this classifier, they manage to find areas corresponding to the four states.

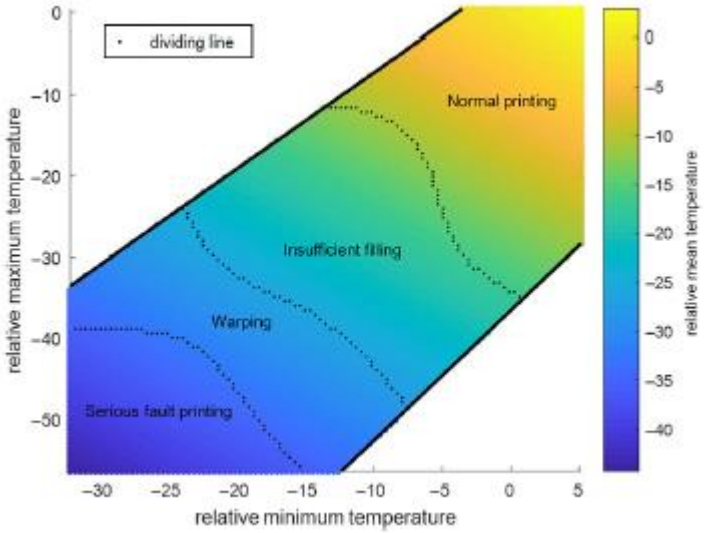

Figure 22: Classification regions resulting from SVM model by Hu et al. (2020) [32]

The strength of the two methodologies described lies in the ability to detect a change of state in the process with very few data – just 4/5 values per layer – and the generalization of the approaches, since they are tested on different geometries.

2.4 Indicators of spatiotemporal association

This section is dedicated to the treaty of indicators of spatial association and how they can be transposed to cases with spatiotemporal data. With *indicators of spatial association*, we refer to those metrics that assess the presence of patterns in the spatial arrangement of a variable. These indicators are commonly exploited in Geographic Information Systems (GIS), but can find proper use in contexts in which spatial information of a data distribution is available. The most common among them is *Moran's I*, which provides an assessment of spatial correlation among variables. If its value is positive, there is a tendency for similar values to be close to each other; instead, a negative value indicates that dissimilar values will be close to each other. The stronger the absolute value of the indicator, the more relevant the pattern, while values close to zero indicate randomness in the spatial arrangement.

To give a better understanding of the rationale of this indicator, we can imagine a matrix in which the only values a cell can assume are 1 or -1 (represented respectively with white and black). In the following image, we have a representation of three possible arrangements: the central one is random, thus Moran's I indicator will assume a value close to 0. In the right case we have a perfectly ordered arrangement with separation between black and white cells in two clusters. In this case, since similar values are close together, the value of *Moran's I* will be positive (and high). In the left example, we again have perfectly ordered values, but in a pattern that surrounds each cell with values different from itself. In this case, the value of *Moran's I* will be negative (and high).

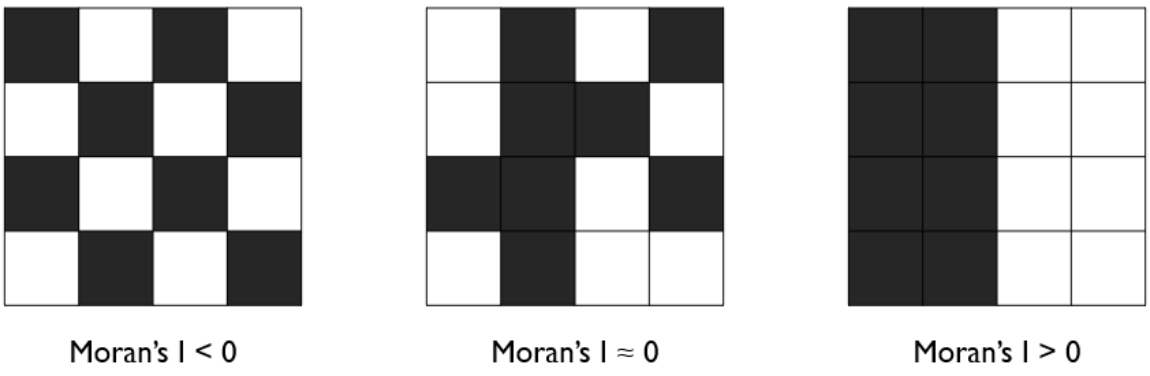

Figure 23: Evaluation of Moran's I in three experiments: negative spatial correlation (left), random distribution (centre), positive spatial correlation (right)

The mathematical formulation of *Moran's I* is the following:

$$I = \frac{N}{S_0} \cdot \frac{\sum_i \sum_i w_{ij} z_i z_i}{\sum_i {z_i}^2} \quad (1)$$

Where:

N: number of elements

S_0: sum of all spatial weights $\sum_i \sum_j w_{ij}$

w_{ij}: spatial weight expressing proximity between element *i* and element *j*

z_i : value of element *i* (expressed as deviation from mean)

Therefore, to compute *Moran's I*, we need a numerical value associated to each element (standardized) and a measure of distance between each couple of elements [45].

The evolution of this indicator that fostered its exploitation in different fields was provided by Anselin (1995) in its paper about Local Indicators of Spatial Association (LISA) [46]. The novelty of these indicators lies in their name: while *Moran's I* is a global metric, able to output a single value that describes the entire spatial arrangement, LISA are able to provide an indication of the spatial arrangement around a single element. What stands of notice is that the sum of all values of a local indicator for each element is proportional to its global counterpart. Thus, local indicators provide a decomposition of global indicators, which allows to have deeper insights about spatial patterns (from this point on, *Moran's I* will be referred to as *Global Moran's I*, while its LISA counterpart will be referred to as *Local Moran's I*).

As *Moran's I* is the most commonly exploited indicator of spatial association, its local counterpart gained a lot of popularity. Its formulation is the following:

$$I_i = z_i \cdot \sum_j w_{ij} z_j \quad (2)$$

Therefore, for each element *i*, an indicator is computed by multiplying its value times the weighted sum of values of all other elements. The interpretation of this indicator is similar to that of *Global Moran's I*: if the value is positive, it means that element *i* is surrounded by elements with similar value; if negative, element *i* is surrounded by elements of dissimilar value; if close to zero, it is surrounded by both similar and

dissimilar values. The absolute value of I_i is clearly influenced by the standardized values of the elements; in fact, if element *i* has value close to zero (which means it has an original value close to mean), and so do elements near it, *Local Moran's I* will be close to zero independently from similarity of values. This means that the indicator gives great importance to association of values that are far from mean.

A limit of indicators of spatial association is that time is not considered. In practice, we frame a set of values for the ensemble of elements in a certain moment of time and we evaluate spatial autocorrelation. But what if elements are associated to time series, and not just to unique values? Or what if we want to evaluate spatiotemporal patterns of events that happen in different places/instants? These questions pushed scientific literature towards methods to extend indicators of spatial association to spatiotemporal analysis.

In their literature review on spatiotemporal autocorrelation, Gong et al. (2020) [47] highlight how many attempts at extending Moran's I or similar metrics to spatiotemporal analysis have been performed by integrating time and space information, for example by using weights that express both spatial and temporal distance between elements or exploiting separately structured spatial and temporal weights. To comment on these approaches, the authors state: "From a physical perspective, it would make no sense to consider spatial and temporal properties of events in the same way. This is because there are significant differences between how events are related to each other in space and in time. […] Therefore, the direct integration of spatial and temporal dimensions of geographic data should be carefully reconsidered". In their paper, Gong et al. (2020) proceed to identify a method to assess spatiotemporal clustering of events which relies on a Voronoi-based sliding window, which allows them to determine which events are spatiotemporal neighbours. The method proposed is particularly effective when applied to cases with multi-categorical events.

If instead of measuring association of events we have a set of elements with constant spatial distance and values that evolve through time, a different approach is required. Such setup is tackled by Gao et al. (2019) [8], who consider cases in which elements are associated to time series. In a nutshell, the proposed methodology relies on extracting a unique numerical value (analogous to the z_i of Moran's I) able to express deviation of a time series with respect to the average profile. In this way, temporal information

is condensed in a unique metric. Once this metric has been computed, we are brought back to the original application of *Local Moran's I* with a set of elements associated to one value with a certain spatial distribution. The issue becomes how to sum up the information of a time series with a unique numerical value. The solution they adopted is the basis for the methodology proposed in this thesis.

3. Methodology

In the following paragraphs, we will describe the adopted methodology for the computation of spatiotemporal indexes, inspired by Gao et al. (2019), and the approach for indicators' monitoring. The methodology is then transposed to extrusion-based AM via a simulation study in section 4 and a real case study in section 5.

3.1 Methodology for Spatio-Temporal Phenomena Description and Diagnosis

The proposed methodology, inspired by Gao et al. (2019), is aimed at identifying the presence of local anomalies in datasets characterized by both spatial and temporal dimensions. More in details, this algorithm is meant for the analysis of time series associated to spatial coordinates. An explanatory example, taken from the aforementioned paper, is shown in the figure below. Here, each city map area, represented by a single cell, is considered to study the temporal evolution of taxi's take-on and drop-off, whose weekly temporal evolution is depicted in panels of Figure 24.

In a nutshell, the proposed methodology makes use of an updated version of a local indicator for spatial association (Local Moran's I, see section 2.4) to identify clustered events with similar temporal behavior.

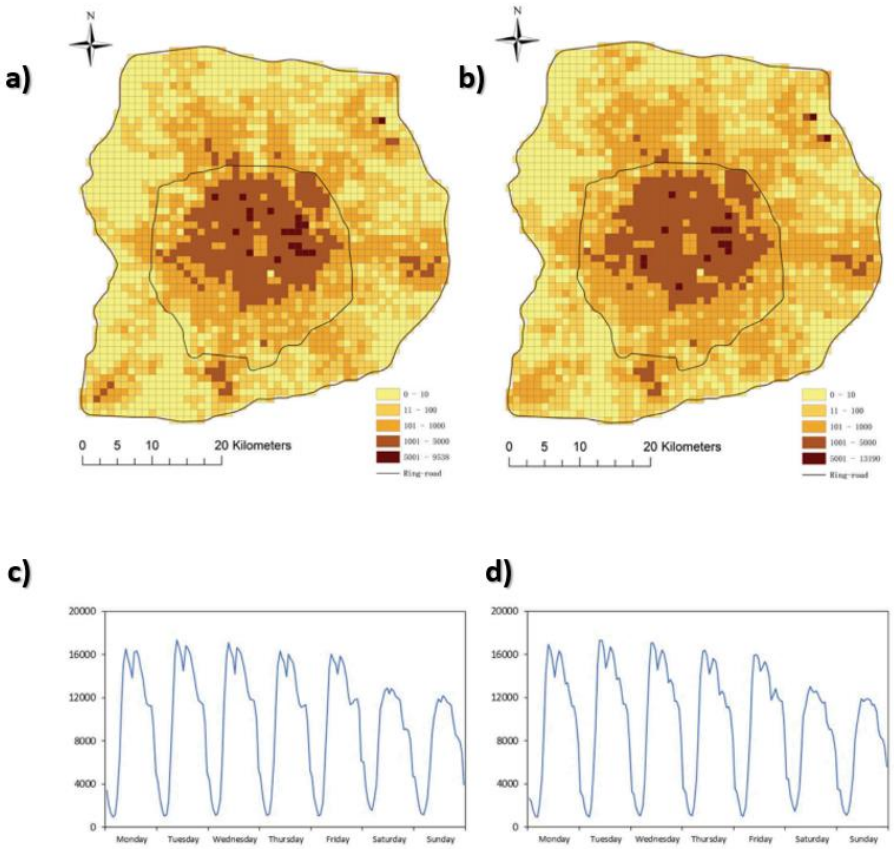

Figure 24: Example of spatiotemporal data taken from Gao et al (2019). (a, b) Total number of weekly take-on and drop-off in a city map, which is discretized in a regular grid. (c-d) Weekly temporal evolution of a single grid cell of respectively take-on and drop-off. [8]

In order to synthetizes temporal information of a cell in a unique value, Gao et al. (2019) propose the indicator ${Z_i}^T$ (also called Z index), which expresses how different the temporal profile of cell i is from a reference one (usually, the average of a set of time series). The indicator is built as multiplication of two components: one that expresses difference in terms of shape (called *CORT component*), the other in terms of magnitude (called *Area Difference component*). The formula proposed is the following:

$$ {Z_i}^T = \varphi\big(CORT(X_i, X_{avg})\big) \cdot (V_i - V_{avg}) \qquad (3) $$

The component relative to shape is obtained through the first-order temporal correlation index (CORT) between the time series of element i (X_i) and the average time series (X_{avg}). The formula of this index is the following:

$$CORT(X_T, Y_T) = \frac{\sum_t^{T-1}(X_{t+1} - X_t)(Y_{t+1} - Y_t)}{\sqrt{\sum_t^{T-1}(X_{t+1} - X_t)^2}\ \sqrt{\sum_t^{T-1}(Y_{t+1} - Y_t)^2}} \quad (4)$$

Which can be seen as the correlation index between two vectors containing the differences between consecutive elements of two time series. The values of CORT are then limited to the interval [-1, 1]. The authors proceed to remap CORT values to the interval (0,2) with an exponential adaptive tuning function defined as:

$$\varphi(x) = \frac{2}{1 + e^{2x}} \quad (5)$$

After the application of this transformation - which can be visualized in Figure 25 - the term is bigger when the difference in terms of profile shape is bigger. Therefore, profiles very similar to the average one will tend to have values closer to 0, profiles not correlated with the average one will result in value close to 1 for the first component, thus the resulting Z index will be driven by the second one. Finally, profiles with behaviour opposite to the average one will see a magnification of the second component in the computation of Z index, due to the value higher than 1 of the first component.

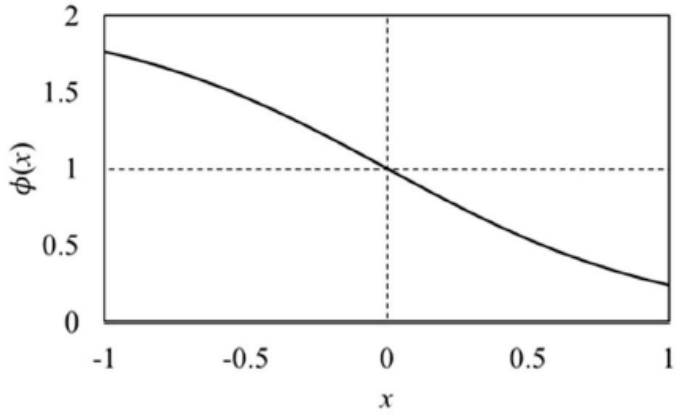

Figure 25: Tuning function $\varphi(x)$ [8]

The other component of indicator ${Z_i}^T$ consists in the so defined magnitude, i.e., the area outside each time series. The areas outside the target time series and the average temporal profile in the period [1, T] are respectively expressed as V_i and V_{avg} and they are computed as in (6). The difference between V_i and V_{avg} accounts for deviation in terms of magnitude.

$$V_i = \int_1^T X_i \, dt \tag{6}$$

The average temporal profile used to compute CORT component and Area difference component is computed by averaging the temporal profiles in each time instant. A reasonable alternative to this approach would be to exploit a theoretical profile, obtained by a priori knowledge. This approach prevents the generation of misleading results given by an erroneous estimation of the average temperature profile, which might be influenced by outliers. However, target temporal profiles are not always known or easy to compute. Moreover, they would possibly introduce an additional source of error, given by the target profile's estimation.

Once ${Z_i}^T$ has been computed for each element *i*, the computation of Local Moran's I for each location is performed by using the equation proposed by Anselin (1995), explained in detail in section 2.4, which is hereafter reported.

$$I_i = z_i \cdot \sum_j w_{ij} z_j \tag{2}$$

where z_i is set to ${Z_i}^T$, and w_{ij} are the spatial weights, usually computed as the inverse of Euclidian distance between the ith and jth location.

The usage of ${Z_i}^T$ as z_i is perfectly reasonable, since in the original formulation z_i is a metric that expresses deviation from mean, and so works ${Z_i}^T$, which expresses deviation from an average profile. Spatial information is condensed in the weights w_{ij}, which are computed to prioritize closer values.

As explained in depth in section 2.4, this indicator provides an assessment of how the z metric for element *i* correlates with other temporal profiles associated to spatial locations *j* in proximity of the location *i*. Positive values for I_i indicate positive correlation, thus element *i* will be surrounded by elements with similar value (same sign), while negative values indicate negative correlation, thus element *i* will be surrounded by elements with dissimilar z metric (different sign). The closer I_i is to 0, the closer to randomness in spatial distribution are Z indexes. By construction, indicator I_i will prioritize Z indexes with high absolute value, therefore it will highlight

more correlation of elements that have behaviour far from mean. The image below depicts the workflow so far described.

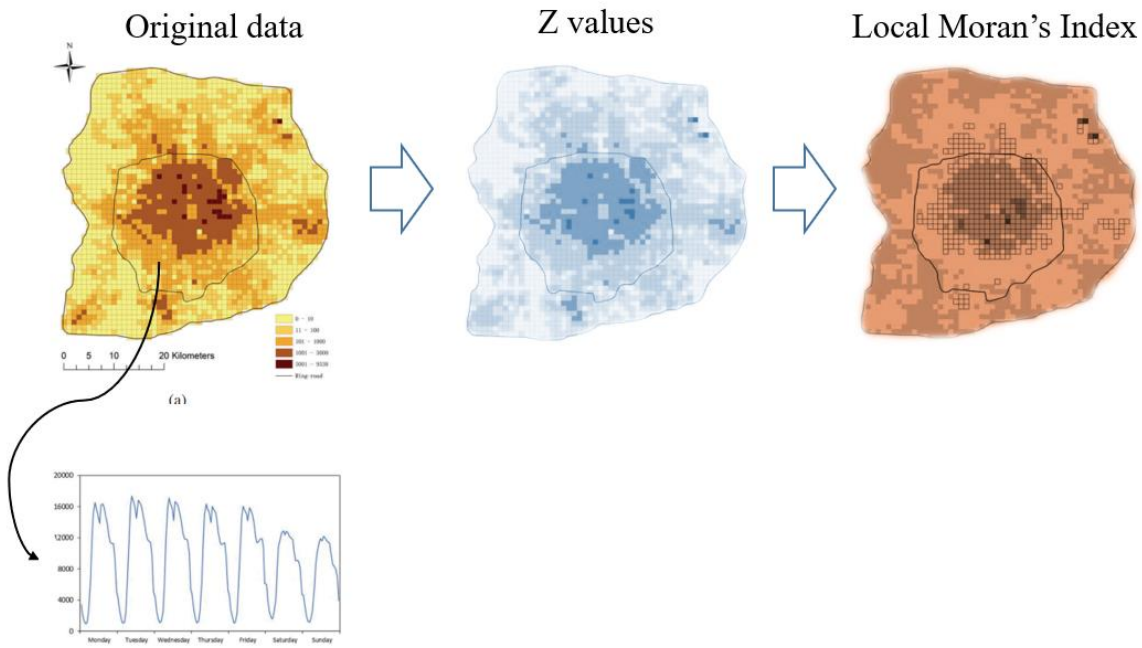

Figure 26: Workflow of indicators extraction: starting from the time series, Z indexes are extracted; then these become the input for computation of Local Moran's I

Once Local Moran's I are calculated, Gao et al. (2019) identify the index values that are statistically different to the others by using the p-value associated to each value. To extract said value, a method based on multiple randomizations is proposed, as detailed in Anselin (1995). The reason why this step is performed is to identify the elements that are characterized by anomalous spatiotemporal association.
Given the original arrangement of Z indexes, 1000 randomizations are performed, thus changing randomly the position of each Z index. For each of the 1000 randomized Z index arrangements, Local Moran's I are computed for each cell. The resulting values are exploited to build an Empirical Cumulated Density Function (ECDF). The ECDF is then used to compute the p-value of the original Moran's values. Threshold values on the p-values (e.g., 0.025 and 0.975, corresponding to selection of extreme 5%) are set to identify those values that are statistically different to the Z population. The figure below depicts this process.

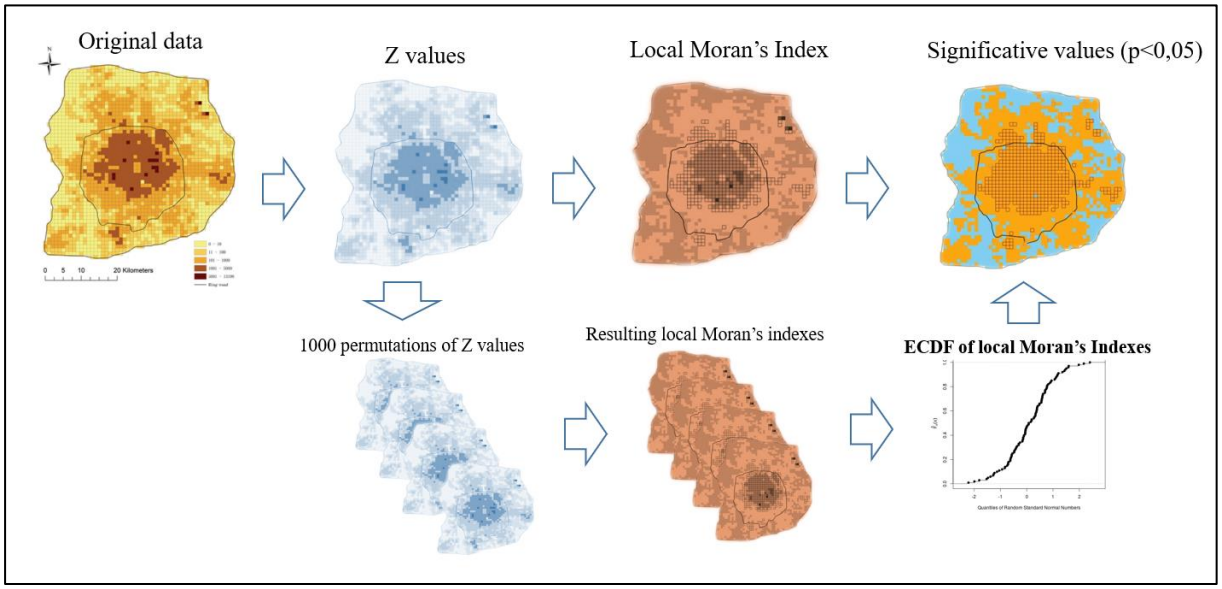

Figure 27: Expansion of precedent workflow with diagnostic step. Top line shows the workflow of the methodology, the bottom branch shows the step for computation of ECDF needed for assessment of significant Local Moran's I values

3.2 Monitoring Approach for spatiotemporal indicators

As shown in the previous paragraphs, Gao et al. (2019) discuss spatiotemporal pattern analysis and diagnostic to detect time series (collected in a given time interval T) that are significantly associated to those of surrounding location. However, the methodology lacks in automatic rules for anomaly detection when multiple consecutive time intervals are considered. In this section, we proposed an approach to monitor the presence of spatiotemporal phenomena in different time intervals. This approach will be useful for the real case study and, in general, for in-situ monitoring in Additive Manufacturing, where the presence of spatiotemporal phenomena can be analysed layerwise (therefore, each layer is a distinct time interval).

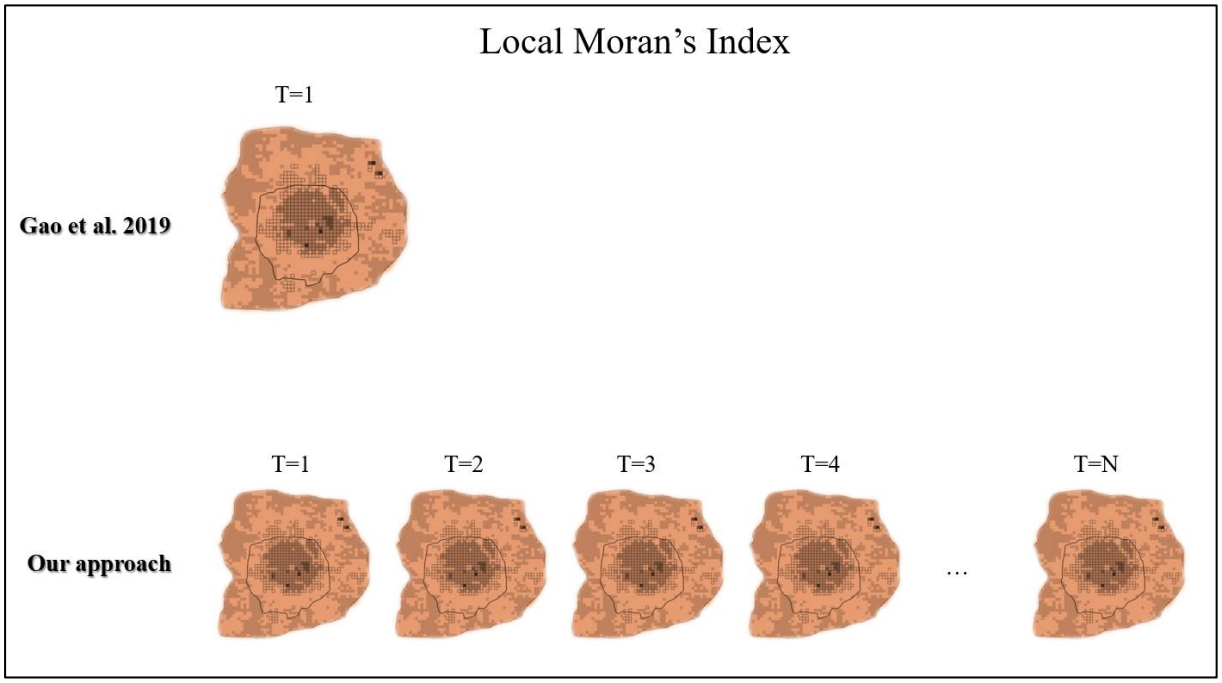

Figure 28: Difference in approach from reference paper. While they analyse a unique dataset, we consider availability of many, each corresponding to a layer of AM processes

For the monitoring purposes, two global metrics were considered, i.e., Global Moran's I and the average value of $Z_i{}^T$ (called mean Z index). These are able to associate each time interval (from now on called layer) a unique value that describes its behaviour. Global Moran's I (which is the result of the average value of all Local Moran's I) provides an assessment about the presence of correlation patterns in a given layer, which can consist of clustered areas with similar temporal behaviour (when positive), or proximity of cells with dissimilar behaviour (when negative). In contrast, the average value of $Z_i{}^T$ should reveal the presence of unusual values in case of spatially sparse defects. In absence of anomalies, this value should be close to 0, while high positive or negative values highlight the presence of temporal profiles significantly different from average, independently from their spatial distribution.

Here we propose a statistical process control methodology based on traditional Shewhart control charts (CC). Given a set of spatiotemporal data, associated to different time intervals, a control chart can be built for each indicator using the following values for the centre line (CL) and the upper and lower control limit

(respectively, UCL and LCL). Therefore, for each of the two global metrics m, control limits are computed as:

$$CL = \mu_m \quad (7)$$

$$UCL = CL + K_{CC} \cdot \sigma_m \quad (8)$$

$$LCL = CL - K_{CC} \cdot \sigma_m \quad (9)$$

where μ_m and σ_m are respectively the metric's mean and the standard deviation. Under indicator's normal distribution assumption, we can set parameter $K_{CC} = 3$ to identify upper and lower control limits, and know that it will correspond to type-I error α = 0.27% for individual charts, but to an overall $\alpha \leq$ 0.54%, due to Bonferroni inequality, which states that when N charts with given α are adopted, the overall type-I error will be $\alpha' \leq \sum_{i=1}^{N} \alpha_i$.

When Global Moran's I and the mean Z index are monitored together, we expect to observe four different scenarios:

1. *No alarms*. This means that neither clustered anomalous time series nor isolated ones occurred.
2. *Alarm on CC based on Z and no alarms on CC based on Moran's index:* This case should signal the presence of cells with abnormal temporal behaviour in a considered time interval, but distributed randomly.
3. *Alarm on CC based on Moran's index and no alarms on CC based on Z:* This is the opposite scenario with respect to the aforementioned point. The CC should signal the presence of abnormal association of temporal profiles - such as clustered defects - in a considered time interval, while overall Z index distribution is not skewed towards one type of anomaly.
4. *Both CC release an alarm*: this scenario should detect the presence of both defects' typologies.

These scenarios are going to be explored in depth throughout the simulation section.

3.3 Methodology sum-up

When considering the transposition of the points explored in the previous paragraphs to extrusion-based AM processes, the methodology can be summed up into a three steps process:

1. Indicators' extraction – given a dataset consisting of temperature profiles in different locations of a layer, Z index values should be computed for each location, having extracted the average profile of a layer. The Z index values should then be exploited to compute Local Moran's I of each location.
2. Anomalies detection – through the assessment of Global Moran's I and mean Z index associated to a layer, it is possible to detect the presence of spatiotemporal association and/or abnormal thermal behaviour, signalled by high or low values of the metrics.
3. Diagnostics – if anomalies are believed to be present in a layer as result of signal in the CC, an assessment of the local Moran's I values should allow to establish which cells are linked to correlation phenomena, by computing the p-value of the metric thanks to the ECDF extracted via multiple randomizations.

4. Simulation

In this section, we will apply the methodology described in the previous paragraphs to a simulation study. More in detail, we will simulate three classes of defects with different spatial characteristics (one clustered area, two clustered areas and many spread points). For these cases, a sensitivity analysis on defect magnitude and defect dimension will be performed.

Figure 29: Examples of the three classes of defects: single cluster (left), sparse defects (centre), two clusters (right)

We simulated 9x9 matrices, where each cell is associated to a temperature profile. Spatial information consists of the coordinates associated to each cell, which are simply extracted from the column and row indexes. These will then be exploited to compute the weight matrix W used for Local Moran's I.

For each element of the 9x9 matrix, we will associate a time series which simulates a temperature profile of a BAAM process. These thermal profiles are generated are generated using preliminary information on temperature decay and, generally speaking, temperature profiles characteristics taken from a previous study [48]. In detail, this study shows that thermal profiles can be adequately modelled using a linear function where the logarithm of temperature depends on time through a second-order polynomial function. This relationship is shown in the following equation.

$$\ln T(t) = \beta_0 + \beta_1 t + \beta_2 t^2 + \varepsilon_t \quad (10)$$

Where :

$\ln T(t)$: natural logarithm of temperature T as function of time

$\beta_0, \beta_1, \beta_2$: coefficients of the second order polynomial function

$\varepsilon_t \sim \text{iid } N(0, \sigma)$: residual between polynomial function and observed temperature logarithm at time instant t

From the aforementioned study (which will be deeply described for the real case study in Section 5), the values of the model's coefficient have been estimated as shown in the table below.

	MEAN	STD. DEVIATION
β_0	5.421	0.0105
β_1	-2.165 e-4	1.773 e-5
β_2	5.18 e-8	1.0129 e-8
ε_t	0	0.0005

Table 1: Descriptive statistics of thermal profile coefficients

Moreover, we a high correlation between β_2 and β_1 is observed. Correlation coefficients between coefficients from all profiles of the dataset are reported in the following table:

	β_0	β_1	β_2
β_0	1	-0.49	0.39
β_1	-	1	-0.85
β_2	-	-	1

Table 2: Correlation between thermal model coefficients

Assuming β_0, β_1, β_2 normally distributed, model's coefficients are randomly generated for the creation of in-control thermal profiles. In specific, β_0 and β_1 are generated following a normal distribution with mean and standard deviation specified in Table 1, while β_2 is computed with a regression model based on β_1. This regression model is built taking profiles from the dataset mentioned above, and it results in equation:

$$\beta_2 = -0.0000001 - 0.000523 \cdot \beta_1 \quad (11)$$

A timespan of T = 1800 frames is exploited as t variable (thus of 60 seconds, given the framerate of 30 fps), therefore for each element we generate 3 β coefficients and 1800 errors, obtaining a profile with variability similar to those available in a real case.

In order to assess ability of methodology to detect presence of defects, some thermal profiles have been altered in shape, by altering the β_1 coefficient. Such alteration mimics changes in terms of cooling rate of the profile, thus changing the slope of the curve. In real cases, this kind of alteration can be the result of phenomena like over/under-extrusion and filament porosity. In practical terms, when thermal profiles are simulated, *K* standard deviations are added to coefficient β_1 in defective cells. Different values of *K*, as well as different values of defect dimension, will be investigated to study the methodology's performance. The image below depicts an example of altered thermal profiles (*K*=3, defect dimension = 3x3 cells). This graphical example will be taken in the following paragraph to discuss the results of methodology application.

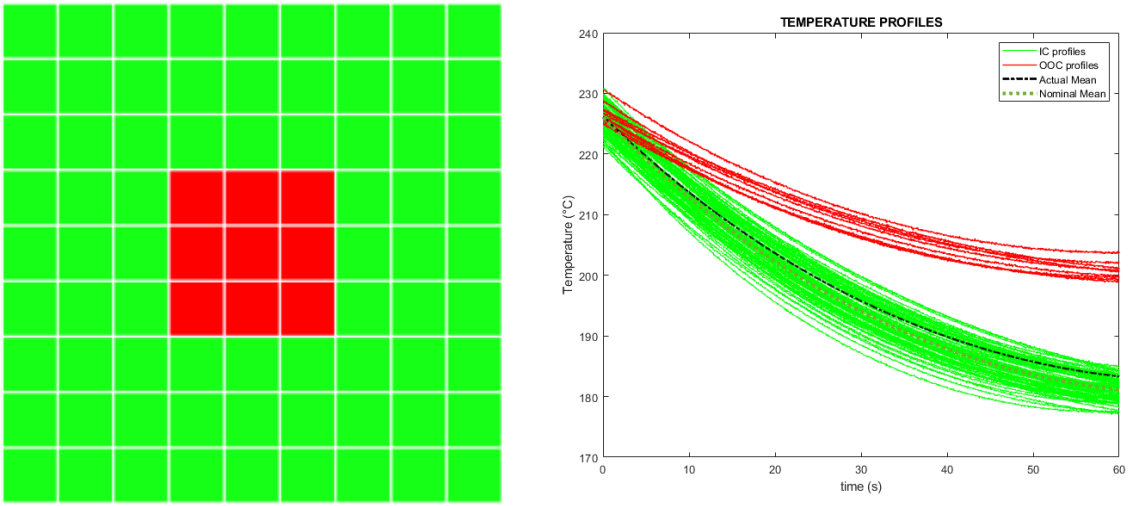

Figure 30: Simulated matrix layout (left); simulated profiles in the example under analysis (right); in both, green is used for in-control elements, red for OOC ones

4.1 Example of simulated defect and methodology application

In this paragraph, we will show the application of the methodology for spatiotemporal analysis to a simulated scenario. A square defect with size of 3x3 cells with K = 3 is placed in the centre of the 9x9 matrix (thus, coefficient β_1 for those cells is incremented by $3 \cdot \sigma_{\beta_1}$). Figure 30 provides a visualization of the defect and of the temperature profiles, coloured according to whether they are defective or not. In the graph above, both the actual average profile and the theoretical one (the one computed without OOC profiles) are shown. From their assessment, the leverage effect of defective profiles on the empirical average profile can be seen. It results in an average profile with lower cooling rate than the theoretical one, thus being impacted by the slow-cooling defective cells.

As mentioned in section 3.3, the first step consists of the computation of Z index, thus in turn of CORT and Area Difference components. A visualization of the three variables in the simulation example previously described is provided hereafter.

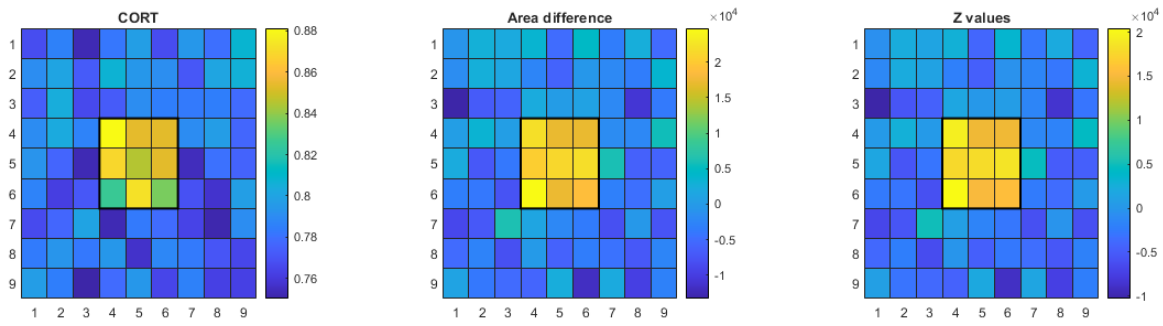

Figure 31: CORT component, Area difference component and Z index visualization through heatmaps

As we can see from the heatmaps, both components highlight the presence of the defective area, which assumes higher values than in-control profiles. An explanation for the values assumed can be provided. CORT component is higher for defective cells since their profiles will be less correlated with the average one than in-control profiles. Thanks to the $\varphi(x)$ function (see section 3.1), lower correlation is remapped to values closer to 1, while higher correlation is remapped to lower values (closer to 0). As for Area difference component, profiles with lower cooling rate result in higher area under

curve. As a natural consequence, their combination into the Z index also highlights the defective cells.

The Z index is then exploited to extract Local Moran's I value for each cell. In order to compute the weight matrix W, distances between each couple of cells must be available. Such distances are computed using the Euclidean distance on the coordinates of each cell, where the system of coordinates coincides with rows and columns indexes. The results for local Moran's I computation in the experiment provided are shown in the following heatmap.

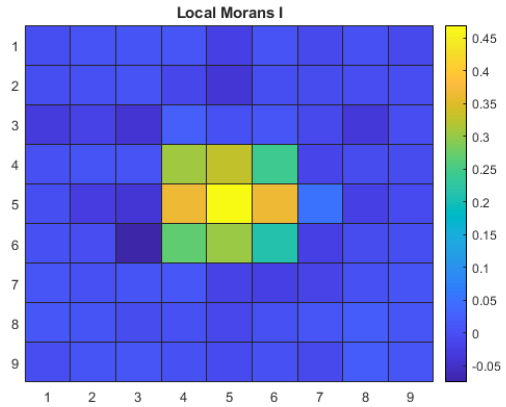

Figure 32: Local Moran's I heatmap in the example proposed

From the figure we can see how the indicator detects positive correlation in the cells belonging to the cluster, which is the desirable result knowing that cells with high and same-sign Z indexes are located close together. The value in the centre of the clustered defect is much higher than those in the border, since that cell is directly surrounded exclusively by similar behaviour cells, while those on the border are close to dissimilar cells (i.e., the in-control ones), which lower their Local Moran's I.

The monitoring ability of mean Z index and Global Moran's I are tested in the example provided. To do so, 2 control charts are built, one for each indicator, by simulating 100 matrices without defects. In this way, we simulate availability of in-control data. The 100 measurements are then used to extract mean and standard deviation of both indicators. Therefore, for each of the two global metrics (here symbolized as m), control limits are computed as:

$$CL = mean(m) \tag{12}$$

$$UCL = CL + K_{CC} \cdot std(m) \quad (13)$$

$$LCL = CL - K_{CC} \cdot std(m) \quad (14)$$

Once the control limits are computed, 5 additional runs are generated, this time with the insertion of a defect analogous to the one explained in the example. The resulting charts for this simulation are reported in Figure 33.

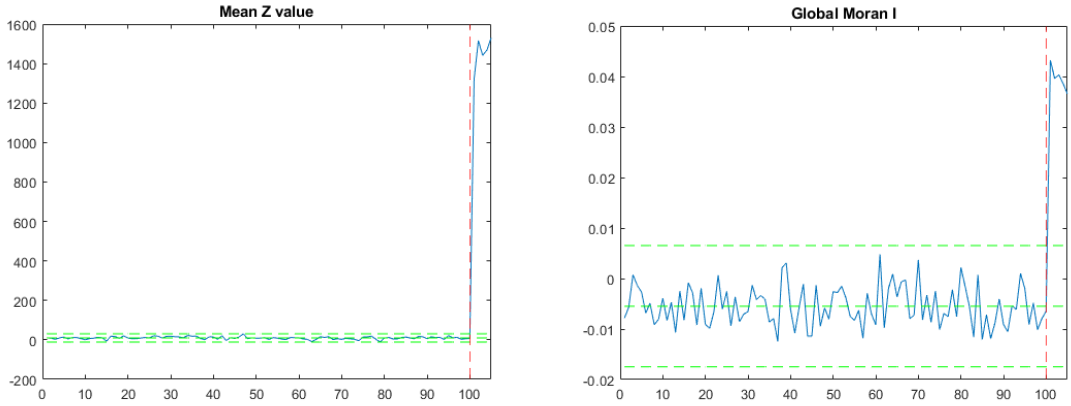

Figure 33: Control Charts for mean Z index and Global Moran's I

Both control charts show a relevant shift after the introduction of the defect, confirming ability of the two metrics to highlight defects like the one simulated.

The last step consists of the automatic identification of cells which contribute to the presence of OOC patterns. In this simulation, the same defective matrix of Figure 31 is analysed through relevance assessment of Local Moran's I. As explained in section 3.1, 1000 randomizations of the Z index matrix are performed, with successive computation of 81x1000 Local Moran's I. All of these are used to extract an ECDF that becomes the basis to assess relevance of the original 81 Local Moran's I values. In the following Image, cells with Local Moran's I beyond 99.5% percentile or below 0.5% percentile are highlighted in red.

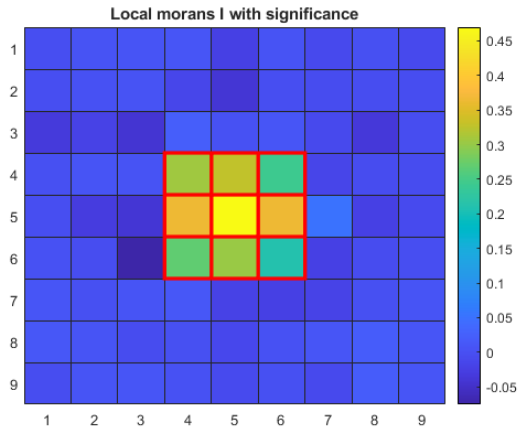

Figure 34: Local Moran's I heatmap with significance assessment

In the simulation study, it is possible to assess how well the method is performing in defect identification, since we know which is the defective region. To that, we can adopt the metrics commonly used in classification algorithms, aimed at describing the algorithm prediction performances. More in details, accuracy, recall and precision are used to compare the diagnosis results [49]. The formulas of the three indicators are hereafter reported:

$$Accuracy = \frac{True\ defect + True\ in\_control}{\#\ elements} \tag{15}$$

$$Recall = \frac{True\ defect}{True\ defect + False\ in\_control} \tag{16}$$

$$Precision = \frac{True\ defect}{True\ defect + False\ defect} \tag{17}$$

In the example above, the value for the 3 indicators is 100%, since we have perfect correspondence between cells identified as defective and real defects.

4.2 Simulation Scenarios

To gain a better understanding of the methodology proposed and to identify its strengths and weaknesses, multiple simulation scenarios are proposed. All the scenarios see the introduction of defects in the 9x9 matrix via alteration of parameter

β_1, with various entity of alteration and number of defective cells. However, each scenario follows a specific rationale. In specific, three cases are simulated:

- *Single cluster*: defective cells are generated in a unique cluster in matrix' centre
- *Sparse defects*: defective cells are randomly located throughout the matrix
- *Two clusters*: defective cells are generated in two cluster, with opposite sign of alteration, but equal intensity

For each scenario, multiple matrices with different characteristics are generated. Each of them is referred to as *experiment*.

4.2.1 Single cluster

Single cluster replicates the study showed in the first example, but it extends the analysis for a wider range of defects magnitude and dimension. More in detail, the defect size D is tested in the range [1, 3, 5, 7], while K is tested in the range [2, 3, 4]. For each experiment (and for each scenario), we provide a visualization of all metrics that make up the methodology, thus CORT component, Area Difference component, Z index and Local Moran's I (with p-value assessment). Together with them, a monitoring application based on mean Z index and Global Moran's I with the 100+5 runs setup is provided. The following image provides a graphical visualization of the 12 proposed experiments.

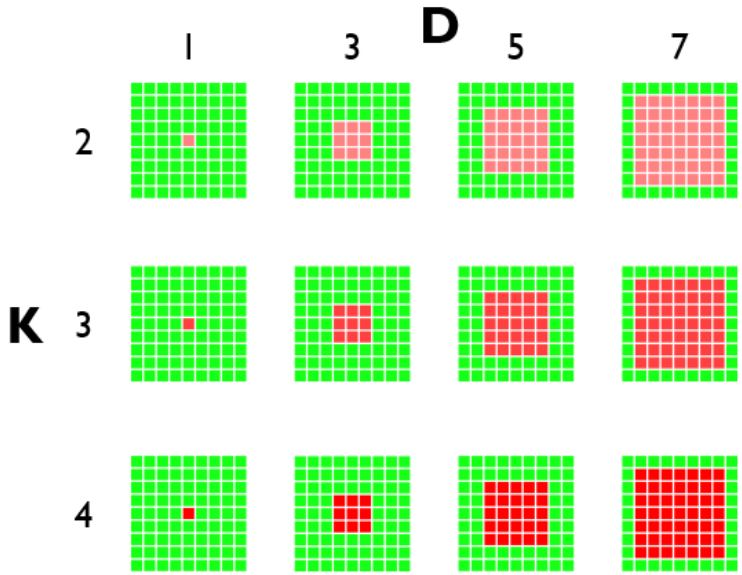

Figure 35: Visualization of *single cluster* experiments

Figure 36 and Figure 37 show the results for CORT and Area difference components. Both components of the Z index provide good highlighting of the defective cells, which assume higher CORT component since they are less correlated with average profile (lower correlation results in higher values thanks to $\varphi(x)$ function), while Area Difference component is higher since slow cooling profiles stay above normal cooling ones, resulting in bigger area under the curve. Both metrics are influenced by intensity K, while only Area Difference component seems to be relevantly affected by defect size, with smaller defects resulting in better highlighting of the defect. This is due to the fact that with bigger defects, the average profile gets "dragged" by defective profiles, resulting in a curve more similar to defective ones than in cases with smaller defects. However, a good separation between in-control and defective is still available for bigger defects. Part of what makes this possible is that with higher average profile, the in-control cells will assume Area Difference values that tend to the negative side, which increases separation between in-control and OOC cells.

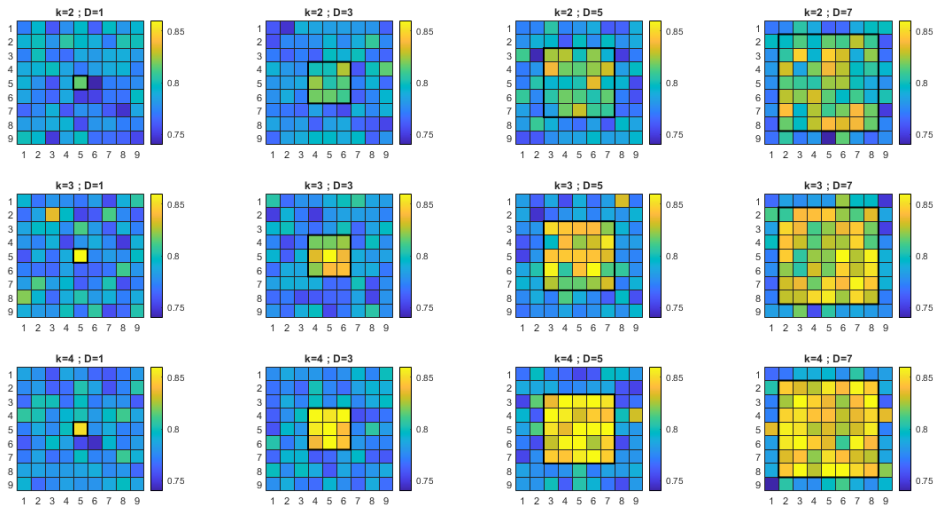

Figure 36: Visualization of CORT component in one example for each *single cluster* experiment

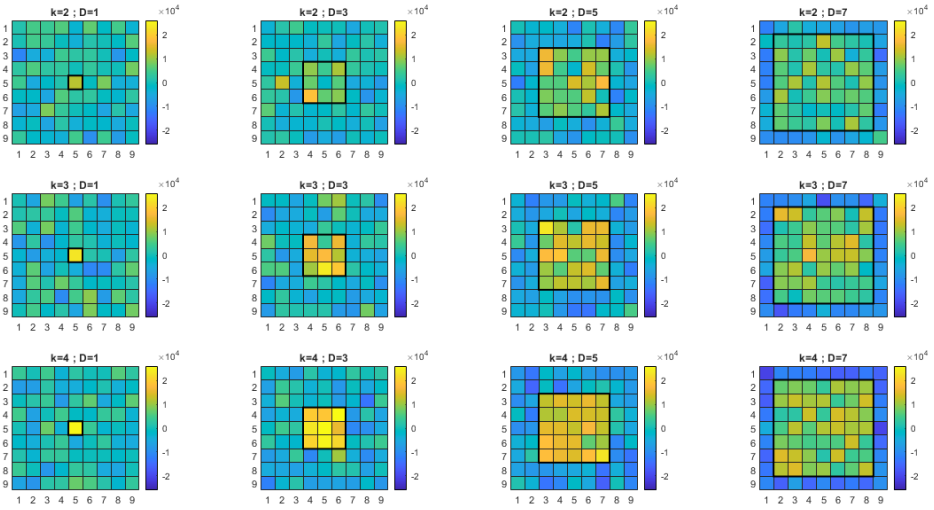

Figure 37: Visualization of Area Difference component in one example for each *single cluster* experiment

As for the Z index, from the 12 heatmaps we can see that the Z index allows the defective regions to stand out well from the in-control cells, independently from the size of the defect, a trivial result considering that it is the combination of two metrics which both highlight defective cells. As expectable, with increasing intensity we can visualize a stronger difference between defective centre and border cells. The results of "dragging" effect that bigger defects apply on average profile is visualizable also for Z index, as for Area Difference component. In fact, we see again that defective cells have lower intensity than with smaller D, and in-control cells assume lower values.

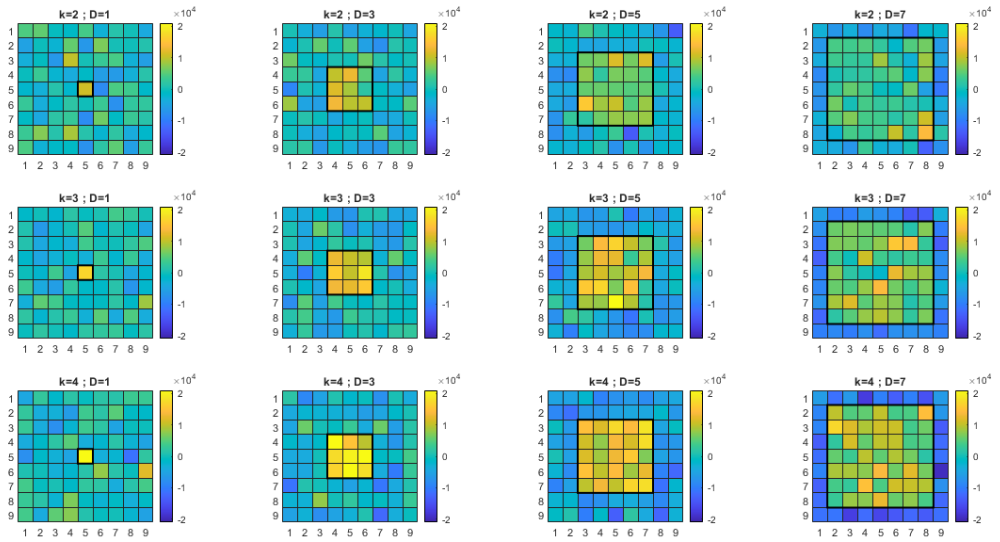

Figure 38: Visualization of Z index in one example for each *single cluster* experiment

The insights from Local Moran's I are quite different from the Z index ones. Single-cell experiments see negative Local Moran's I, which is reasonable since it reflects the case in which a cell is surrounded by cells with different behaviour. While for small and medium defects (D = 3, 5) the defective region still stands out well from the in-control one, when defects become very wide (D = 7) the effects become smoothened. The reason behind this smoothening lies in the behaviour of Z index as D increases. As we have seen, the leverage on average profile applied by higher number of defective cells diminishes the absolute value of Z index for defective cells with respect to experiments with fewer defects, and at the same time increases the absolute value of in-control cells in the negative side. Therefore, when Local Moran's I is computed for cells closer to border, they are impacted by proximity to in-control cells that have Z index value negative and further from 0 than in cases with smaller D. As a consequence, Local Moran's I will be closer to 0.

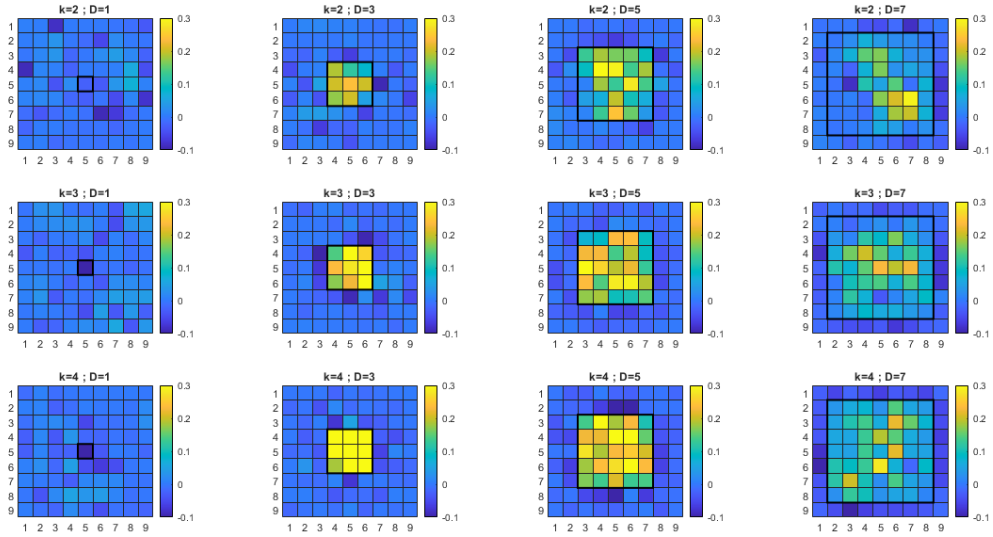

Figure 39: Visualization of Local Moran's I in one example for each *single cluster* experiment

The smoothing effect is evident when we try to exploit Local Moran's I for diagnostic purposes, as shown in Figure 40, since the lower Local Moran's I are less significant. If we consider the information of relevancy obtained through the multiple randomization approach described in the previous section (visualized with the red squares), it is clear that Local Moran's I fails at the identification of defective cells when the altered region corresponds to a high percentage of overall dataset.

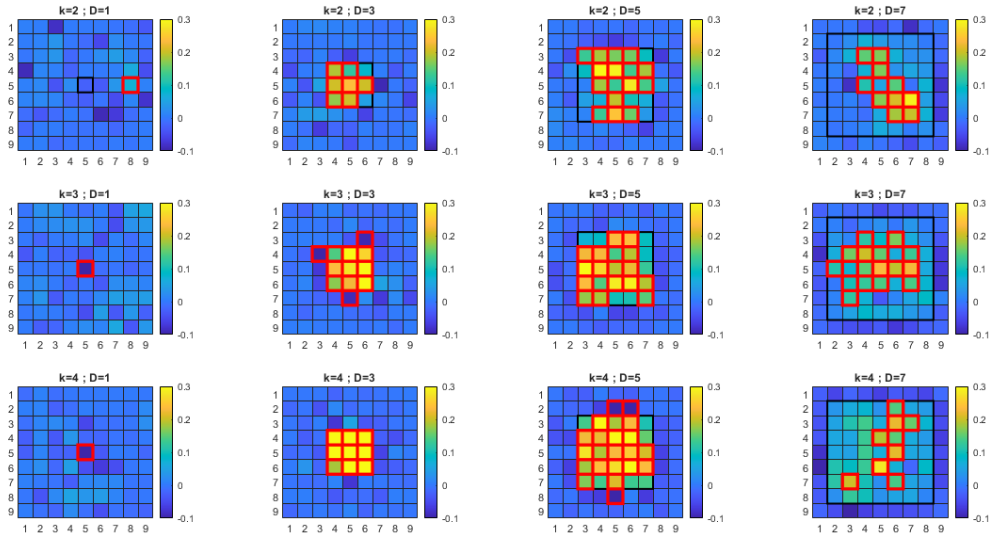

Figure 40: Visualization of Local Moran's I with significance assessment in one example for each *single cluster* experiment

Results for the three classification metrics after 100 repetitions of each experiment are reported in the following table:

	D=1	**D=3**	**D=5**	**D=7**
K=2	Acc = 0.974 Tp = 0.257 Prc = 0.181	Acc = 0.983 Tp = 0.964 Prc = 0.897	Acc = 0.889 Tp = 0.674 Prc = 0.954	Acc = 0.538 Tp = 0.241 Prc = 0.980
K=3	Acc = 0.981 Tp = 0.528 Prc = 0.423	Acc = 0.985 Tp = 0.999 Prc = 0.891	Acc = 0.923 Tp = 0.788 Prc = 0.957	Acc = 0.568 Tp = 0.287 Prc = 0.994
K=4	Acc = 0.987 Tp = 0.714 Prc = 0.527	Acc = 0.976 Tp = 1 Prc = 0.833	Acc = 0.966 Tp = 0.826 Prc = 0.962	Acc = 0.580 Tp = 0.305 Prc = 0.999

Table 3: Accuracy, Recall and Precision after 100 repetitions of each *single cluster* experiment

The intuition about inability to flag as defective cells that are such is confirmed by the measurement of recall for D = 7 with 100 tests for each experiment: the values span

from 24 to 30%. However, the precision results are very good, meaning that though the method is unable to recall all defects, those identified are typically correct. On the contrary, with small defects (D = 3) we observe very high recall, but a lower precision, due to the tendency to estimate as defective in-control cells on the border, which assume highly negative Local Moran's I values due to their proximity to neighbours with intensely different Z values. Overall, D is far more influent than K, since it leads to completely different trends, while increases in K given a D just impact positively the three metrics.

Moving to monitoring, mean Z index works well for the identification of defects like the one simulated, since defective runs are associated to values whose difference from the control limits flattens their visualization to a single line. The higher intensity K and size D, the more intense is the shift in the control chart as soon as the defective runs begin. Global Moran's I works really well for the identification of defective regions (D>1), since defective runs have significantly different values than in-control runs, which results in a shift in the control chart. This shift becomes more intense with increasing K, as expectable. In presence of a unique defective cells, which assumes negative Local Moran's I value, Global Moran's I is unable to detect it, no matter the intensity.

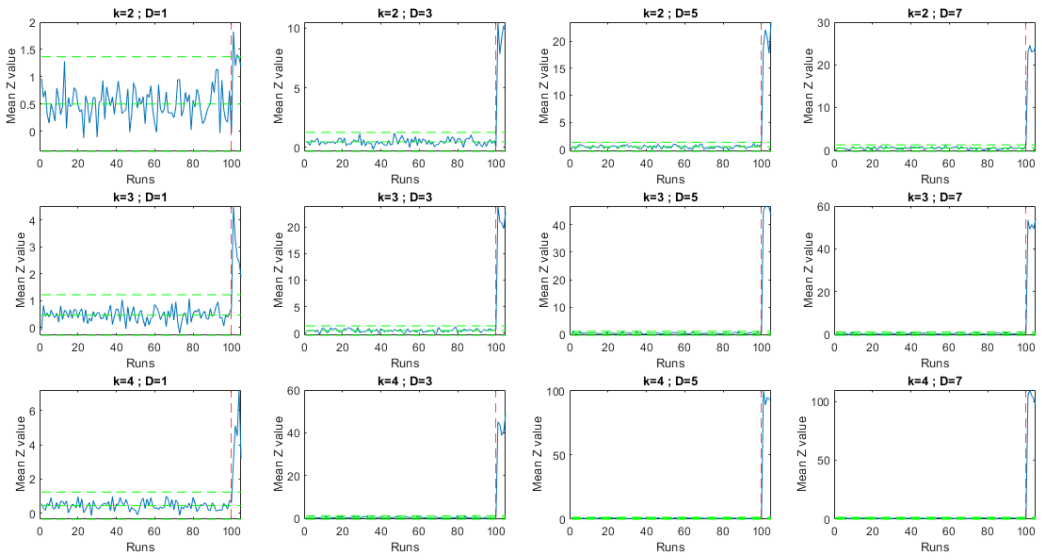

Figure 41: Visualization of CC on mean Z index for each *single cluster* experiment

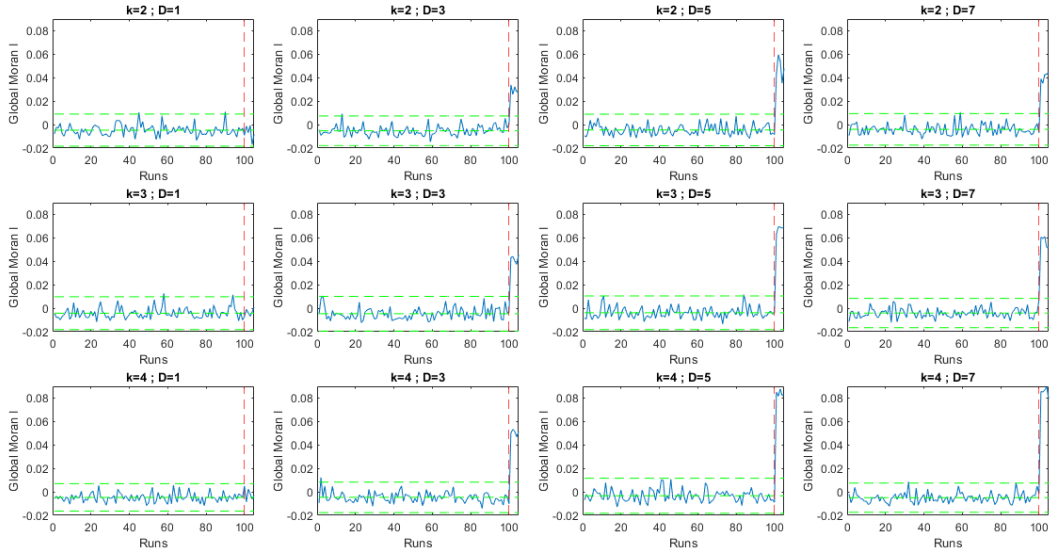

Figure 42: Visualization of CC on Global Moran's I for each *single cluster* experiment

4.2.2 Sparse defects

In this scenario the two parameters used to characterize each experiment are magnitude of alteration K (always positive) and number of defects N. In specific, N is tested in the range [1, 9, 25, 49], to keep ties with the previous experiment, while k is tested in the range [2, 3, 4]. The following image provides a graphical visualization of the 12 proposed experiments.

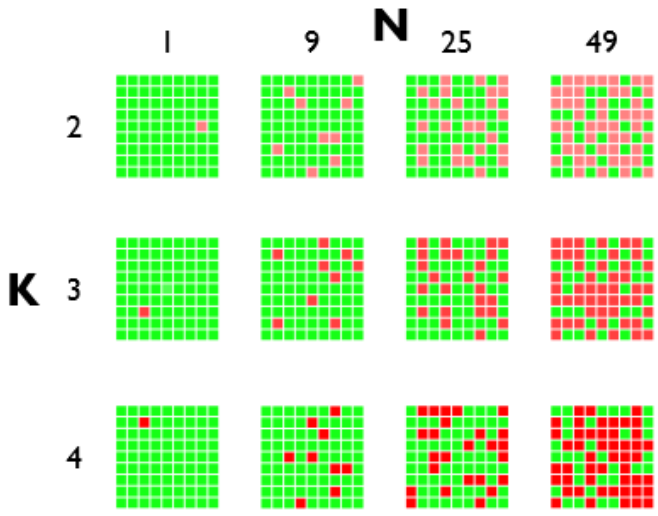

Figure 43: Visualization of *sparse defects* experiments

The two components of Z index in *sparse defects* scenario behave exactly as in *single cluster* one, since the two metrics consider no information of spatial distribution; therefore, given the same number of defective cells and the same intensity K, the two scenarios are indistinguishable from the point of view of the two indicators.

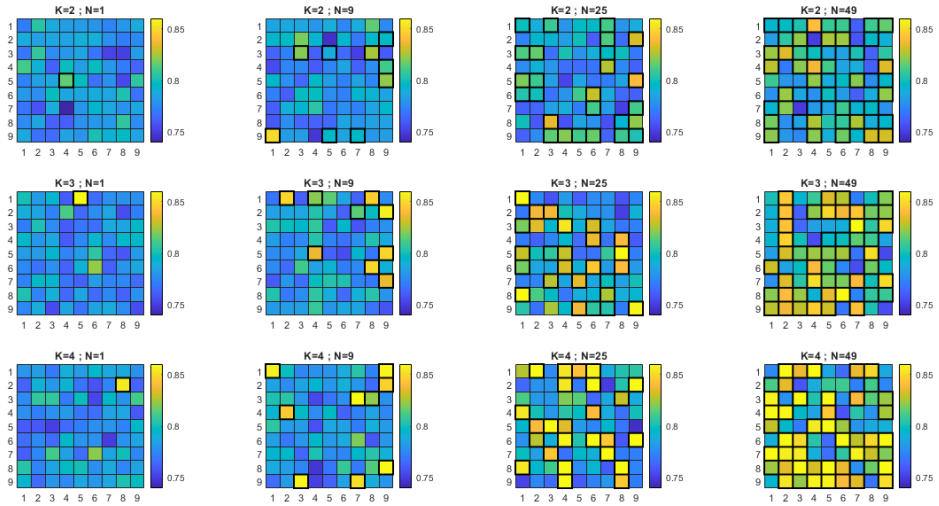

Figure 44: Visualization of CORT component in one example for each *sparse defects* experiment

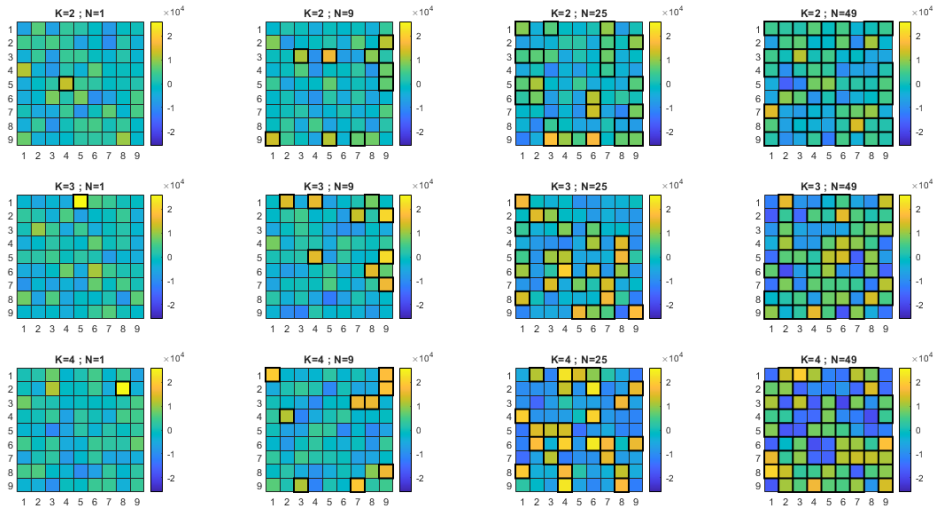

Figure 45: Visualization of Area Difference component in one example for each *sparse defects* experiment

Of course, the same consideration holds true for Z index, which as in the previous scenario, allows defective cells (highlighted with thicker border) to stand out well from in-control ones.

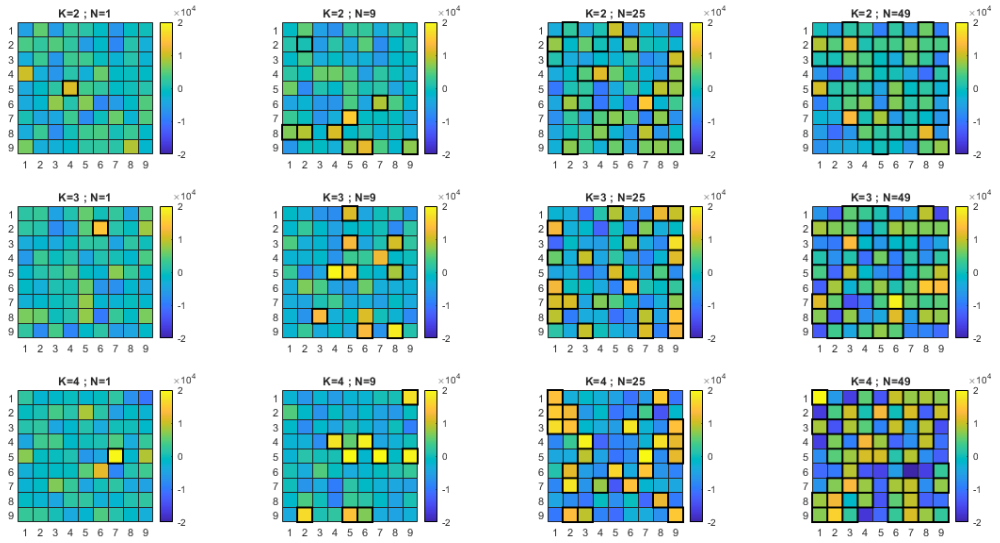

Figure 46: Visualization of Z index in one example for each *sparse defects* experiment

On the other hand, the behaviour of Local Moran's I is completely changed with respect to *single cluster* scenario, since the spatial arrangement of Z indexes is now random. As a result of randomness in the arrangement, some positive correlation areas and negative correlation cells are present in the dataset, but it is impossible to link Moran's I values to presence of defects.

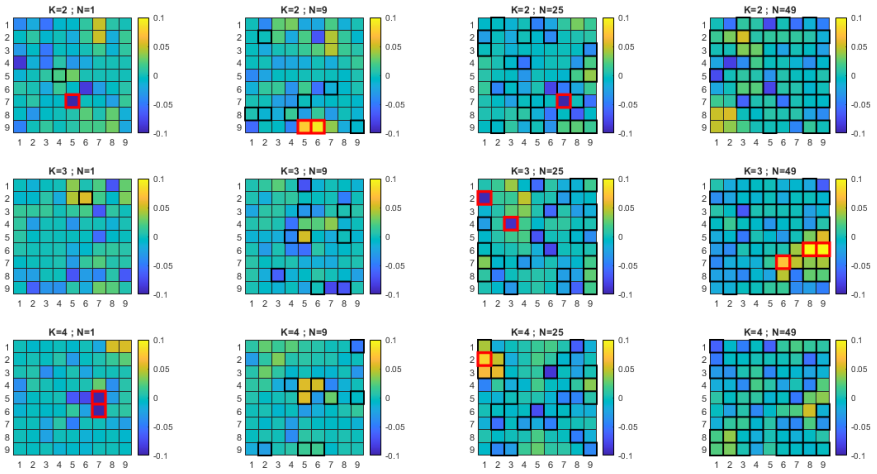

Figure 47: Visualization of Local Moran's I with significance assessment in one example for each *sparse defects* experiment

The evaluation metrics are computed repeating each experiment 100 times.

	N=1	N=9	**N=25**	**N=49**
K=2	Acc = 0.968 Tp = 0.080 Prc = 0.034	Acc = 0.875 Tp = 0.024 Prc = 0.103	Acc = 0.684 Tp = 0.015 Prc = 0.201	Acc = 0.397 Tp = 0.020 Prc = 0.294
K=3	Acc = 0.971 Tp = 0.040 Prc = 0.040	Acc = 0.876 Tp = 0.029 Prc = 0.119	Acc = 0.686 Tp = 0.030 Prc = 0.226	Acc = 0.403 Tp = 0.022 Prc = 0.425
K=4	Acc = 0.971 Tp = 0.120 Prc = 0.120	Acc = 0.876 Tp = 0.024 Prc = 0.122	Acc = 0.690 Tp = 0.018 Prc = 0.220	Acc = 0.402 Tp = 0.019 Prc = 0.372

Table 4: Accuracy, Recall and Precision after 100 repetitions of each *sparse defects* experiment

As for accuracy, we can see that in each experiment it tends to coincide with the percentage of in-control cells over the total. This is because the method tends to find no significant Local Moran's I values, a behaviour perfectly expressed by the recall values, that usually lay around 2% for experiments with more than one defective cells. Parameter N seems to have no effect on precision and recall, and at the same time we don't see improvements as K increases, given a N. Overall, we can conclude that this

diagnostic approach is not suitable for scenarios in which there is no spatial association between Z indexes.

Moving to monitoring, for mean Z index, we see exactly the same behaviour as in the single cluster scenario, which is reasonable if we consider that the Z index values will be very similar if generated with same alteration K and same number of defective cells. As for Global Moran's I, in this scenario it is not a good metric to detect presence of defects, since for most of the experiments there never is an alarm once the defective runs begin. The exceptions are the cases with many defective cells and with high deviation K. In these conditions, clusters randomly form in the matrix, creating spikes of Local Moran's I which are then captured by the mean value.

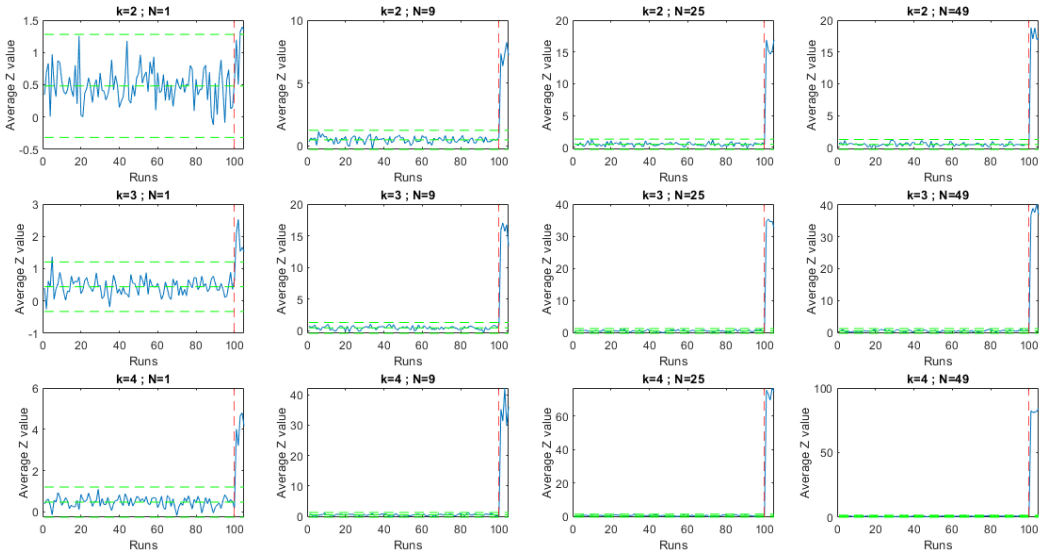

Figure 48: Visualization of CC on mean Z index for each *sparse defects* experiment

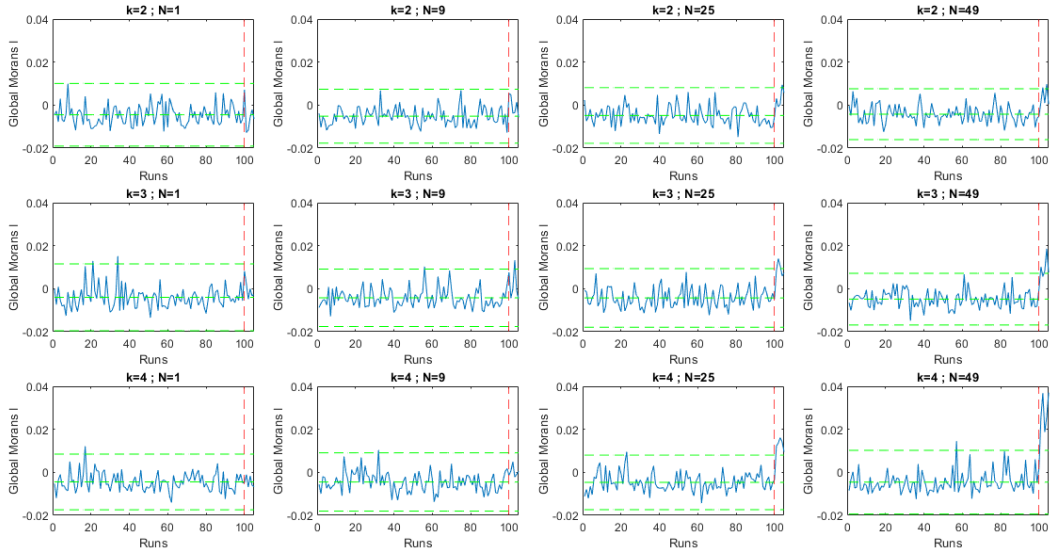

Figure 49: Visualization of CC on Global Moran's I for each *sparse defects* experiment

4.2.3 Two clusters

The last scenario is characterized by presence of two clusters, which are generated with same number of cells and same alteration intensity, though opposite in sign. Each experiment is characterized by number of defective cells N, which includes cells from both clusters, thus being equal to the double of the number of defective cells of each, and the alteration intensity K, which is once positive and once negative. In specific, N is tested in the range [2, 18, 36, 54], while K is tested in the range [±2, ±3, ±4]. The following image provides a graphical visualization of the 12 proposed experiments.

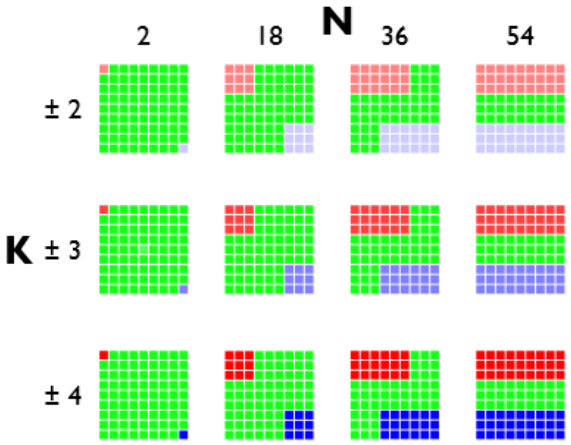

Figure 50: Visualization of *two clusters* experiments

CORT component highlights with high values both defective regions, indicating for both lack of correlation with the average profile. Area difference component shows a division between hot, average and cold behaviour (respectively positive K defects, in-control and negative K defects). Differently from the previous scenarios, the Area Difference component does not provide lower values for defective cells when their number increase, since the presence of two balanced defective clusters cancels the "drag" effect on average profile, which stays closer to the average between in-control profiles. Therefore, the indicator is affected only by intensity K, and not by N.

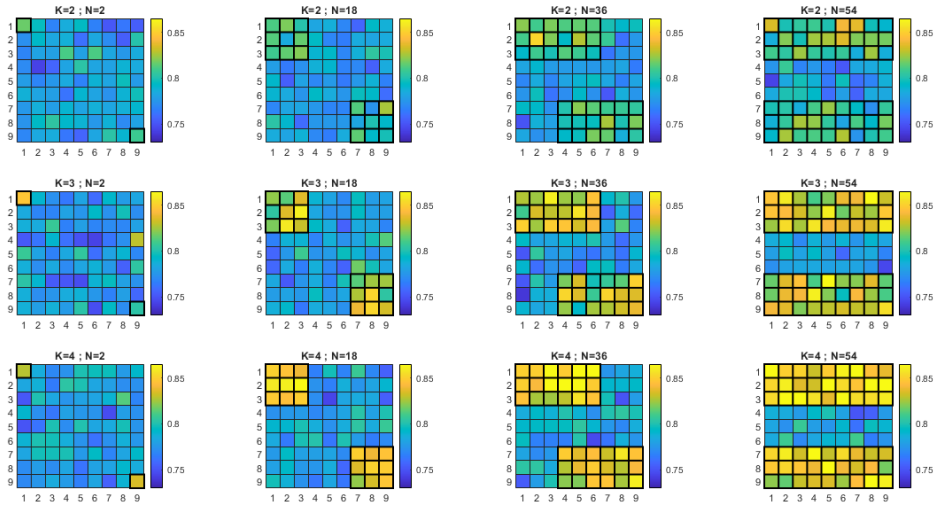

Figure 51: Visualization of CORT component in one example for each *two clusters* experiment

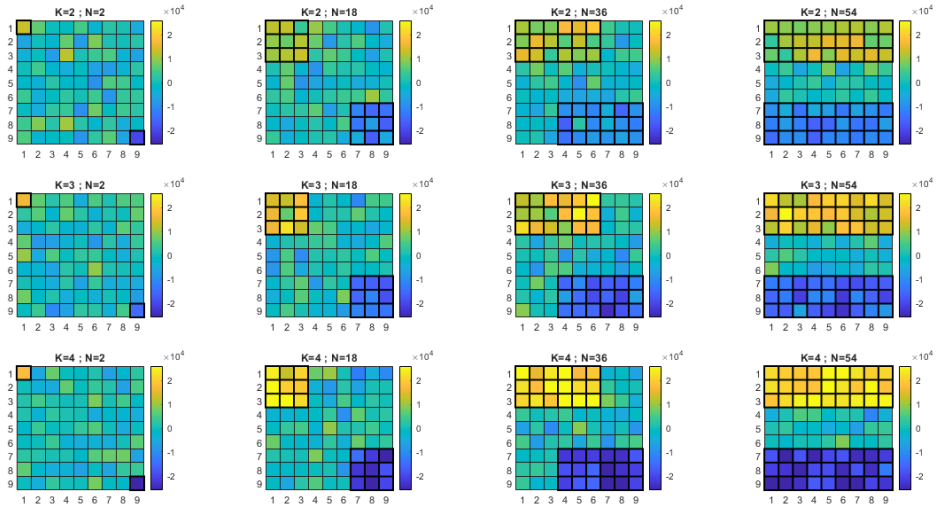

Figure 52: Visualization of Area Difference component in one example for each *two clusters* experiment

Once the two components are combined, for Z index we see good ability to capture defective cells. The sign is the same as Area Difference component, while CORT component acts as magnifier, increasing separation with in-control cells, which assume values closer to 0.

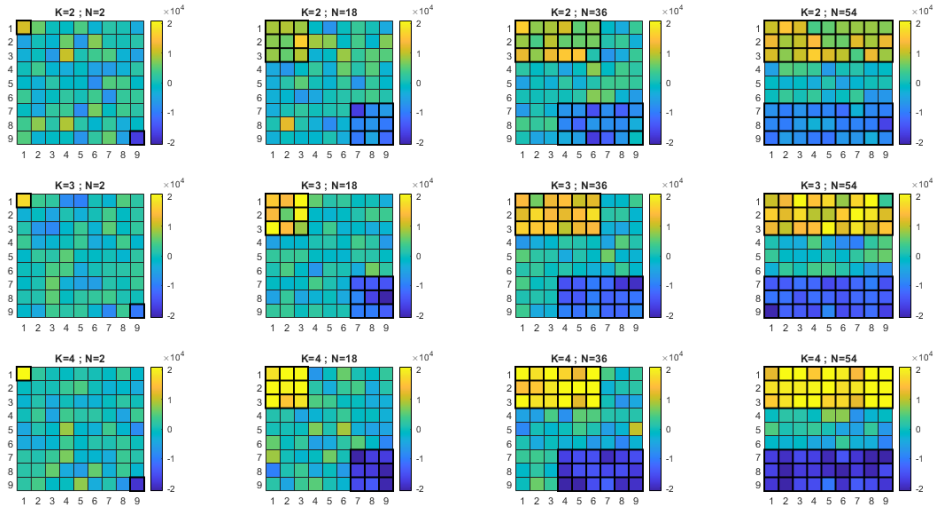

Figure 53: Visualization of Z index in one example for each *two clusters* experiment

Local Moran's I becomes very effective for the identification of defective cells when there are many, leading to good ability to recall defective cells, with some occasional false positives around the border of clusters.

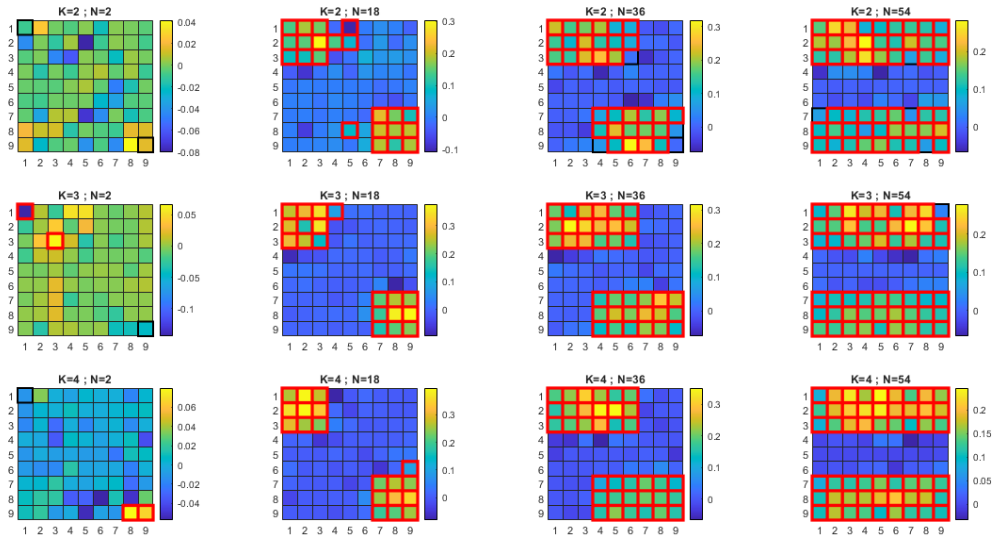

Figure 54: Visualization of Local Moran's I with significance assessment in one example for each *two clusters* experiment

If we look at the three classification metrics, we see as for other scenarios poor performance with single cell defects, but very good performances for all others, with lower recall when N increases, due to the more frequent cluster formation during randomization, which as in the first scenario increases the threshold for relevancy of Local Moran's I.

	N=2	N=18	N=36	N=54
K=2	Acc = 0.965 Tp = 0.130 Prc = 0.118	Acc = 0.970 Tp = 0.954 Prc = 0.917	Acc = 0.949 Tp = 0.898 Prc = 0.986	Acc = 0.880 Tp = 0.820 Prc = 0.999
K=3	Acc = 0.970 Tp = 0.230 Prc = 0.258	Acc = 0.991 Tp = 0.982 Prc = 0.979	Acc = 0.957 Tp = 0.904 Prc = 0.999	Acc = 0.870 Tp = 0.805 Prc = 1
K=4	Acc = 0.974 Tp = 0.270 Prc = 0.312	Acc = 0.996 Tp = 0.983 Prc = 0.998	Acc = 0.914 Tp = 0.807 Prc = 1	Acc = 0.769 Tp = 0.654 Prc = 1

Table 5: Accuracy, Recall and Precision after 100 repetitions of each *two clusters* experiment

Moving to monitoring, mean Z index proves to be ineffective in the identification of defective runs, leading to many in-control values throughout different experiments, while defects are in fact present. Some runs do trigger alarms, usually with positive outliers for mean Z, especially when N increases. This is linked to the Area difference component, which for profiles like the ones simulated tends to result in slightly higher values when the alteration of β_1 is positive, given the same K. Therefore, when N increases, positive Z index defective cells act as leverage on the mean value. Instead, Global Moran's I prove to be very effective in the identification of defective runs when multiple cells are involved, with a pattern very similar to the single cluster scenario. However, it lacks effectiveness for single cell defects.

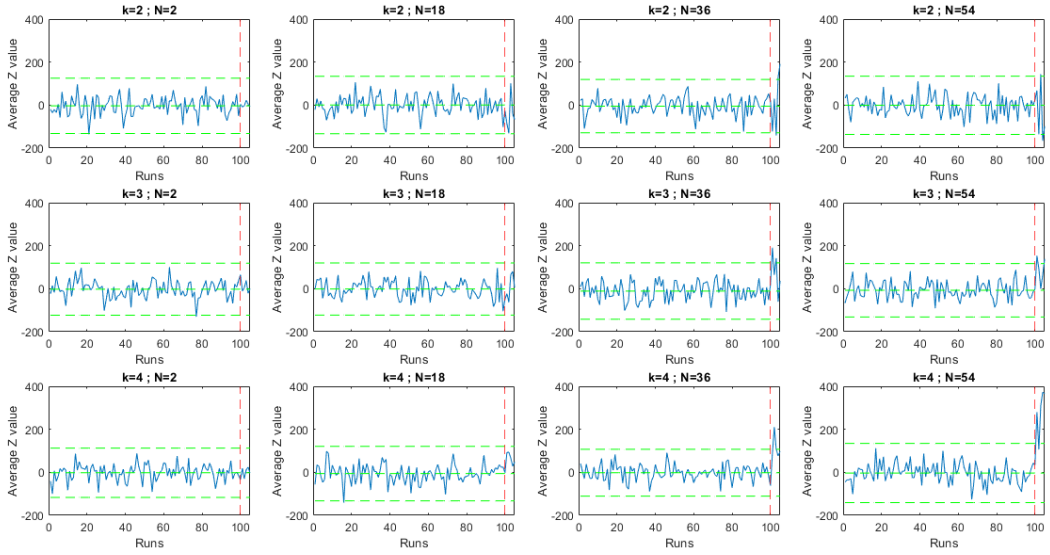

Figure 55: Visualization of CC on mean Z index for each *two clusters* experiment

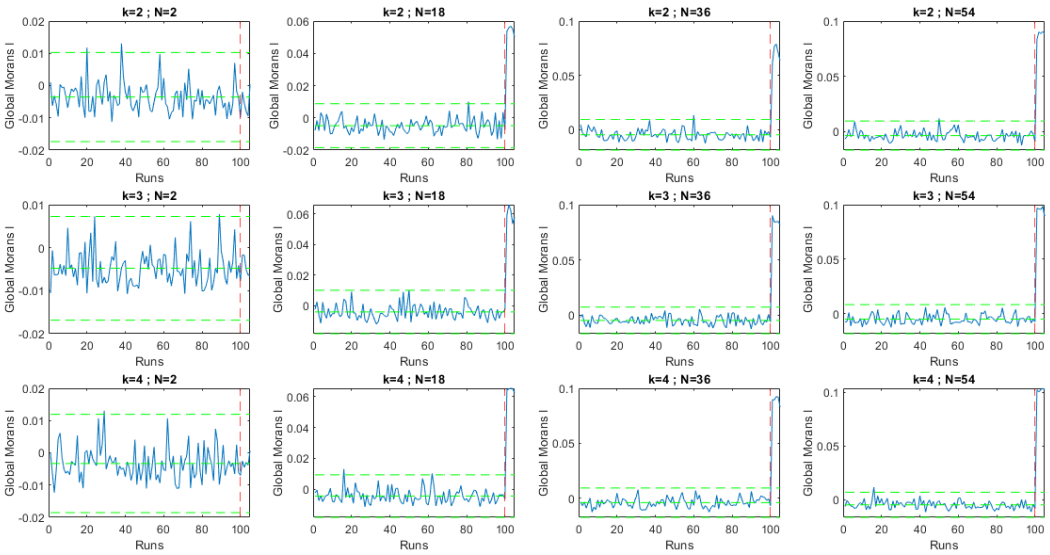

Figure 56: Visualization of CC on Global Moran's I for each *two clusters* experiment

4.3 Improved diagnostics

While for monitoring we discussed that an application that exploits both Global Moran's I and mean Z index is effective in the identification of OOC layers, the diagnostic approach based on Local Moran's I significance level has limited

effectiveness in two situations, i.e., when no association patterns are present and when number of defective cells is high. The former case coincides with the scenario in which defective cells are positioned randomly. The ineffectiveness of Local Moran's I in this scenario is reasonable, since the indicator is built to capture presence of spatial association, and in random configurations like *sparse defects* scenario none is present. In the latter case, the performance of the method is hindered by the smoothing effect of Local Moran's I observed for large defects, which doesn't allow to capture well all the cells that contribute to the pattern detected in control charts.

Local Moran's I is a powerful tool to understand what happens in a process, allowing to know how cells interact with their neighbours. However, if the purpose it to subdivide cells according to their behaviour into in-control and OOC, then the weaknesses of the indicator identified in the previous paragraph do not allow it to be used as a diagnostic tool in all process conditions. Instead, we want to exploit a metric that allows to classify elements effectively in all scenarios.

As a substitute for the exploitation of relevancy of Local Moran's I, it is reasonable to exploit directly Z indexes for the diagnostics step. Indeed, as shown, in Figure 38, Figure 46 and Figure 53, this indicator always highlights defective cells, regardless the defect typology. In addition, we substitute the diagnosis approach based on ECDF estimation with a hierarchical clustering algorithm, which is less sensible to defect dimensions, and which is able to identify more than one defect cluster (for example, the two clusters scenario). The new diagnosis methodology and the results are displaced in the following paragraph.

4.3.1 Hierarchical clustering

Agglomerative hierarchical clustering is a clustering technique which progressively joins the two closest elements of the dataset – basing on a predefined distance metric – until all elements are joined. The algorithm consists of 4 steps:

1) As initialization phase, each observation constitutes a cluster, and the distance between cluster coincides with distance between observations
2) The two clusters with minimum distance between them are merged in a new cluster, and their original distance is recorded
3) The distance between the new cluster and the pre-existing ones is computed

4) If all observations are included in a cluster the method stops. Otherwise, it is repeated from step 2

The output of the algorithm is a dendrogram, a chart shaped as a tree in which the distance between two elements is visualized through the height of the bracket connecting them. Dendrograms can be truncated ad a desired height to obtain a desired number of clusters. A visualization of how agglomerative hierarchical clustering works is provided in the following image.

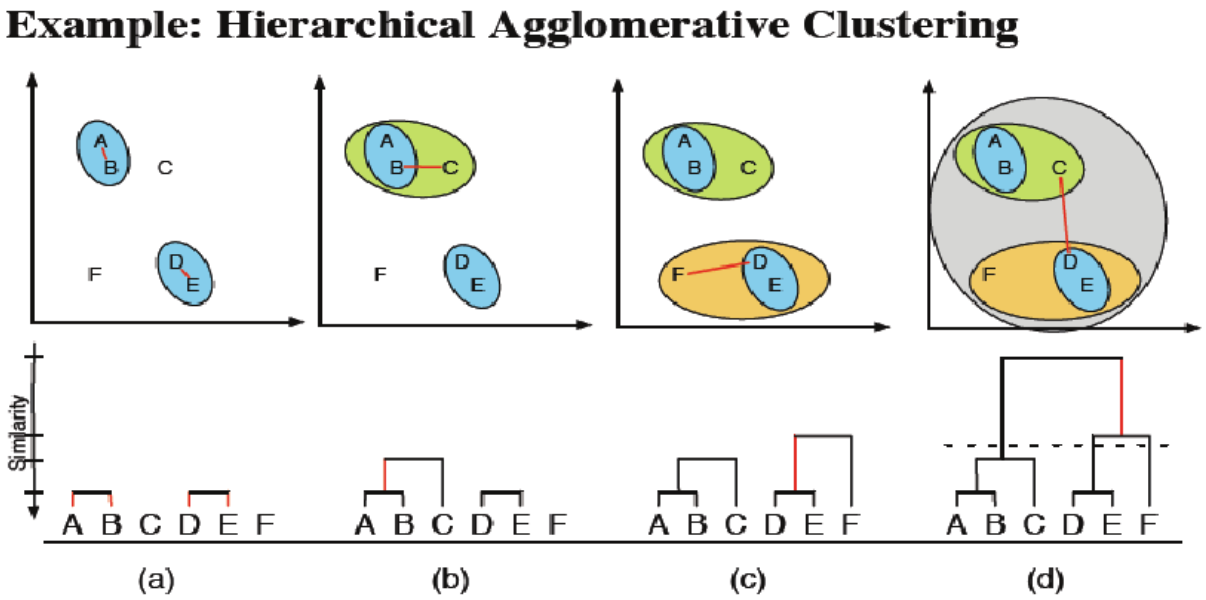

Figure 57: Example of Agglomerative hierarchical clustering [50]; as distance between clusters, the minimum distance between all couples of elements belonging to the two clusters is taken; the length of vertical lines in dendrogram reflects distance between clusters

In the methodology proposed, a hierarchical clustering algorithm can be applied directly to Z indexes. The distance between elements is the absolute value of the difference between their values. Once the dendrogram with all observation is built, a number of clusters is selected. Each cluster corresponds to a class of thermal behaviour. The rationale that makes this approach interesting for diagnostics is that clusters with centroid closer to 0 will be composed of elements with temperature profile similar to average one, and therefore less critical. On the other hand, clusters with centroid far from 0 will be composed of elements with thermal behaviour far from average, and therefore critical. Thus, through hierarchical clustering, we are able to

automatically identify groups of cells with critical temperature evolution. In the following sub-sections, the implementation of hierarchical clustering for diagnostic purposes is tested in the three defective scenarios.

4.3.2 Single cluster

The simulation experiments of section 4.2 are replicated with 100 repetitions to assess how good hierarchical clustering is at identifying defective cells. The number of clusters is set to two, knowing that two classes of behaviour are expected for the experiment: in-control cells and slow-cooling OOC cells. By slicing the dendrogram at the height in which only two partitions are present, a classification of each observation in one of the two clusters is achieved. In specific, the cluster with lower centroid (and closer to 0) is "*in-control*", the one with higher centroid is "*OOC*".

A visualization of the performance of hierarchical clustering with two cluster is provided with the following figure. The heatmaps for each experiment are drafted by counting how many times over the 100 trials each cell is assigned to the top cluster, and a colormap from 0 to 100 is created to show visually this frequency of assignment.

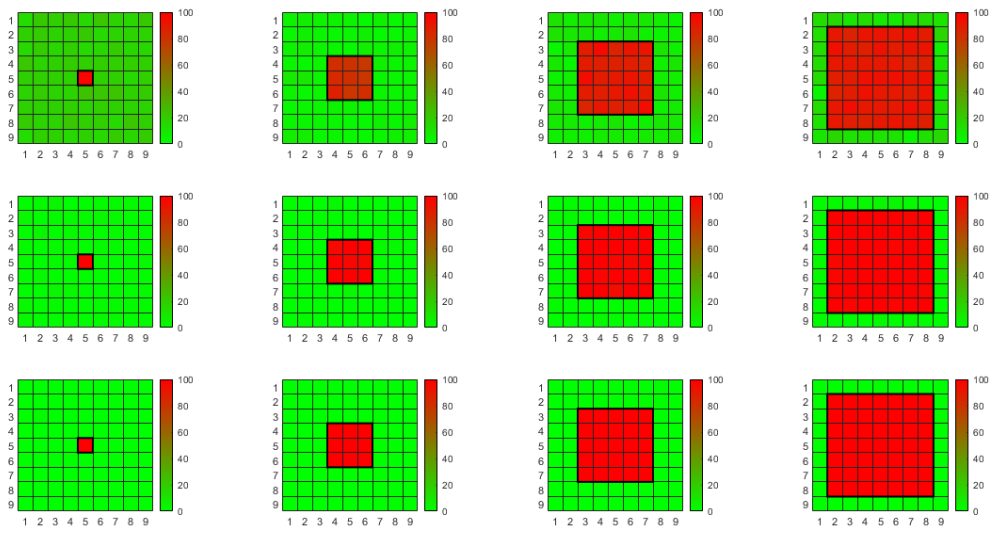

Figure 58: Outcome of hierarchical clustering over 100 runs for *single cluster* scenario

The evaluation of the three classification metrics is also provided, with highlighting through bold text of the metrics that see an improvement with respect to the results of diagnostics based on relevance of Local Moran's I:

	D=1	D=3	D=5	D=7
K=2	Acc = 0.819 **Tp = 0.98** **Prc = 0.444**	Acc = 0.939 Tp = 0.814 Prc = 0.850	**Acc = 0.916** **Tp = 0.898** Prc = 0.891	**Acc = 0.898** **Tp = 0.906** **Prc = 0.980**
K=3	**Acc = 0.983** **Tp = 1** **Prc = 0.825**	**Acc = 0.994** Tp = 0.983 **Prc = 0.967**	**Acc = 0.992** **Tp = 0.989** **Prc = 0.987**	**Acc = 0.990** **Tp = 0.994** Prc = 0.991
K=4	**Acc = 0.999** **Tp = 1** **Prc = 0.982**	**Acc = 0.999** Tp = 0.998 **Prc = 0.998**	**Acc = 0.999** **Tp = 0.999** **Prc = 0.998**	**Acc = 0.998** **Tp = 0.999** Prc = 0.999

Table 6: Accuracy, Recall and Precision after 100 repetitions of each *single cluster* experiment with hierarchical clustering approach

For the majority of experiments, we have an improvement of at least two out of three metrics, and in particular we see very relevant improvements for recall of D = 7 and D = 1, the experiments where Local Moran's I performed worse. Overall, K plays an important role in the performance of the method, with better results when K is higher. Instead, D has almost no influence, and the three evaluation metrics have very similar results independently of defect size, with the only exception of low K single cell experiment. The only experiment in which no improvements are achieved is (K=2 D=3), however the values are still very similar to the previous approach. Considering that this is the only worsening case, and the big benefits achieved when D=1 and D=7, the hierarchical clustering approach is better than assessment of relevancy of Local Moran's I for *single cluster* scenario.

4.3.3 Sparse defects

As done in single cluster scenario, after the extraction of the dendrogram, the number of clusters is set to two, with the bottom one linked to in-control and the top one linked to OOC. From the algorithm point of view, this scenario is indistinguishable from the previous, since clustering is applied on Z index, which yields no spatial information, thus having defective cells arranged in a cluster or randomly doesn't impact the

hierarchical clustering if their number and intensity are kept constant. A table with the resulting metrics values is reported, this time highlighting improvements with respect to Local Moran's I in the corresponding scenario:

	N=1	N=9	N=25	N=49
K=2	Acc = 0.785 **Tp = 0.990** **Prc = 0.472**	**Acc = 0.934** **Tp = 0.836** **Prc = 0.806**	**Acc = 0.913** **Tp = 0.880** **Prc = 0.892**	**Acc = 0.890** **Tp = 0.897** **Prc = 0.973**
K=3	Acc = 0.964 **Tp = 1** **Prc = 0.891**	**Acc = 0.994** **Tp = 0.971** **Prc = 0.975**	**Acc = 0.993** **Tp = 0.993** **Prc = 0.986**	**Acc = 0.984** **Tp = 0.990** **Prc = 0.993**
K=4	**Acc = 0.999** **Tp = 1** **Prc = 0.967**	**Acc = 0.999** **Tp = 0.999** **Prc = 0.996**	**Acc = 0.999** **Tp = 0.998** **Prc = 0.999**	**Acc = 0.998** **Tp = 0.999** **Prc = 0.999**

Table 7: Accuracy, Recall and Precision after 100 repetitions of each *sparse defects* experiment with hierarchical clustering approach

As we can see, the results of the table are nearly identical to the previous one, with differences that are entirely linked to variability during simulation. In this scenario improvements thanks to the implementation of hierarchical clustering with respect to Local Moran's I significance are huge, and they are especially remarkable for recall and precision, which previously spanned respectively in the range [2%, 12%] and [4%, 42%]. Besides, for N>1 accuracy is much higher than in the previous case, when it tended to coincide with percentage of in-control cells over the total. The only worsening is for accuracy in concurrence with N=1, however the better values in the previous case are induced by lack of identification of defects, which in an imbalanced dataset made almost entirely of in-control results in high accuracy. Overall, the approach based on clustering of elements according to their Z index is able to counter the weakness of Local Moran's I assessment in cases with randomly distributed defects.

4.3.4 Two clusters

Differently from the previous examples, in this scenario 3 clusters are expected: a high Z one, a low Z one and an average Z one. Cells are therefore assigned to low Z cluster (-1), middle Z cluster (0) or high Z cluster (+1). By summing the assigned cluster

number over 100 runs, it is possible to draft a visualization of assignment of cells to the 3 clusters.

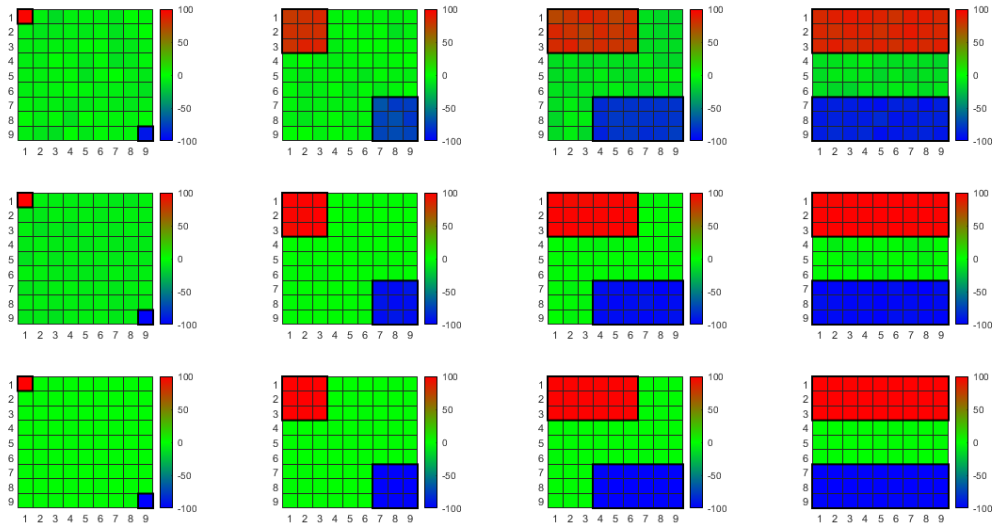

Figure 59: Outcome of hierarchical clustering over 100 runs for *two clusters* scenario

Similarly to *single cluster* scenario, we see that K plays an important role in the performance of the clustering, while number of cells looks less relevant. Results in terms of the three metrics, computed considering as defect the cells assigned to either the top or the bottom cluster, are reported in the following table:

	N=1	N=9	N=25	N=49
K=2	Acc = 0.807 **Tp = 0.945** **Prc = 0.332**	Acc = 0.870 Tp = 0.778 Prc = 0.776	Acc = 0.806 Tp = 0.810 Prc = 0.807	Acc = 0.843 **Tp = 0.875** Prc = 0.892
K=3	Acc = 0.905 **Tp = 0.995** **Prc = 0.644**	Acc = 0.978 Tp = 0.962 Prc = 0.949	**Acc = 0.969** **Tp = 0.968** Prc = 0.969	**Acc = 0.974** **Tp = 0.981** Prc = 0.981
K=4	**Acc = 0.987** **Tp = 1** **Prc = 0.924**	Acc = 0.995 **Tp = 0.997** Prc = 0.984	**Acc = 0.989** **Tp = 0.992** Prc = 0.989	**Acc = 0.994** **Tp = 0.997** Prc = 0.996

Table 8: Accuracy, Recall and Precision after 100 repetitions of each *two clusters* experiment with hierarchical clustering approach

Looking at the metrics, we see that K plays again a big role when it comes to performance, while N is less impactful, with similar values independently from defect size, given the same K. When compared to Local Moran's I significance method, in this scenario we see improvements in ability to identify defects for single cell clusters and for high intensity ones, though with small losses in terms of performance for low K defects. As a trend, we see improvements in recall with reduced precision, meaning that it is able to capture more defective cells, though this also provokes an increase in false positives. Out of the three scenarios, it is the one that sees the least improvements with respect to Local Moran's I significance. However, metrics that don't see an improvement are still very close to the values of the other approach in the same scenario, and overall performances are very satisfactory.

Taking this in consideration, together with the big improvements in the weak points of Local Moran's I significance, we can conclude that the method based on hierarchical clustering is better than the previous one for the identification of cells with critical behaviour.

5. Real-Data Application

5.1 Dataset Explanation

The dataset exploited for the real case study consists of the thermographic monitoring of a Big Area Additive manufacturing (BAAM) build, manufactured by the large-scale printer developed at the Oak Ridge National laboratories in collaboration with Cincinnati Incorporated. Acrylonitrile Butadiene Styrene (ABS) with 20% of chopped carbon fibres weight is used to print a connected serpentine pattern, shown in Figure 60.

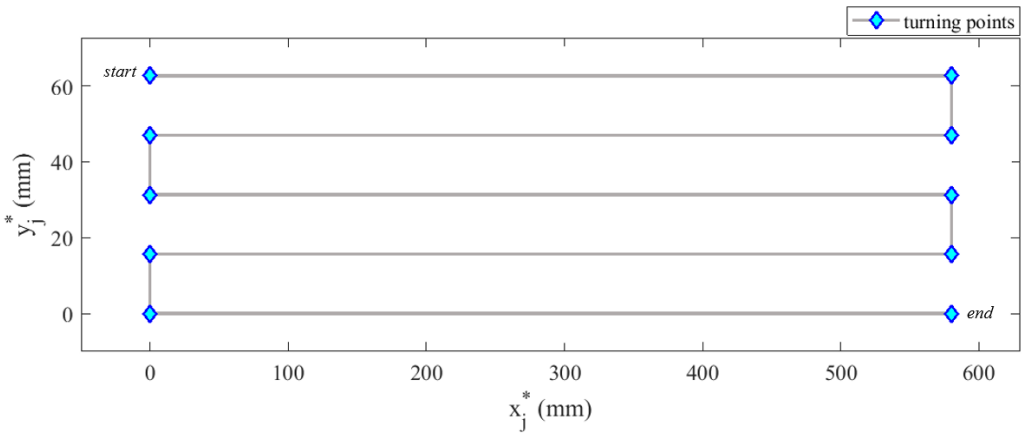

Figure 60: Extruder nominal toolpath

Extruder temperature was set at 230°C, while the building platform was pre-heated at 90°C. Extruder speed was 63.5 mm/s, so that a single layer printing lasts around 70 seconds.

Figure 61: BAAM equipment [51]

During the entire building process, IR videos were acquired using a FLIR A35 thermal camera (FLIR® Systems Inc, Wilsonville, U.S.), positioned near the build area (approximately 1.3 m from the target object) with an inclination of around 45°with respect to the building platform. The camera was equipped with a 25 mm optic, previously calibrated in a temperature range between 25°C and 300°C, with an accuracy of 5°C. During the printing process, the video was acquired with a frequency of 30 fps. Temperature data were exported using ExaminIR software (FLIR® Systems Inc, Wilsonville, U.S.), and then analysed by means of Matlab (MathWorks Inc.).

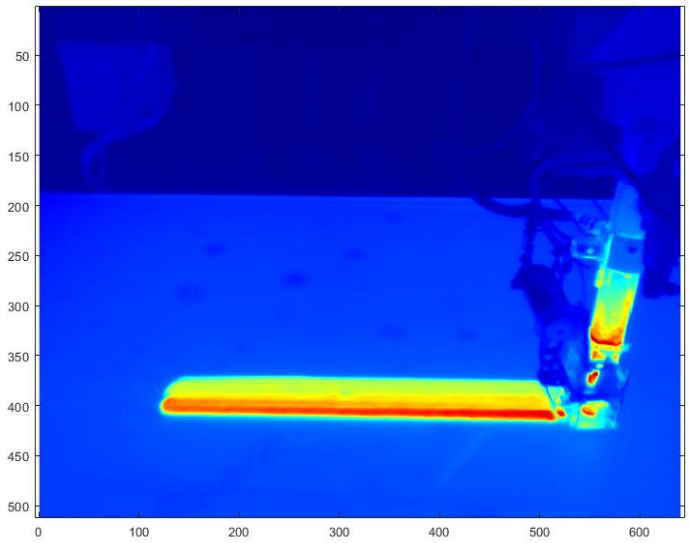

Figure 62: Example frame from IR dataset

5.2 Data Extraction and Pre-Processing

In order to extract temperature profiles from IR videos, few preliminary passages are required. They are mainly meant to place within the video frames a set of regions of interest, extract thermal profiles, and filter out the temperature alteration given by extruder blocking. The following scheme sums up all the needed data pre-processing operations.

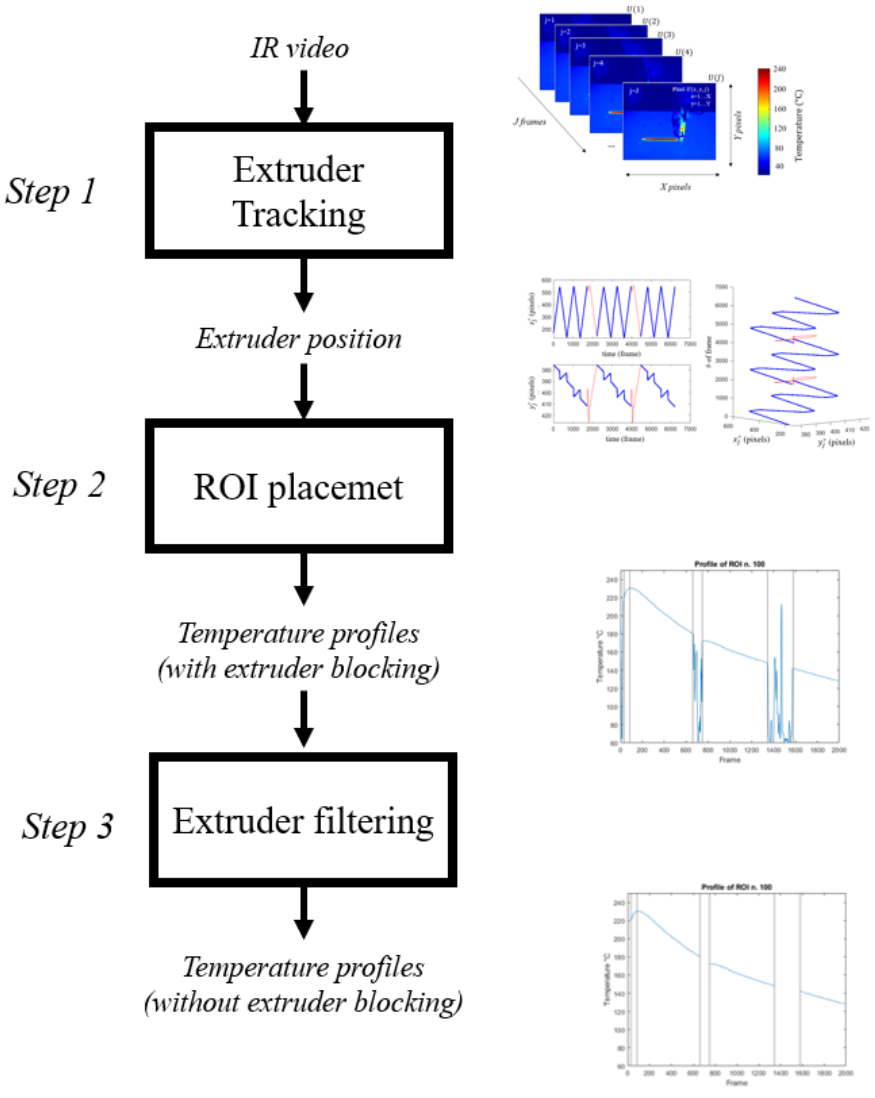

Figure 63: Workflow of pre-processing operations

Step 1. Before the extraction of thermal profiles, it is necessary to obtain information about position of extruder in each frame, since it serves as reference to know which

region of the serpentine is being printed. To obtain this information, visual tracking is adopted as explained in Caltanisseta et al. (2021) [48]. The overall principle of visual tracking consists of identifying and locating one or more target objects in consecutive video frames in a scene composed of different static and dynamic elements. To define the target objects, we exploit corner points, i.e., locations where sudden jumps in the grayscale intensity occur in all directions. We selected the extruder nozzle as the target object, since we are interested in reconstructing its trajectory. The extruder corner points are automatically detected by means of the Harris and Stephens' approach [52], which is based on identifying the corner points by looking at the biggest local variations in image. An example of frame including the extruder nozzle and the detected corner points is shown in the following figure.

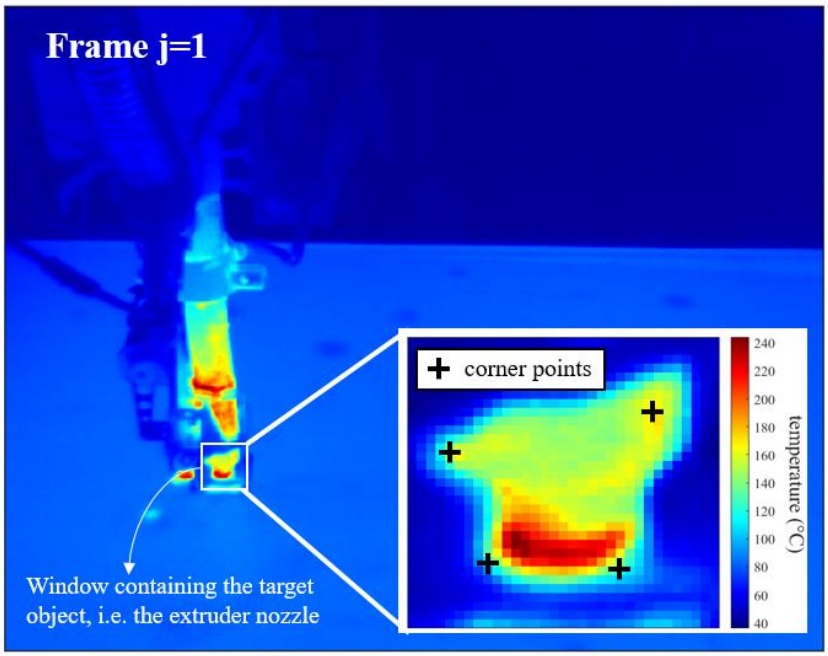

Figure 64: The first video frame together with the detail of the nozzle and its corner points detected by means of Harris and Stephens approach [48]

Once the corner points have been identified in the first frame, the Kanade-Lucas-Tomasi (KLT) algorithm is used to track these points along the entire video duration. The KLT allows to track one or more target objects between temporally consecutive frames, assuming constant object brightness and small displacement. The application of this algorithm enabled the reconstruction of extruder toolpath and the identification

of extruder's nozzle position frame by frame. The extruder position will be used to place a set of regions of interest within each video frame.

Step 2. Once the extruder's toolpath has been identified, extruder position is exploited to place a grid of ROI over each frame, as displayed in Figure 65. Each grid cell, whose centre corresponds to the nozzle tip position in a given frame, is a square with sides long 4 pixels (i.e., the average beads height). As a result of grid creation, a total of 506 Regions of Interest (ROI) are created and analysed. ROIs are enumerated from 1 to 506 following the toolpath. To draft a comparison with the simulation described in the previous sections, these ROIs correspond to the cells of the simulated matrices. Each bead contains approximately 100 ROIs. Turning points are made of 4 each.
Temperature profiles are extracted for each of the 506 ROIs and for each layer. All the thermal profiles will be extracted starting from the moment when the extruder releases the molten material onto the considered ROI. The automatic identification of said point is the result of the application of the algorithm explained in Appendix A. All the temperature profiles will be extracted with the same duration (2000 frames).

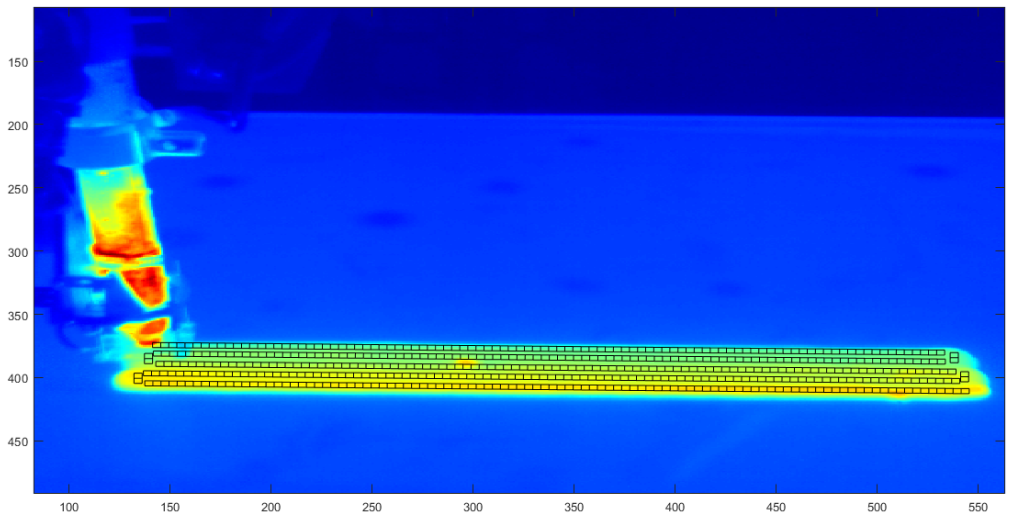

Figure 65: Visualization of grid over serpentine

Step 3. The main issue with the extracted profiles is the presence of highly noisy regions. These phenomena occur when the extruder passes in front of a ROI, covering it for the camera, which in turn provokes acquisition of temperature measurements of the print head, rather than of the extruded material. In the following image, a

visualization of noisy regions in temperature profiles is provided by plotting the raw temperature profiles from four different locations. For each ROI, noisy regions are in different temporal position, because of the different relative position between extruder and ROI.

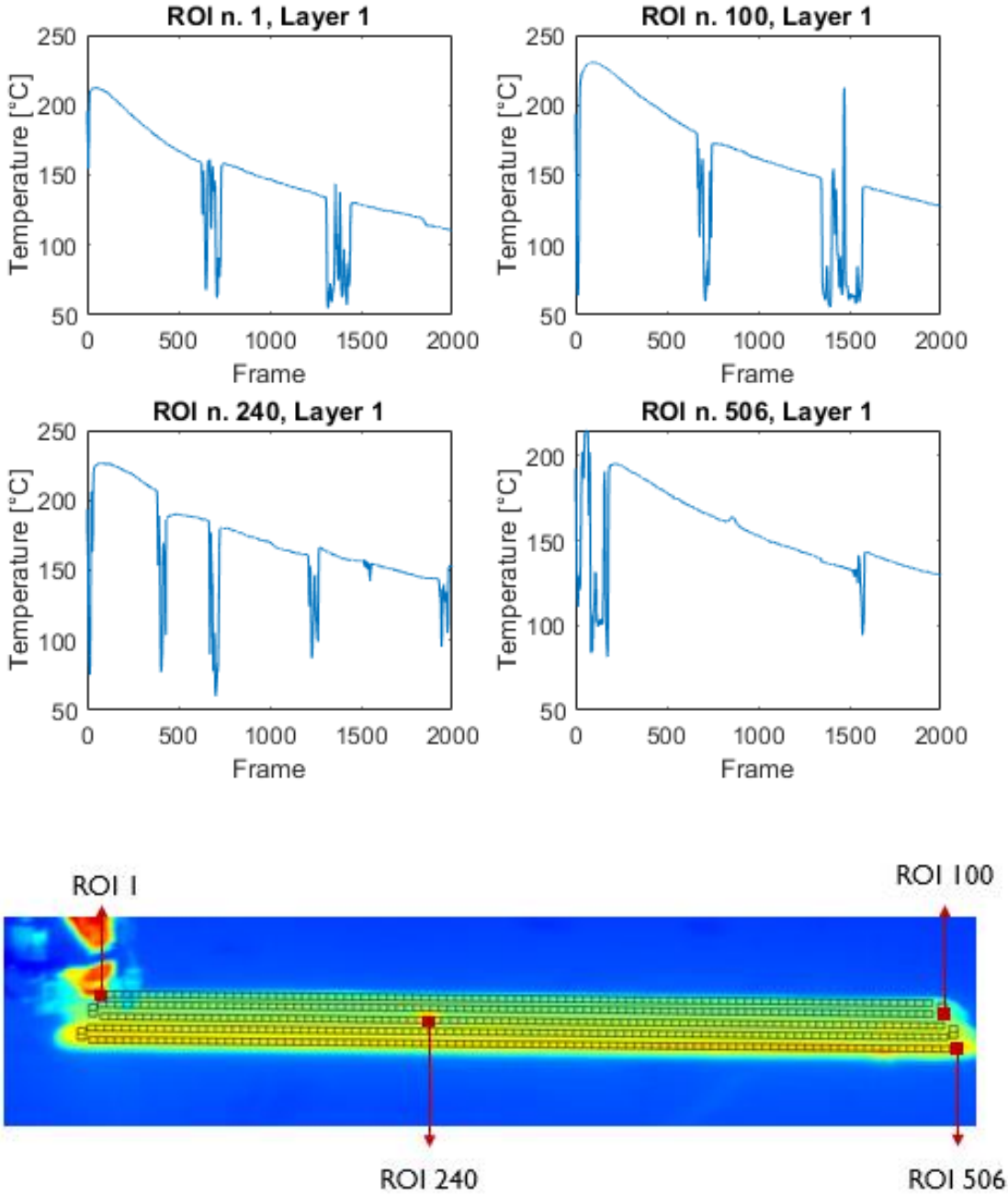

Figure 66: Raw temperature profiles of four different ROIs, with reference to their location on the grid

Knowing that noisy regions are characterized by higher variability than correct data acquisition regions, we want to use this property to automatically recognize them and successively filter them out. For this purpose, we applied a method for time series segmentation, based on the paper from Killick et al. (2012) [53] (Appendix A), which is meant to divide time series in a pre-defined number of regions according to some specific property. In this case, after time series detrending through computation of successive differences, we applied this algorithm to search regions with homogeneous variability. Once this is done, the temperature values inside of those regions are substituted by the linear interpolation between the extremes of the noisy regions. Since noisy regions at the beginning of the acquisition cannot be properly interpolated, given that only one extreme is available, the first 200 frames are excluded for each temperature profile. Once processing is finished, 506x15 (ROIs x Layers) temperature profiles are generated. At this point, data are separated according to layers, and each layer is treated independently from others.

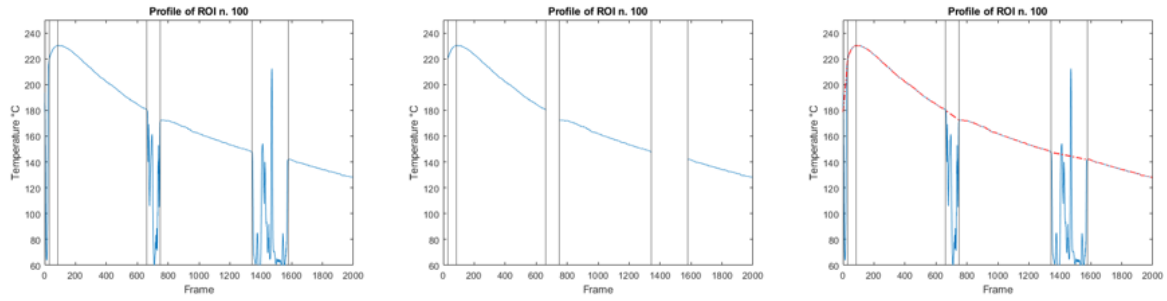

Figure 67: Filtering of noisy regions for ROI 100 at layer 1; from left to right we have: change points identification, noisy regions removal, interpolated profile (red) over raw one (blue)

5.3 Thermal phenomena description and analysis through Z and Moran's I

5.3.1 Analysis of Z index and Local Moran's I

Figure 68 and Figure 69 displays a visualization of the Z index evolution throughout the 15 layers. More in details, the first image depicts the average Z value for each ROI, while the second one displays the temporal evolution within each layer and among

consecutive layers. From these figures, we can see that some relevant patterns are present. First, we noticed a peculiar behaviour of temperature in the first bead, thus from ROI 1 to 100. First of all, for all layers after the first, we see that the first 12 ROI resulted to be way colder than the average temperature profile. Considering that these ROIs are at the beginning of the layer, this pattern may be due to delays in material release. Indeed, extruder acceleration or deceleration may lead to material release flaws, such as over/under-extrusion states, particularly if feed rate is not correctly synchronized with nozzle speed [19]. Therefore, it is reasonable to assume that the cold start of bead 1 is caused by under-extrusion linked to initial acceleration. These values are separated from the rest of the bead by an evident jump in Z index, which is placed in each layer at the same temporal instant. After the jump, we see for the rest of bead 1 a progressively decreasing trend for Z index until the turning point, with some jumps always synchronized in the same locations. A similar behaviour, though less remarkable, is present in the last bead, thus in the last 100 ROIs. This jumping pattern is most likely linked to fluctuations of the extrusion feed rate caused by the extruder deceleration before the layer's end, as already discussed. Independently from the cause of the different behaviours, these inhomogeneities in the thermal evolution of all layers may cause the generation of defects and poor mechanical performances, as observed in the paper from Malekipour et al. (2018) [41].

A noticeable pattern linked to the layer progression is the increasing disparity between beads 1 and 5 and beads from 2 to 4. From Figure 69, we can notice that in bead 1, the Z indexes get lower values with layer progression, while beads 2 and 4 see an increase in Z index value. This phenomenon may be linked to stronger heat retention for inner beads with respect to external ones, which creates more and more disparity in thermal evolution as layers progress. The overall presence of heat retention phenomenon throughout the print can be observed in Figure 70, where the average profile for each layer is depicted. If we combine the two insights, we see that in a print that overall is affected by heat retention, beads 2 and 4 are more affected by it than the average, presenting an increase in Z index. However, this interpretation does not apply for bead 3, the central one, whose Z values appear stable along the process. On the other hand, we see an opposite pattern for bead 1, with Z indexes that become more polarized towards negative values as layers progress, hinting at a lower heat retention for this bead with respect to the average.

Finally, we can see that bead 3 presents in the middle a localized temperature behaviour inhomogeneity in most layers, as well as the turning point between bead 2 and 3. The former behaviour is caused by presence of a hot spot, which from a video analysis is found to be caused by a reheating of that region every time the nozzle hovers above it to move from ROI 506 to ROI 1 to start a new layer. The latter is caused by the combination of colder temperature evolution of border and proximity to the very cold region at the beginning of bead 1.

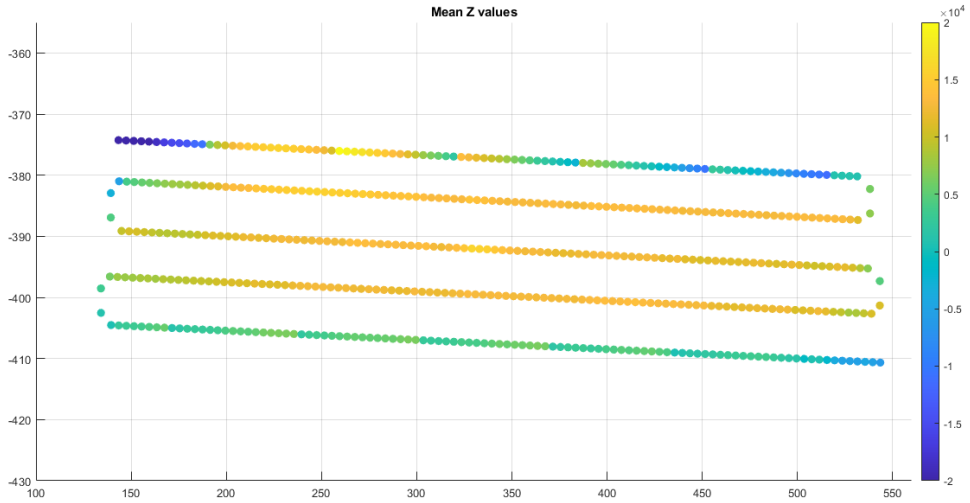

Figure 68: Scatterplot of all ROIs with colormap used to visualize mean Z index; this visualization is analogous to the heatmaps seen in Simulation section

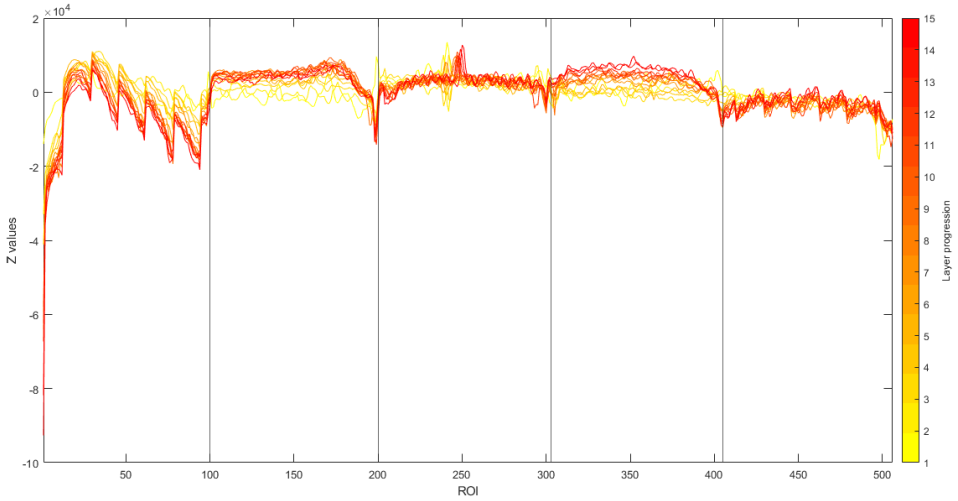

Figure 69: Z index by ROI for each of the 15 layers; vertical lines are used to mark turning points between beads, while colormap is used to visualize layer progression; since ROI sequence follows extruder path, these profiles show temporal evolution for Z index for a layer along its printing

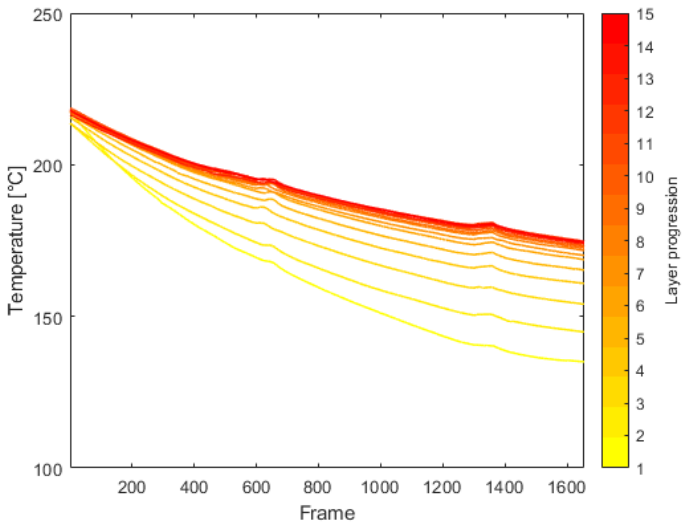

Figure 70: Plot of all average profiles, with colormap used to visualize layer progression

The Z values extracted are then used as input to compute Local Moran's I for each ROI, using the inverse of the Euclidian distance between each couple of ROIs as weight matrix. As for Z indexes, a visualization of the average Local Moran's I of each ROI

and of the progression of the indicator values throughout the print are provided in Figure 71 and Figure 72.

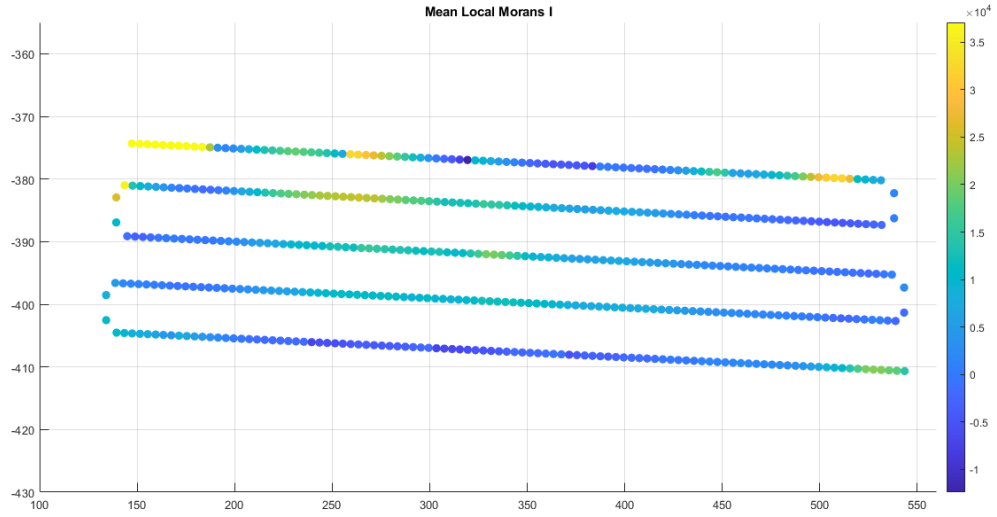

Figure 71: Mean Local Moran's I of each ROI

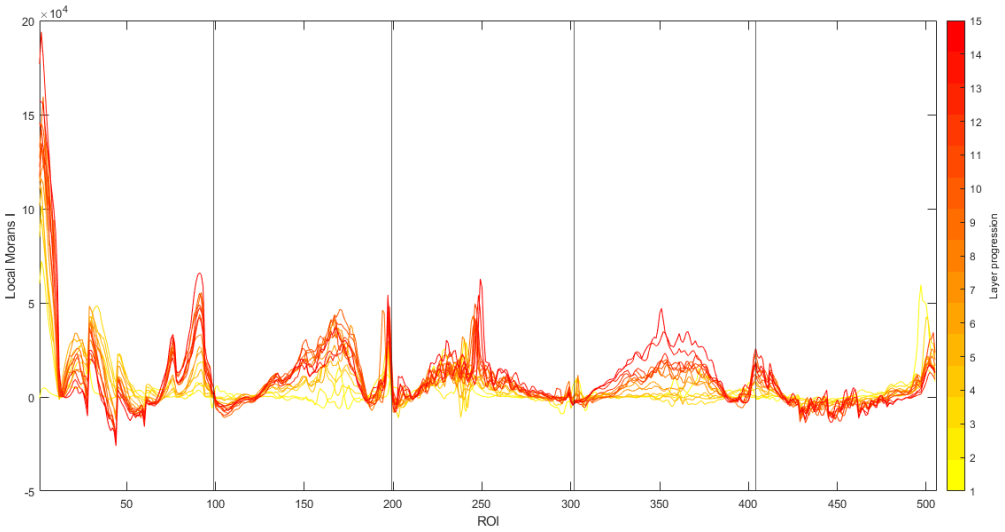

Figure 72: Local Moran's I by ROI for each of the 15 layers

Generally speaking, Local Moran's I shows a very variable and instable behaviour along the process, highlighting different areas of high spatial association and discontinuities.

In the first bead, the indicator shows a higher variability with respect to the other ones. This is caused by the presence of different and separated areas with homogeneous temperature, but with a thermal behaviour far from the average thermal profile. Local Moran's I also shows many negative jumps due to the sudden changes of Z index, which imply negative spatial correlation between neighbour ROIs. The same phenomena are also present in the last bead, due to the same pattern but with smaller intensity, due to the less intense Z indexes of the bead.

Beads 2 and 4 show a more regular pattern, with increasing association of values towards the centre of the bead as layers progress, reflecting the increase in Z index observed in advance.

Local Moran's index is also able to capture well the presence of a local thermal anomaly of bead 3, which can be seen with the spike in the corresponding location. This flaw is clearly visible in all layers except 6 and 7. Figure 73 displays the temperature anomaly in layer 9.

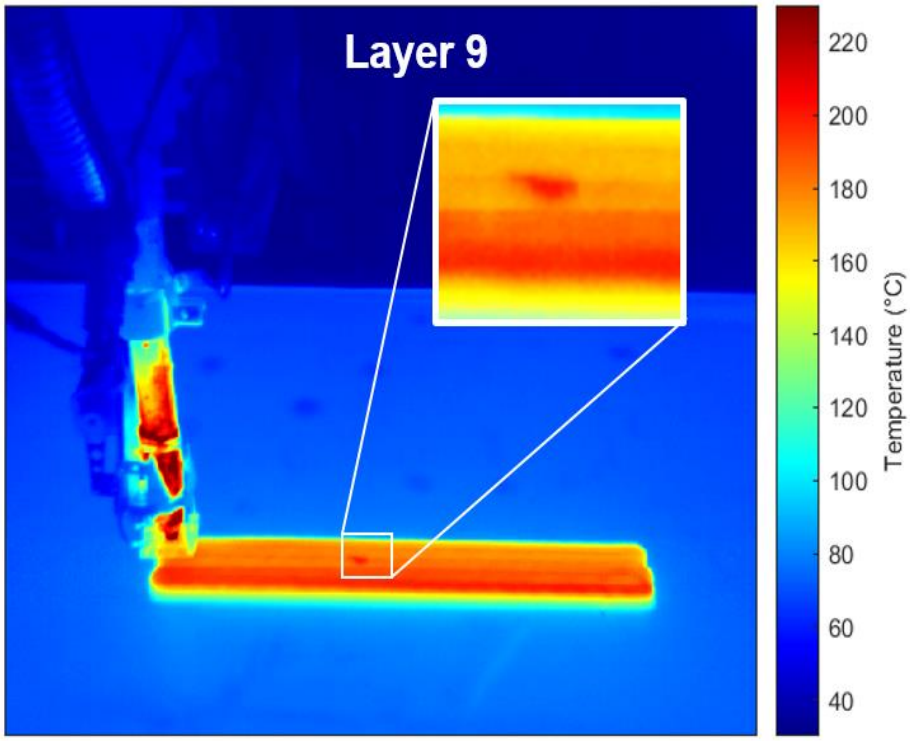

Figure 73: Frame that shows presence of hot spot in the middle of bead 3 after the completion of layer 9

5.3.2 Mean Z index and Global Moran's Index analysis

Looking at mean Z index for each layer, it is possible to observe a positive trend for the indicator. After the first three layers, where the mean fluctuates around zero, mean Z index assumes positive values that keep increasing as layers progress. This is due to the polarization of Z values (Figure 69), which overall assume higher values with the increase of the layer number.
If linked to the observation of Z evolution throughout the 15 layers, this phenomenon can be linked to the more intense heat retention of the central beads observed in the previous paragraph. It is important to remember that the computation of Z index for each layer has no relationship with other layers. Therefore, the evolution observed is not the trivial result of the overall heat retention of the print, visualized with the progression of average profiles of Figure 70, since indexes are not computed with respect to an overall average profile. This means that the evolution observed is the result of the skewness of Z index distribution towards positive values, which is caused by presence of inner beads with very high Z indexes. These high Z indexes are in turn caused by a more intense heat retention for those regions than for the rest of the layer. In other words, mean Z index captures unbalances in the Z index distribution of each layer, which are caused by presence of many ROIs with thermal behaviour hotter than average in later layers. It does not capture evolutions of the average profile.

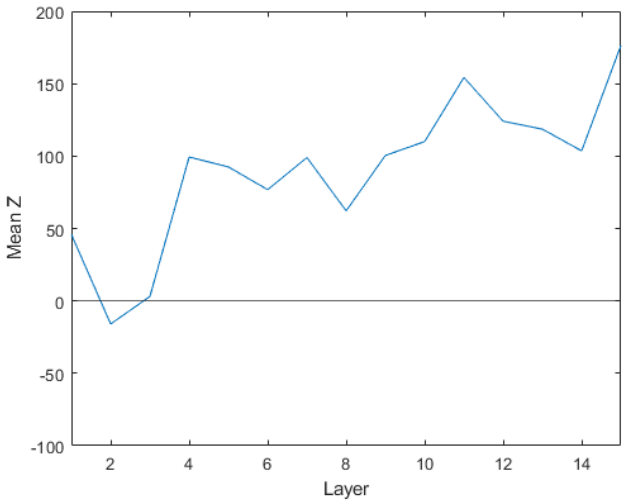

Figure 74: Mean Z index by Layer

Moving to the observation of Global Moran's I, the growth trend is very remarkable. This trend is impacted by the polarization of Z index values observed before (beads 2 and 4 with increasingly higher and bead 1 with increasingly lower Z index), since high absolute valued Z indexes lead to high Local Moran's I values, either positive or negative. It is not possible to assess whether the positive trend of Global Moran's I is exclusively caused by the polarization of Z indexes, or whether it is also influenced by increased spatial association of similar profiles. However, the metric is still relevant in confirming the non-stationarity of the process.

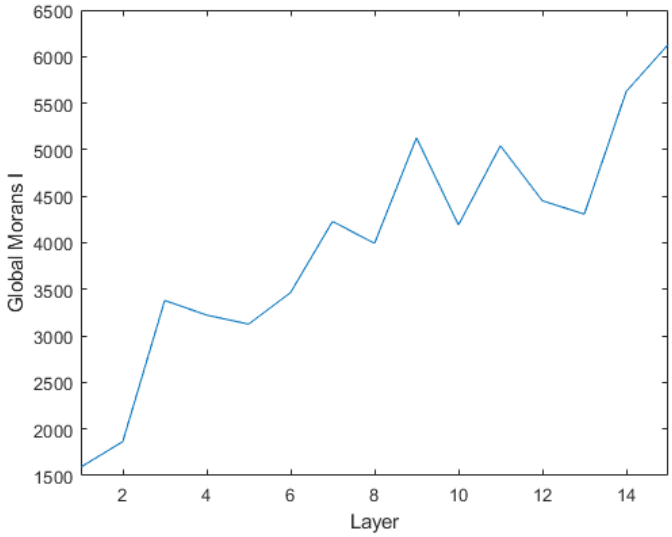

Figure 75: Global Moran's I by Layer

5.3.3 Discussion of results

In conclusion, despite the simplicity of the chosen toolpath, the process shows a lot of complexity in terms of thermal behaviour, both infra-layer and inter-layer. To sum up, different areas with homogeneous thermal behaviour are identified, i.e., different consecutive regions in the external beads and one more stable area between bead 2 and 4. All these areas are separated by sudden changes in temperature profiles, which resulted in jumps in Z values and negative values of local Moran's index. The presence of many homogeneous areas different to the average thermal profile resulted in a quite complex behaviour of Local Moran's I, which highlights many areas with high spatial association. Even within the more stable areas (from bead 2 to 4), an increasing spatial association towards the part centre is observed. For all these phenomena, we provided

some possible explanations related to the process dynamics (i.e., acceleration/deceleration of the extruder respectively at the beginning and the end of each layer) and to the process physics (i.e., heat retention). Finally, a local temperature perturbation has been observed in the middle of bead 3 for almost all layers. From a visual inspection of the thermal video, this inhomogeneity seems to be linked to the presence of a local temperature flaw, which might be related to different kind of defects. This last point will be further discussed in section 5.4, where these signals will be exploited for thermal in-situ monitoring.

Both global metrics (mean Z index and Global Moran's I) show non-stationarity of the process, presenting upward trend. For mean Z index, the trend can be linked to the increasing skewness of Z index distribution towards positive values (as result of more intense heat retention of inner beads). For Global Moran's I the interpretation is less clear, however the trend is most likely caused by the combined effect of increasing spatial association with creation of more clusters of similar behaviour and by the polarization of Z index.

When it comes to automatic defect identification, the methodology already proposed in the simulation study is inadequate for this case study. First of all, it does not embed the temporal evolution of the indicators within each layer. Moreover, the lack of knowledge of the in-control state of the process, combined with the growing trend of the monitoring metrics (mean Z index and Global Moran's I), do not allow the application of the classical control charts proposed in simulation. Given the impossibility to exploit the two global metrics to build control chart, and the subsequent lack of identification of OOC layers, the diagnostic step is not applied, since its purpose is the identification of anomalies within critical layers. In section 5.4, a variation of the monitoring approach is proposed, aimed at dealing with the case study complexity.

5.4 Monitoring of localized inhomogeneities

The qualitative assessment of the thermal behaviour via Z index and Local Moran's I performed in the previous sections showed presence of jumps in terms of Z index between adjacent cells. These signal's jumps reveal the presence of sudden temperature variation and, overall, thermal inhomogeneities, which may be origin of

local parts defects. In this context, process monitoring may be a useful approach to prevent the arising of final part defects by leveraging the in-situ thermal information.

Considering the common application for parts produced with this technology (usually production of moulds for automotive and aerospace applications), the spatial disposition of these anomalies is crucial to understand their impact on the final part. In general, we can infer that defect placed on the outer part surface (or in proximity of it) has a low impact on the final part integrity, since the outer surface is always reworked through machining for a better surface finishing. Thus, even if some defect arises in the outer beads, these will be partially or totally removed in post-processing phase. In case of internal anomalies, they would be difficult to detect and, eventually, to remove. For these reasons, we will focus the monitoring study on the internal beads, excluding the first and last bead, together with the lateral turning points, as shown in Figure 76.

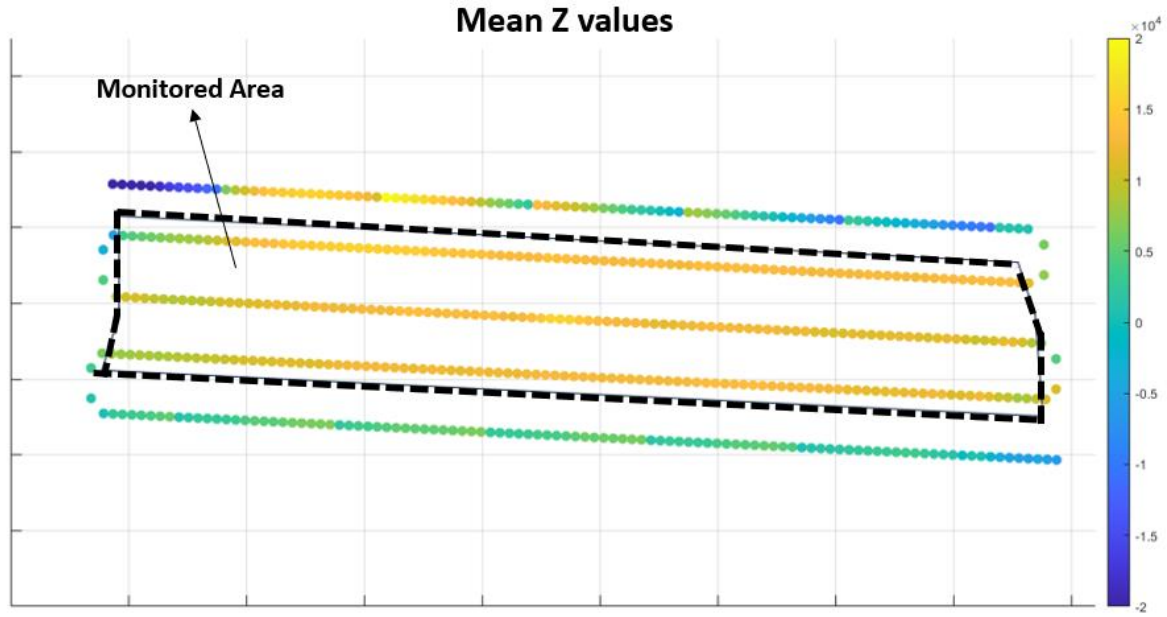

Figure 76: ROIs considered for monitoring of localized inhomogeneities

Next paragraphs will be devoted to the description and the results of the proposed monitoring approach. Paragraph 5.4.1 will describe the applied methodology, while paragraph 5.4.2 will discuss the results.

5.4.1 Monitoring methodology

The signal proposed for the monitoring approach is Z index, which was discussed in paragraph 5.3.1. As previously shown in Figure 69, its behaviour appears not stationary, with a change of the mean value among different beads, but also within each bead. Moreover, since Z values are computed on adjacent ROIs, they result to be autocorrelated. These observations are confirmed from the sample autocorrelation function (ACF) and partial autocorrelation function (PACF), shown in Figure 77.

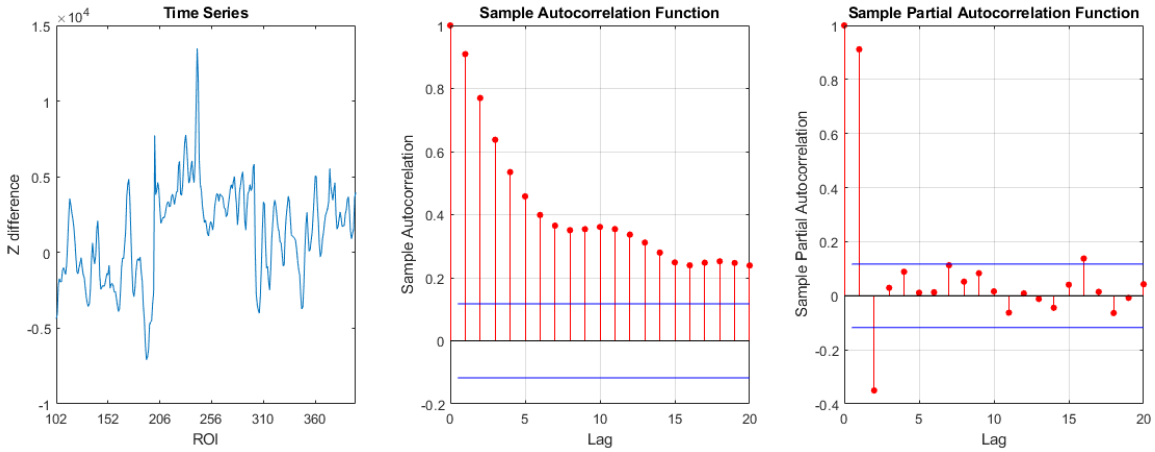

Figure 77: Statistical analysis of Z index for layer 1

After differentiation, ACF and PACF still highlight the presence of an autoregressive component and moving average component.

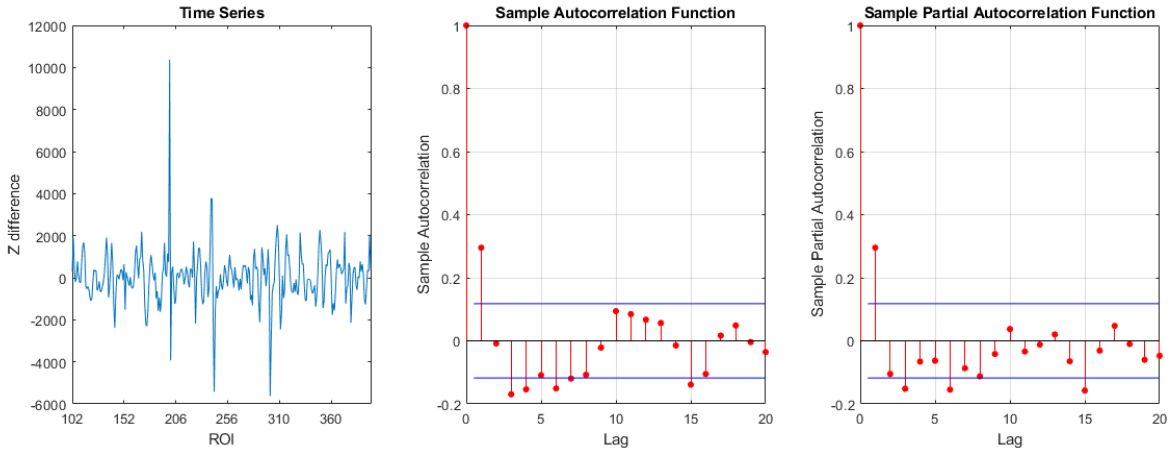

Figure 78: Statistical analysis of Z gradient for layer 1

In order to propose an effective in-situ monitoring solution, a control chart for autocorrelated data should be considered. Among the solutions for monitoring of positively autocorrelated data, the Exponentially Weighted Moving Average (EWMA) is well established as an effective and efficient solution which does not require expensive training. The rationale behind this approach lies in the use of the EWMA statistic as one-step-ahead forecast for the process output x_t, to then build a control chart to monitor the prediction error. In specific, the EWMA statistic is computed as:

$$z_t = \lambda \cdot x_t + (1 - \lambda) \cdot z_{t-1} \tag{18}$$

Where $0 < \lambda \leq 1$.

As a result, the prediction error at time *t* is computed as:

$$e_t = x_t - z_{t-1} \tag{19}$$

An EWMA control chart for autocorrelated data is thus proposed for monitoring. To compute the one-step-ahead prediction, λ is set equal to 0.2, as usually assumed in EWMA. Control limits are set adaptively as:

$$UCL_t = +3 \cdot \sqrt{\widehat{\sigma_t^2}} \tag{20}$$

$$LCL_t = -3 \cdot \sqrt{\widehat{\sigma_t^2}} \tag{21}$$

where $\widehat{\sigma_t^2}$ is the smoothed variance computed as:

$$\widehat{\sigma_t^2} = \alpha \cdot {e_t}^2 + (1 - \alpha) \cdot \widehat{\sigma_{t-1}^2} \tag{22}$$

Setting $\alpha = 0.01$, as suggested by MacGregor and Harris (1993) [54], and starting from the initial value of $\widehat{\sigma_0^2}$, equal to the variance of residuals measured in the first layer (Phase 1 of the control chart).

5.4.2 Discussion of Results on Monitoring

The EWMA control chart for layer 1 and a visualization of the location of the OOC found are shown in the following images:

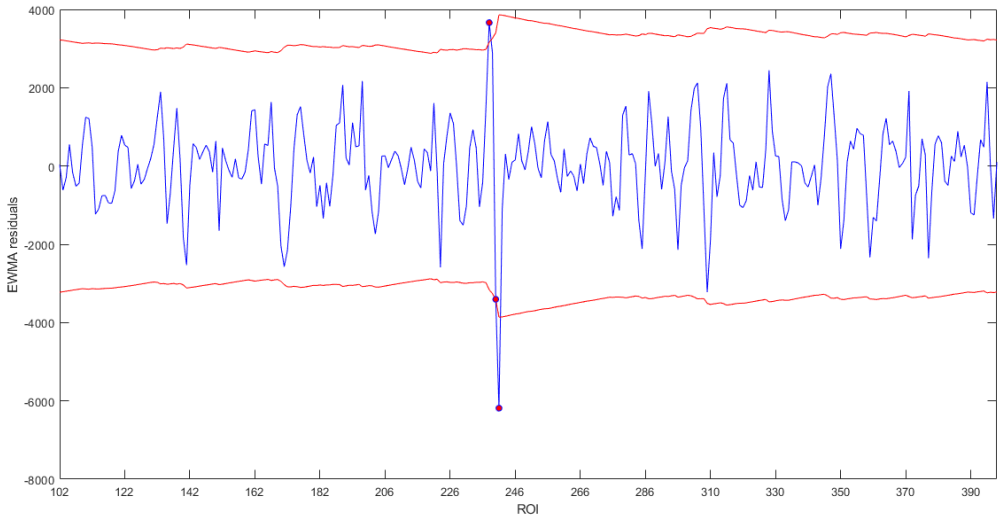

Figure 79: CC on EWMA residuals for layer 1

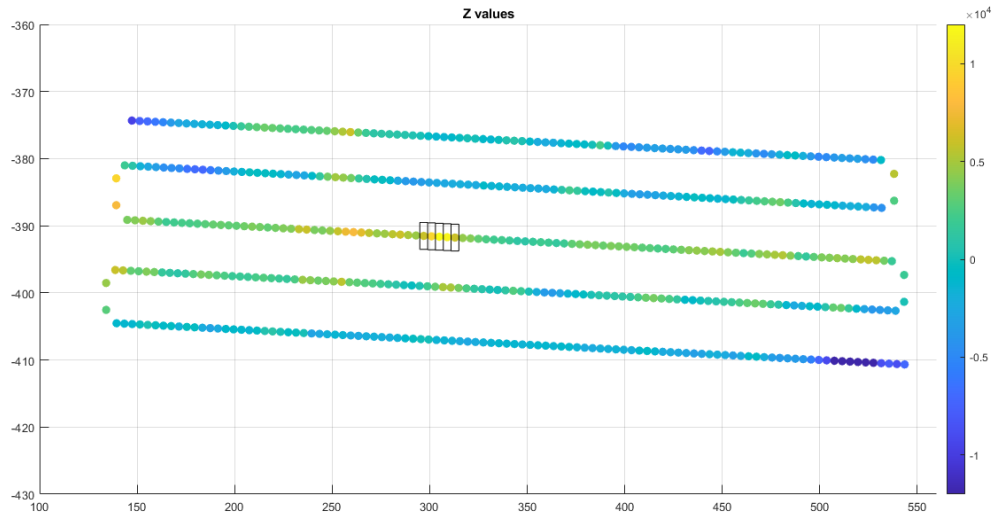

Figure 80: OOC of layer 1 highlighted on the scatterplot of Z index values for layer 1

The jumps highlighted are between ROIs belonging to the hot spot in the middle of bead 3. A highlight of the hot spot for layer 1 from the IR video is provided in the following image.

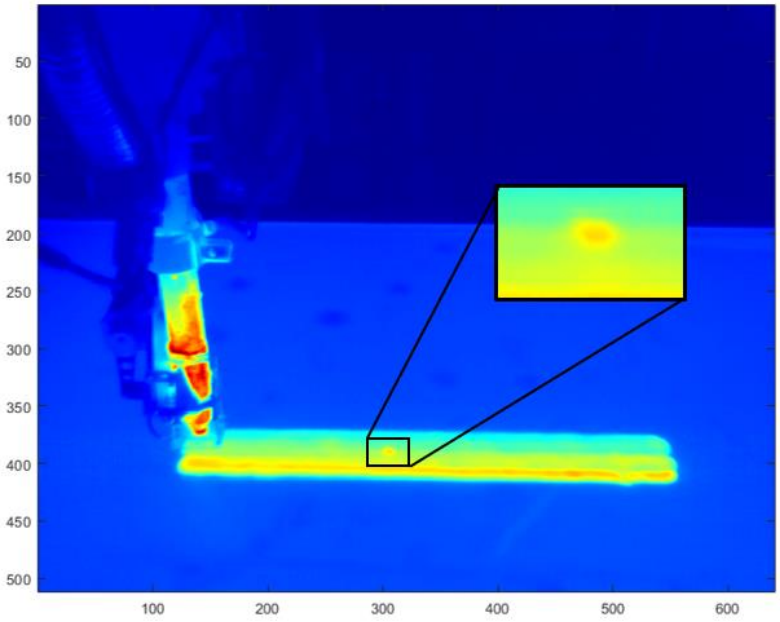

Figure 81: Highlight of middle hot spot for layer 1

Variables z_n and δ_n, the last ones, are kept as starting point for phase 2. By setting z_0 and δ_0 to the last values for layer 1, it is possible to repeat the same approach for following layers, focusing again only on central ROIs. The resulting CC is provided hereafter:

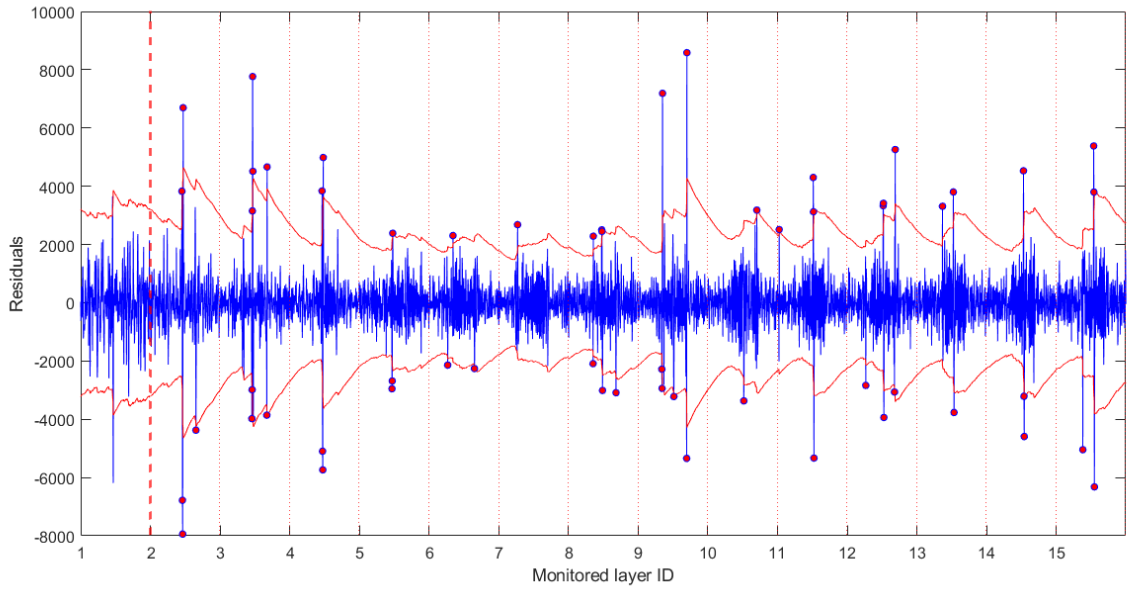

Figure 82: CC on EWMA residuals for all layers after the 1st one

Nearly all alarms of the chart are related to the same spatial location, i.e., either the central hot spot or irregularities located at the beginning and at the end of each bead, as shown in Figure 83. As mentioned before, the anomalous and high values of Z index in the centre of the bead reveals the presence of a localized hot spot. The presence of a hot area is visible for all layers (except 6 and 7) from IR images reported in Figure 84. Moreover, in layers 6 another hot spot is highlighted, this time located between bead 1 and 2, on the left side of the print. This defect is clearly visible from the IR frame associated to layer 6. Different out of controls are detected in correspondence of the beginning and the end of the analysed beads. The presence of these alarms at the beginning or end of bead is reasonable, since they may be linked to the acceleration and deceleration phases of the nozzle, which can cause instability in the material feed rate and result in under/over-extrusion [19]. As regards false alarms or OOC with a not clear explanation, only two cases are observed, particularly in layer 7 and 12, around three quarters of bead 2. Through a more thorough analysis, we can see how for layer 12 it is located in correspondence to a jump of the 1st bead, therefore we can assume that the inhomogeneity is caused by the interaction with an adjacent bead characterized by inhomogeneous thermal behaviour, while for layer 7 it may be the result of the interaction with the hot spot of layer 6.

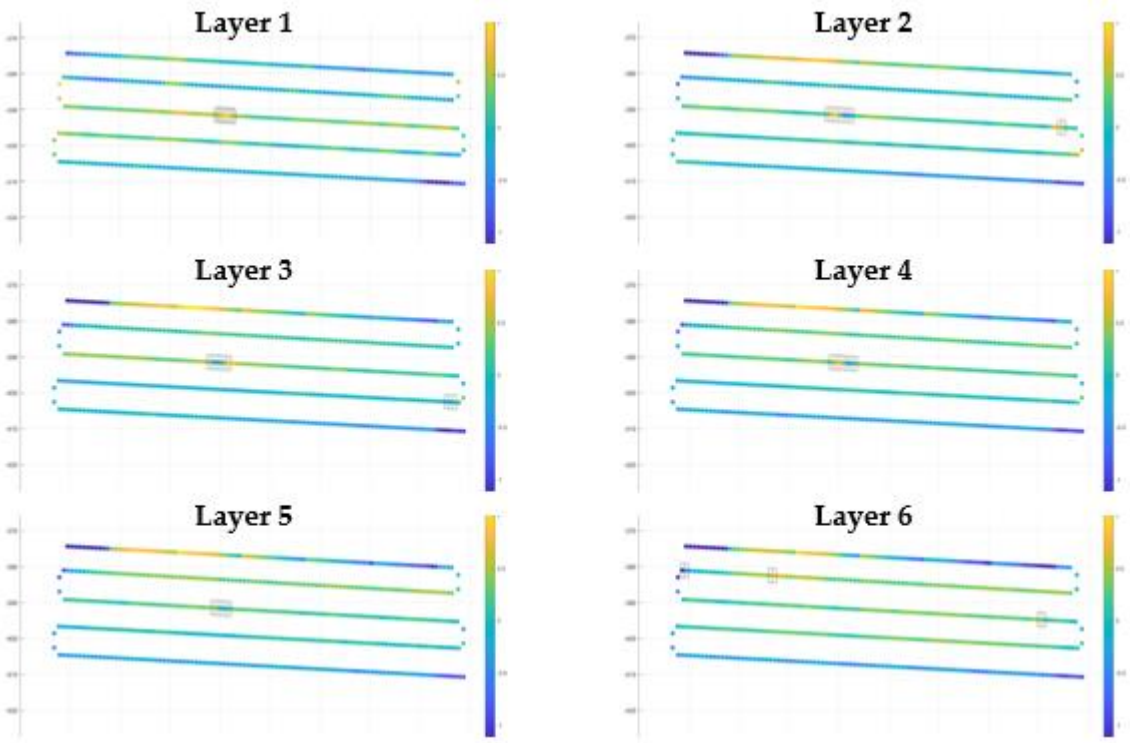

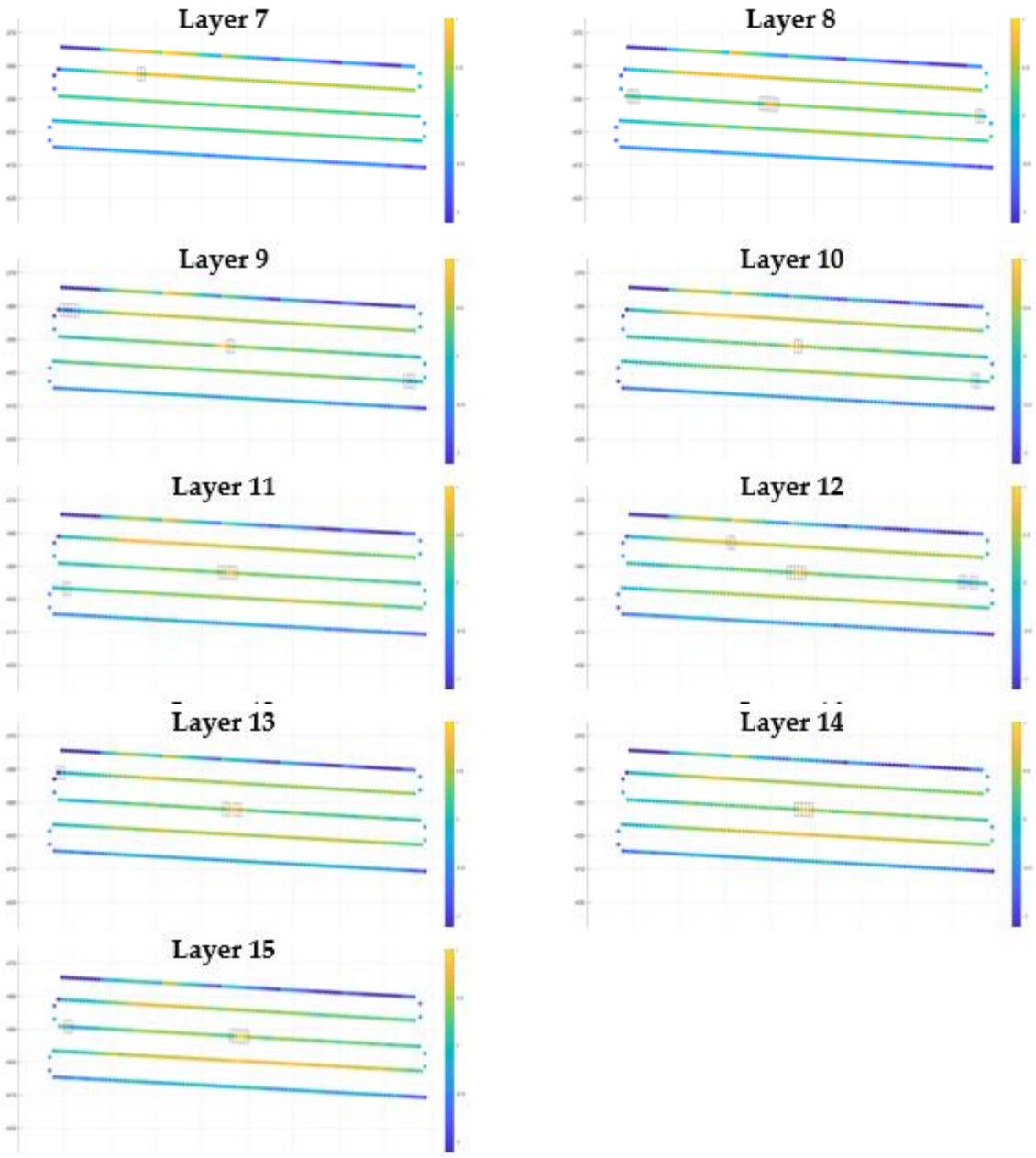

Figure 83: visualization of OOC location for all layers, highlighted as squares placed on the scatterplot of all ROIs with colormap proportional to Z index

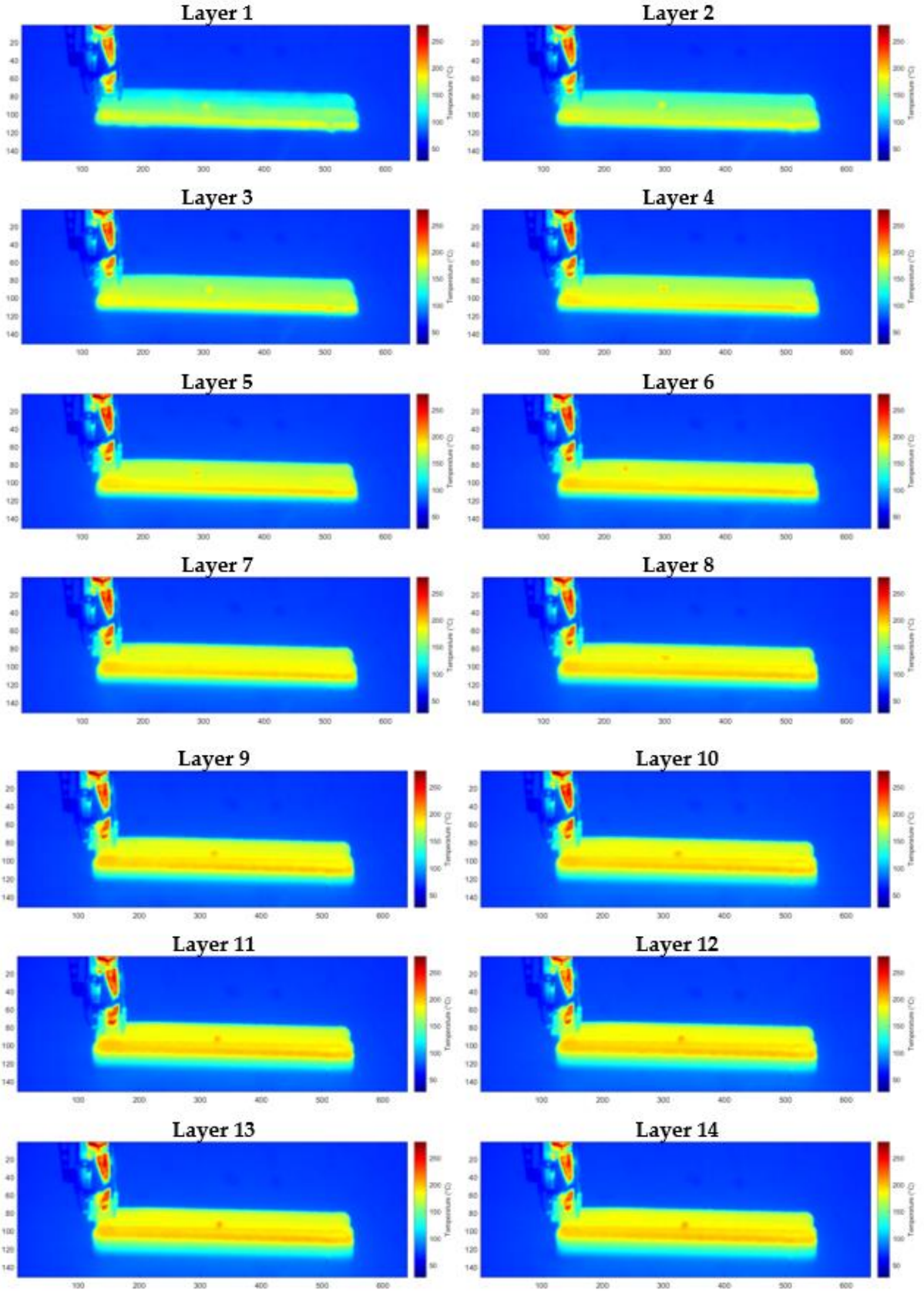
Layer 1
Layer 2
Layer 3
Layer 4
Layer 5
Layer 6
Layer 7
Layer 8
Layer 9
Layer 10
Layer 11
Layer 12
Layer 13
Layer 14

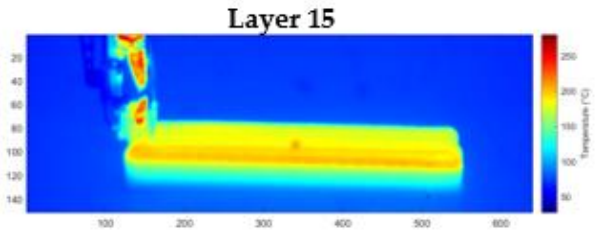

Figure 84: Visualization of a frame for each of the 15 layers

In conclusion, this methodology shows the ability of automatically detecting those local anomalies that were qualitatively observed in Z index analysis (paragraph 5.3.1). Moreover, it highlights the presence of temperature changes in proximity to the turning points, where the extruder changes its direction and speed. These results, together with the low number of alarms with unclear explanation, makes this methodology suitable for online monitoring applications.

6. Conclusion and future developments

In the past years, Additive Manufacturing technologies have drastically changed the manufacturing panorama, introducing a vast range of new possibilities in terms of product design and materials, paving the way to mass customization. The adoption of Extrusion-based AM processes grew quickly due the easy-to-use and low-cost machines, spreading in the industrial world for rapid prototyping use, as well as among hobbyist, fostering AM democratization. Extrusion AM processes recently gained an increasing attention for many promising innovations, such as the possibility of producing big volume parts, new printable materials (techno polymers, composites, metals etc.) and new applications (i.e., bioprinting). However, low repeatability and stability have limited the diffusion of extrusion-based AM in industrial world, being unable to achieve quality desired for finished products.

To tackle this issue, the scientific and the industrial community have recently proposed methods based on in-situ monitoring to prevent the arising of defects, in a first-time-right production perspective. Among many available information sources, the process' thermal behaviour has recently found significant interest, since it allows the identification of anomalies linked to quality issues, such as lack of bond (i.e., delamination, inter-road voids), failures due to heat retention, warpage, and over/under-extrusion states. So far, most of studies on thermal profiles analysis are based on data acquired via IR thermography. However, many papers are dedicated to in-situ sensing solutions for temperature measurement, without taking steps towards automatic defect identification. Moreover, none of the existing studies tackled together the temperature temporal evolution and the spatial dimension (i.e., the location within the layer where temperature profiles are extracted). This lack of techniques for spatiotemporal analysis is not only present for extrusion-based processes but, in our knowledge, it is absent in all the papers concerning in-situ monitoring for Additive Manufacturing.

In this thesis, a methodology for spatiotemporal thermal data analysis and monitoring of AM processes based on spatiotemporal analysis of temperature is proposed. The methodology is inspired by the paper from Gao et al. (2019) [8], in which the authors presented a new version of Local Moran's I, a local index for spatial association, that embeds a temporal descriptor (Z index). This index and a methodology for monitoring and diagnosis were tested both on simulation experiments and on a real case study.

As regards the simulation study, matrices of thermal profiles are simulated, using a temperature model based on previous study on thermal measurement and modelling for extrusion-based AM. Three defective scenarios are explored, i.e., *single clustered defect*, *sparse defects* and *two clustered defects*, testing both monitoring and diagnostic capabilities of the methodology. In all scenarios, different defect sizes and magnitude were analysed. Results showed that the use of Z index and Moran's I for defect detection and diagnosis enable the identification of thermal anomalies. Moreover, the monitoring approach resulted to be robust towards different defects typologies, size and magnitude. In this framework, this thesis also proposed a new algorithm for diagnosis based on hierarchical clustering. This approach outperformed the algorithm proposed by Gao et al. (2019), showing more stable results in presence of large defects.

As regards the real case study, the dataset used consists of an IR video of a serpentine printed part (ABS with 20% fibre) by means of a Big Area Additive Manufacturing (BAAM) system. Temperature profiles are extracted along the toolpath, and they are used to compute Z index and Local Moran's I. These indicators enabled the description and the analysis of thermal evolution along the extruder path, highlighting great complexity of thermal phenomena despite the simplicity of the chosen toolpath. More in detail, these indicators underline the instability of temperature evolution in proximity to the part's external edges, probably due to extruder motion changes. Furthermore, the presence of a local hot spot was identified in proximity to the central bead. Local Z indexes were further exploited to automatically detect the presence of this flaw through process monitoring. The proposed monitoring technique brought to the automatic identification and localization of the hot spots in every layer in which they are present, together with other anomalies linked to nozzle acceleration and deceleration phases.

Despite the promising results, the attention needs to be addressed towards some future developments. First, we propose to extend the simulation study towards other

temporal profiles alteration, to test the algorithm performances in more complex scenarios. Then, the combination between the current methodology and the a priori knowledge on the average (or target) thermal profile needs to be deepened, in order to increase the algorithm robustness towards the presence high number of anomalous profiles. As regards the real case applications, we suggest testing the proposed methodology to new real case studies related to other AM technology, such as Powder Bed Fusion, in order to demonstrate the algorithm's adaptability to different dataset.

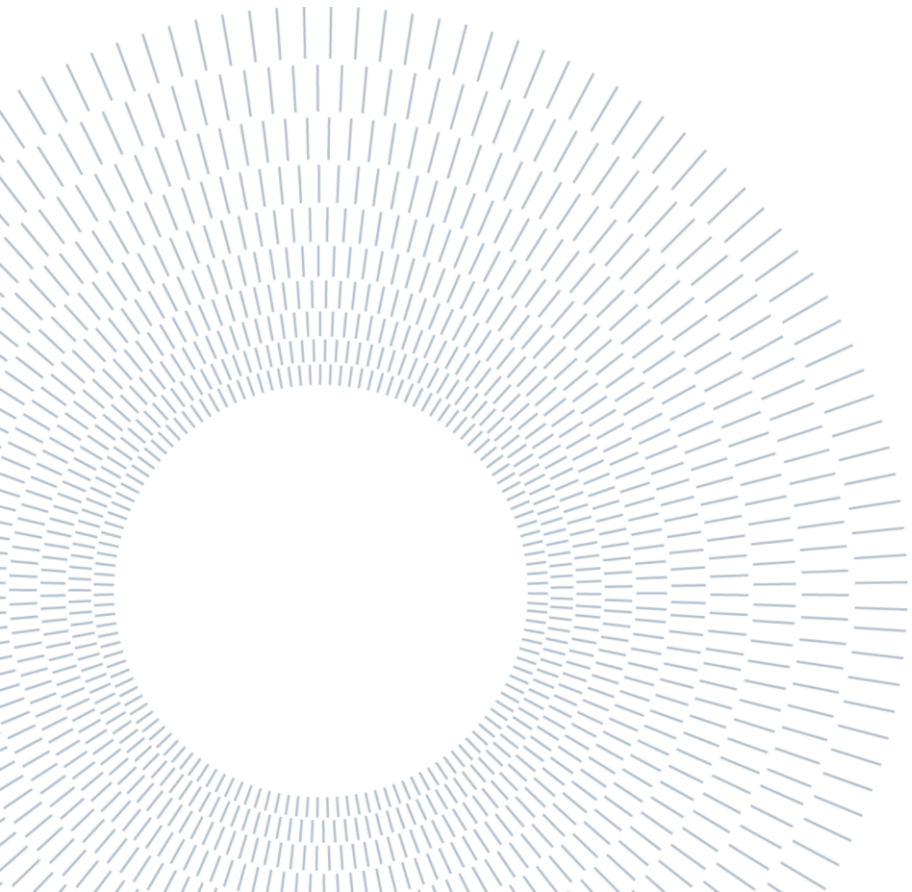

Bibliography

[1] ASTM, «ASTM F2792-10 standard terminology for additive manufacturing technologies».

[2] I. Gibson, D. Rosen e B. Stucker, «Additive Manufacturing Technologies 3D Printing, Rapid Prototyping, and Direct Digital Manufacturing Second Edition».

[3] «BIO X webpage,» [Online]. Available: https://www.cellink.com/product/cellink-bio-x/.

[4] «Oak Ridge National Laboratories website,» [Online]. Available: https://www.ornl.gov.

[5] «Masterprint webpage,» [Online]. Available: https://en.machinetools.camozzi.com/products/additive-manufacturing/all-products/masterprint-.kl.

[6] M. Grasso e B. M. Colosimo, «Process defects and in situ monitoring methods in metal powder bed fusion: A review,» *Measurement Science and Technology*, vol. 28, n. 4, 4 2017.

[7] Y. Fu, A. Downey, L. Yuan, A. Pratt e Y. Balogun, «In situ monitoring for fused filament fabrication process: A review,» *Additive Manufacturing*, vol. 38, 2 2021.

[8] Y. Gao, J. Cheng, H. Meng e Y. Liu, «Measuring spatio-temporal autocorrelation in time series data of collective human mobility,» *Geo-Spatial Information Science*, vol. 22, n. 3, pp. 166-173, 2019.

[9] A. D. Chouakria e P. N. Nagabhushan, «Adaptive dissimilarity index for measuring time series proximity,» *Advances in Data Analysis and Classification*, vol. 1, n. 1, pp. 5-21, 2007.

[10] B. N. Turner, R. Strong e S. A. Gold, «A review of melt extrusion additive manufacturing processes: I. Process design and modeling,» *Rapid Prototyping Journal,* vol. 20, n. 3, pp. 192-204, 2014.

[11] S. Wickramasinghe, T. Do e P. Tran, «FDM-Based 3D printing of polymer and associated composite: A review on mechanical properties, defects and treatments,» *Polymers,* vol. 12, n. 7, pp. 1-42, 7 2020.

[12] J. E. Seppala e K. D. Migler, «Infrared thermography of welding zones produced by polymer extrusion additive manufacturing,» *Additive Manufacturing,* vol. 12, pp. 71-76, 10 2016.

[13] «What are composites,» [Online]. Available: https://discovercomposites.com/what-are-composites/.

[14] V. Kishore, C. Ajinjeru, A. Nycz, B. Post, J. Lindahl, V. Kunc e C. Duty, «Infrared preheating to improve interlayer strength of big area additive manufacturing (BAAM) components,» *Additive Manufacturing,* vol. 14, pp. 7-12, 3 2017.

[15] C. E. Duty, V. Kunc, B. Compton, B. Post, D. Erdman, R. Smith, R. Lind, P. Lloyd e L. Love, «Structure and mechanical behavior of Big Area Additive Manufacturing (BAAM) materials,» 2017. [Online].

[16] W. Sun, B. Starly, A. C. Daly, J. A. Burdick, J. Groll, G. Skeldon, W. Shu, Y. Sakai, M. Shinohara, M. Nishikawa, J. Jang, D. W. Cho, M. Nie, S. Takeuchi, S. Ostrovidov, A. Khademhosseini, R. D. Kamm, V. Mironov, L. Moroni e I. T. Ozbolat, «The bioprinting roadmap,» *Biofabrication,* vol. 12, n. 2, 4 2020.

[17] U. Yaman, «Shrinkage compensation of holes via shrinkage of interior structure in FDM process,» *International Journal of Advanced Manufacturing Technology,* vol. 94, n. 5-8, pp. 2187-2197, 2 2018.

[18] C. Schmutzler, A. Zimmermann e M. F. Zaeh, «Compensating Warpage of 3D Printed Parts Using Free-form Deformation,» *Procedia CIRP,* vol. 41, pp. 1017-1022, 2016.

[19] B. N. Turner e S. A. Gold, «A review of melt extrusion additive manufacturing processes: II. Materials, dimensional accuracy, and surface roughness,» *Rapid Prototyping Journal,* vol. 21, n. 3, pp. 250-261, 4 2015.

[20] T. M. Wang, J. T. Xi e Y. Jin, «A model research for prototype warp deformation in the FDM process,» *International Journal of Advanced Manufacturing Technology,* vol. 33, n. 11-12, pp. 1087-1096, 8 2007.

[21] F. Awaja, S. Zhang, M. Tripathi, A. Nikiforov e N. Pugno, «Cracks, microcracks and fracture in polymer structures: Formation, detection, autonomic repair,» *Progress in Materials Science,* vol. 83, pp. 536-573, 10 2016.

[22] S. Garzon-Hernandez, D. Garcia-Gonzalez, A. Jérusalem e A. Arias, «Design of FDM 3D printed polymers: An experimental-modelling methodology for the prediction of mechanical properties,» *Materials and Design,* vol. 188, 3 2020.

[23] C. Bellehumeur, L. Li, Q. Sun e P. Gu, «Modeling of bond formation between polymer filaments in the fused deposition modeling process,» *Journal of Manufacturing Processes,* vol. 6, n. 2, pp. 170-178, 2004.

[24] Z. Jin, Z. Zhang e G. X. Gu, «Automated Real-Time Detection and Prediction of Interlayer Imperfections in Additive Manufacturing Processes Using Artificial Intelligence,» *Advanced Intelligent Systems,* vol. 2, n. 1, p. 1900130, 1 2020.

[25] R. Van Weeren, M. Agarwala, V. R. Jamalabad, A. Bandyophadyay, R. Vaidyanathan, N. Langrana+, A. Safari, P. Whalen#, S. Danforth e C. Ballard#, «Quality of Parts Processed by Fused Deposition,» 1995.

[26] A. P. Valerga, M. Batista, J. Salguero e F. Girot, «Influence of PLA filament conditions on characteristics of FDM parts,» *Materials,* vol. 11, n. 8, 7 2018.

[27] L. G. Blok, M. L. Longana, H. Yu e B. K. Woods, «An investigation into 3D printing of fibre reinforced thermoplastic composites,» *Additive Manufacturing,* vol. 22, pp. 176-186, 8 2018.

[28] C. Oztan, R. Karkkainen, M. Fittipaldi, G. Nygren, L. Roberson, M. Lane e E. Celik, «Microstructure and mechanical properties of three dimensional-printed continuous fiber composites,» 1 2019. [Online].

[29] D. S. Ertay, A. Yuen e Y. Altintas, «Synchronized material deposition rate control with path velocity on fused filament fabrication machines,» *Additive Manufacturing,* vol. 19, pp. 205-213, 1 2018.

[30] «simplify3D,» [Online]. Available: https://www.simplify3d.com/support/print-quality-troubleshooting/stringing-or-oozing/.

[31] A. Saluja, J. Xie e K. Fayazbakhsh, «A closed-loop in-process warping detection system for fused filament fabrication using convolutional neural networks,» 10 2020. [Online].

[32] H. Hu, K. He, T. Zhong e Y. Hong, «Fault diagnosis of FDM process based on support vector machine (SVM),» *Rapid Prototyping Journal,* vol. 26, n. 2, pp. 330-348, 2 2020.

[33] M. Moretti, A. Rossi e N. Senin, «In-process monitoring of part geometry in fused filament fabrication using computer vision and digital twins,» *Additive Manufacturing,* vol. 37, 1 2021.

[34] W. Lin, H. Shen, J. Fu e S. Wu, «Online quality monitoring in material extrusion additive manufacturing processes based on laser scanning technology,» *Precision Engineering,* vol. 60, pp. 76-84, 11 2019.

[35] K. He, Q. Zhang e Y. Hong, «Profile monitoring based quality control method for fused deposition modeling process,» *Journal of Intelligent Manufacturing,* vol. 30, n. 2, pp. 947-958, 2 2019.

[36] I. Cummings, E. Hillstrom, R. Newton, E. Flynn e A. Wachtor, «In-Process Ultrasonic Inspection of Additive Manufactured Parts,» 2016.

[37] M. Moretti, F. Bianchi e N. Senin, «Towards the development of a smart fused filament fabrication system using multi-sensor data fusion for in-process monitoring,» *Rapid Prototyping Journal,* vol. 26, n. 7, pp. 1249-1261, 7 2020.

[38] Z. Jin, Z. Zhang e G. X. Gu, «Autonomous in-situ correction of fused deposition modeling printers using computer vision and deep learning,» *Manufacturing Letters,* vol. 22, pp. 11-15, 10 2019.

[39] K. Okarma e J. Fastowicz, «Adaptation of full-reference image quality assessment methods for automatic visual evaluation of the surface quality of 3D prints,» *Elektronika ir Elektrotechnika,* vol. 25, n. 5, pp. 57-62, 10 2019.

[40] R. B. Dinwiddie, L. J. Love e J. C. Rowe, «Real-time process monitoring and temperature mapping of a 3D polymer printing process,» *Thermosense: Thermal Infrared Applications XXXV,* vol. 8705, p. 87050L, 5 2013.

[41] E. Malekipour, S. Attoye e H. El-Mounayri, «Investigation of Layer Based Thermal Behavior in Fused Deposition Modeling Process by Infrared Thermography,» vol. 26, pp. 1014-1022, 2018.

[42] E. Ferraris, J. Zhang e B. Van Hooreweder, «Thermography based in-process monitoring of Fused Filament Fabrication of polymeric parts,» *CIRP Annals,* vol. 68, n. 1, pp. 213-216, 1 2019.

[43] K. Choo, B. Friedrich, T. Daugherty, A. Schmidt, C. Patterson, M. A. Abraham, B. Conner, K. Rogers, P. Cortes e E. MacDonald, «Heat retention modeling of large area additive manufacturing,» *Additive Manufacturing,* vol. 28, pp. 325-332, 8 2019.

[44] K. He, H. Wang e H. Hu, «Approach to online defect monitoring in fused deposition modeling based on the variation of the temperature field,» *Complexity,* vol. 2018, 2018.

[45] P. A. P. Moran, «Notes on Continuous Stochastic Phenomena,» 1950.

[46] L. Anselin, «Local Indicators of Spatial Association-LISA,» 1995.

[47] J. Gong, J. Lee, S. Zhou e S. Li, «Toward measuring the level of spatiotemporal clustering of multi-categorical geographic events,» *ISPRS International Journal of Geo-Information,* vol. 9, n. 7, 7 2020.

[48] F. Caltanissetta, G. Dreyfus, A. J. Hart e B. M. Colosimo, «In-situ monitoring of Extrusion-based processes via thermal videoimaging with application to Big Area Additive Manufacturing (BAAM),» *Additive Manufacturing,* 2021.

[49] C. Vercellis, Business Intelligence, 2009.

[50] P. Janssen e C. Walther, «Sachsen-Anhalt View project Archetypes of (un)sustainability View project,» 2012.

[51] «Cincinnati Incorporated - BAAM webpage,» [Online]. Available: https://www.e-ci.com/baam.

[52] C. Harris e M. Stephens, «A COMBINED CORNER AND EDGE DETECTOR,» 1988.

[53] R. Killick, P. Fearnhead e I. A. Eckley, «Optimal detection of changepoints with a linear computational cost,» 2012. [Online].

[54] J. F. Macgregor e T. J. Harris, «The Exponentially Weighted Moving Variance,» *Journal of Quality Technology,* 1993.

[55] «findchangepts function documentation,» [Online]. Available: https://it.mathworks.com/help/signal/ref/findchangepts.html.

[56] M. Hebda, C. McIlroy, B. Whiteside, F. Caton-Rose e P. Coates, «A method for predicting geometric characteristics of polymer deposition during fused-filament-fabrication,» *Additive Manufacturing,* vol. 27, pp. 99-108, 5 2019.

[57] C. Barile, C. Casavola e A. Cazzato, «Acoustic emissions in 3D printed parts under mode I delamination test,» *Materials,* vol. 11, n. 9, 9 2018.

[58] A. D'Amico e A. M. Peterson, «An adaptable FEA simulation of material extrusion additive manufacturing heat transfer in 3D,» *Additive Manufacturing,* vol. 21, pp. 422-430, 5 2018.

[59] E. Rodriguez, J. Mireles, C. A. Terrazas, D. Espalin, M. A. Perez e R. B. Wicker, «Approximation of absolute surface temperature measurements of powder bed

fusion additive manufacturing technology using in situ infrared thermography,» *Additive Manufacturing,* vol. 5, pp. 31-39, 1 2015.

[60] U. Delli e S. Chang, «Automated Process Monitoring in 3D Printing Using Supervised Machine Learning,» vol. 26, pp. 865-870, 2018.

[61] S. F. Costa, F. M. Duarte e J. A. Covas, «Estimation of filament temperature and adhesion development in fused deposition techniques,» *Journal of Materials Processing Technology,* vol. 245, pp. 167-179, 7 2017.

[62] X. Zhou, S. J. Hsieh e Y. Sun, «Experimental and numerical investigation of the thermal behaviour of polylactic acid during the fused deposition process,» *Virtual and Physical Prototyping,* vol. 12, n. 3, pp. 221-233, 7 2017.

[63] Y.-H. Choi, C.-M. Kim, H.-S. Jeong e J.-H. Youn, «Influence of Bed Temperature on Heat Shrinkage Shape Error in FDM Additive Manufacturing of the ABS-Engineering Plastic,» *World Journal of Engineering and Technology,* vol. 04, n. 03, pp. 186-192, 2016.

[64] M. Moretti, A. Rossi e N. Senin, «In-process simulation of the extrusion to support optimisation and real-time monitoring in fused filament fabrication,» *Additive Manufacturing,* vol. 38, 2 2021.

[65] J. Li, R. Jin e H. Z. Yu, «Integration of physically-based and data-driven approaches for thermal field prediction in additive manufacturing,» *Materials and Design,* vol. 139, pp. 473-485, 2 2018.

[66] K. C. Ang, K. F. Leong, C. K. Chua e M. Chandrasekaran, «Investigation of the mechanical properties and porosity relationships in fused deposition modelling-fabricated porous structures,» *Rapid Prototyping Journal,* vol. 12, n. 2, pp. 100-105, 2006.

[67] M. Y. Ansari, A. Ahmad, S. S. Khan, G. Bhushan e Mainuddin, «Spatiotemporal clustering: a review,» *Artificial Intelligence Review,* vol. 53, n. 4, pp. 2381-2423, 4 2020.

[68] Y. Zhou, T. Nyberg, G. Xiong e D. Liu, «Temperature Analysis in the Fused Deposition Modeling Process,» *Proceedings - 2016 3rd International Conference on Information Science and Control Engineering, ICISCE 2016,* pp. 678-682, 10 2016.

[69] C. Kousiatza, N. Chatzidai e D. Karalekas, «Temperature mapping of 3D printed polymer plates: Experimental and numerical study,» *Sensors (Switzerland),* vol. 17, n. 3, 3 2017.

[70] X. Zhou e S.-J. Hsieh, «Thermal analysis of fused deposition modeling process using infrared thermography imaging and finite element modeling,» *Thermosense: Thermal Infrared Applications XXXIX,* vol. 10214, p. 1021409, 5 2017.

[71] D. C. Montgomery, Introduction to Statistical Quality Control - Eight Edition, 2019.

A. Appendix A

Setpoints Identification

In order to extract temperature profiles, a big challenge lies in synchronization, i.e., the automatic identification of starting point of a profile - which means finding for each ROI for each layer the frame enumeration at which temperature measurements begins - followed by the alignment of different temperature time series. The starting points are hereafter referred as setpoints. For each ROI and for each layer, setpoints are taken as the moment in which the print head extrudes material in the ROI under control. This allows to have a precise event to exploit to synchronize all temperature profiles.

In order to automatically detect when the print head is above a ROI, tracking information extracted in step 1 are used. Thus, for each ROI i and for each layer j, a distance function $d_{ij}(t)$ is built, extracting for each frame t the Euclidean distance between the centroid of ROI i and the tip of the print head. Setpoints are then identified among the frames belonging to a layer through the minimization of said function:

$$Setpoint_{ij} = \{\, t \in [t_{1,j}\,, t_{end,j}] \mid min_t\, d_{ij}(t)\} \tag{23}$$

Where:

$t_{1,j}$: frame at which the printing of layer j begins

$t_{end,j}$: frame at which the printing of layer j ends

Therefore, the temperature profile of a ROI for a layer is obtained by measuring the mean temperature inside of the ROI's cell for each frame between the setpoint of the current layer and the following setpoint, thus from material deposition on ROI i for the current layer until the initial deposition on ROI i for the following layer.

B. Appendix B

Change Points Identification

An explanation of the method used to identify change points in a signal is hereafter provided. The method is based on the paper from Killick et al. (2012) [53]. The methodology proposed is based on minimization of a cost function, which evaluates how good a subdivision of the signal is, given a predefined number of change points.

Given a signal $y_{1:n} = (y_1, \ldots, y_n)$ and a set of m change points $\tau_{1:m} = (\tau_1, \ldots, \tau_m)$, the overall cost of the subdivision the signal with the set of change points is:

$$\sum_{i=1}^{m+1} C(y_{\tau_{i-1}+1:\tau_i}) + \beta \tag{24}$$

Where:

β: penalty guard against overfitting

$C(y_{\tau_{i-1}+1:\tau_i})$: Cost function for the segment of signal between instants $\tau_{i-1} + 1$ and τ_i.

The changepoints are obtained minimizing the overall cost function. $C(y_{\tau_{i-1}+1:\tau_i})$ can be set in different ways. Killick et al. (2012) mention as common cost metrics negative log likelihood and quadratic loss. In our case, we use total residual error as cost function (from a mathematical point of view, minimization of residual error is equivalent to maximization of log likelihood), following the algorithm used in *MATLAB*'s function *findchangepts*, the implementation of Killick et al. (2012) methodology into the *Signal Processing Toolbox* [55]. In a nutshell, a statistical property is chosen as basis to find changes in the signal (e.g. mean, variance). Then, the residual error of a section is the sum of the deviation of the property with respect to its empirical

estimate for each point of the section. With this cost function, the identification of a changepoint for a signal consists of the following five steps:

1. Choose a point and divide the signal into two sections.
2. Compute an empirical estimate of the desired statistical property for each section.
3. At each point within a section, measure how much the property deviates from the empirical estimate. Add the deviations for all points.
4. Add the deviations section-to-section to find the total residual error.
5. Vary the location of the division point until the total residual error attains a minimum

Therefore, the changepoint k of a signal $y_{1:n} = (y_1, \ldots, y_n)$ is the element that minimizes the function:

$$J(k) = \sum_{i=1}^{k-1} \Delta(y_i, \chi(y_1, \ldots, y_{k-1})) + \sum_{i=k}^{n} \Delta(y_i, \chi(y_1, \ldots, y_{k-1})) \qquad (25)$$

Where Δ is the deviation measurement, χ is the statistical property chosen.

To find multiple changepoints, the approach is iterated selecting the sections found at a previous iteration as signals to split with a change point

List of Figures

List of Tables

Acknowledgements

A conclusione di questa tesi, desidero menzionare le persone che hanno contribuito, grazie al loro supporto, sia alla realizzazione di questo elaborato, che al completamento del mio percorso universitario.

Prima di tutto vorrei ringraziare la Professoressa Bianca Maria Colosimo, relatrice di questa tesi, non solo per l'immenso supporto datomi nella stesura della stessa, ma anche per avermi insegnato il valore della cura dei dettagli nello svolgere i propri compiti.
Grazie a Fabio Caltanissetta, co-relatore di questa tesi, non solo per la grande pazienza avuta nell'aiutarmi a trasformare le mie troppe idee in un lavoro solido e ben strutturato, ma anche per essere sempre stato in grado di trovare la giusta soluzione, o anche solo la giusta parola, per permettermi di continuare nei momenti di maggiore sconforto. Auguro a chiunque di poter lavorare almeno una volta nella vita con una persona dotata del tuo rigore e del tuo altruismo.
Grazie al Politecnico di Milano, e alla sua meravigliosa comunità, per avermi fatto sempre sentire a casa e avermi fatto crescere come ingegnere e come persona. Sono fiero ed onorato di aver condotto qui i miei studi

Grazie ai miei genitori, per i sacrifici fatti per permettermi di seguire i miei sogni, per tutto l'amore che mi date e per l'impegno che mettete ogni giorno per rendere la nostra famiglia il nido sicuro di cui sono tanto grato. Ogni momento con voi mi fa sentire la persona più fortunata del mondo.
Grazie a mia sorella Elena, la persona più importante per me a questo mondo. Non te lo dico spesso per non renderti arrogante, ma ti voglio un bene dell'anima.
Grazie alla nonna Dina, la mia unica nonna, perché se sono ciò che sono è anche grazie a lei. Non poter condividere questo traguardo con te per un soffio brucia moltissimo, so che saresti stata fiera. Mi mancherai.

Vorrei ringraziare i miei amici, siete tantissimi per nominarvi uno ad uno, il che mi rende immensamente orgoglioso di essermi circondato di persone a cui tengo così tanto e che mi facciano sentire tanto amato. Ci tengo a menzionare almeno i miei tre gruppi, ciascuno capace di farmi sentire parte di una famiglia.

Grazie ai TRA, il gruppo più longevo, adoro ogni nostro momento insieme, da quelli di gioia a quelli polemici, dalle stupende vacanze alle semplici serate a Salice. Mi aspetto per ognuno di voi una vita piena di successi, e spero che potremo condividerli sempre insieme.
Grazie agli SLEG, dagli amici di una vita a quelli più recenti, perché le nostre cene piene di vita, le notti magiche e le conversazioni profonde mi fanno sentire a pieno la gioia di aver vent'anni. Sapere di poter contare su ciascuno di voi è una delle mie più grandi fonti di conforto.
Grazie al Mango, il gruppo con cui ho condiviso a tempo pieno il mio periodo più felice e spensierato, sono avidamente affezionato ai nostri ricordi insieme, e sono grato di continuare a crearne con voi.
Una menzione speciale va a chi ha condiviso con me sia il duro percorso al Poli, che la vita nella mia amata Milano, quindi grazie a Teo, Lore, Luca, Checco, Ema, Simo e Marci.

Ringrazio anche i progetti che negli ultimi anni mi hanno dato degli obiettivi per cui lottare e delle squadre per cui giocare.
Grazie quindi ai ragazzi di Polimi Motorcycle Factory, con cui ho condiviso l'esperienza incredibile di Aragon e dei grandi successi, dover lasciare questo progetto mi lascia grande rammarico, ma anche grande conforto all'idea che il team darà ad altri l'opportunità di vivere quello che ho vissuto io.
Grazie ai ragazzi del Garpez, la manica di scappati di casa capaci più di chiunque altro di farmi ridere, salire sul palco con voi è la sensazione più elettrizzante a cui io possa pensare.

Infine, grazie ad Agi e alla Zia Bibi, perché siete i ricordi più belli della mia infanzia e nonostante il tempo passato, sento di dover anche a voi questo traguardo che sto per raggiungere.

Grazie a tutti,

Emanuele